Titre: Title:	Fabrication of Fiber Bragg Gratings Using Femtosecond Laser Direct-Writing Techniques
Auteur: Author:	Anthony Roberge
Date:	2022
Type:	Mémoire ou thèse / Dissertation or Thesis
Référence: Citation:	Roberge, A. (2022). Fabrication of Fiber Bragg Gratings Using Femtosecond Laser Direct-Writing Techniques [Master's thesis, Polytechnique Montréal]. PolyPublie. https://publications.polymtl.ca/10526/

POLYTECHNIQUE MONTRÉAL

affiliée à l'Université de Montréal

Fabrication of Fiber Bragg Gratings Using Femtosecond Laser Direct-Writing Techniques

ANTHONY ROBERGE

Département de génie physique

Mémoire présenté en vue de l'obtention du diplôme de *Maîtrise ès sciences appliquées*

Génie physique

Août 2022

POLYTECHNIQUE MONTRÉAL

affiliée à l'Université de Montréal

Ce mémoire intitulé :

Fabrication of Fiber Bragg Gratings Using Femtosecond Laser Direct-Writing Techniques

présenté par **Anthony ROBERGE**

en vue de l'obtention du diplôme de *Maîtrise ès sciences appliquées*

a été dûment accepté par le jury d'examen constitué de :

Yves-Alain PETER, président

Raman KASHYAP, membre et directeur de recherche

François LÉGARÉ, membre externe

ACKNOWLEDGEMENTS

First, I would like to express my deepest gratitude to Professor Raman Kashyap for giving me the opportunity to be part of his research group. Thank you for sharing your valuable knowledge and for believing in me, I'll remember the way you inspired me to keep learning.

I am also very grateful to all my colleagues in the Fabulas group for their support. Many thanks should go to Sébastien Loranger, Frédéric Monet, and Jean-Sébastien Boisvert, who taught me the arts of fiber Bragg grating fabrication and femtosecond laser processing. Your help made all the difference.

Additionally, I would like to thank Saket Kaushal and Professor José Azaña from INRS, with whom I had the pleasure of working on some ambitious projects.

Thanks should also go to my defense committee, Professors Yves-Alain Peter and François Légaré, for generously providing their knowledge and expertise.

Finally, thanks to my friends and family, and especially to my fantastic girlfriend Audrey-Anne for all her love and support. Your presence helped me a lot during this journey.

RÉSUMÉ

Les réseaux de Bragg (FBGs) sont des composantes essentielles dans plusieurs systèmes de fibre optique. Le sujet principal de cette thèse porte sur la fabrication des FBGs par écriture directe avec un laser femtoseconde. L'écriture directe est une technique employée pour modifier l'indice de réfraction de composés de verre dans une région contrôlée et localisée. Pour la fabrication de FBGs, cette technique peut être utilisée pour créer une variation périodique de l'indice de réfraction dans la fibre, une période à la fois.

Dans cette étude, un système d'écriture directe capable d'inscrire des structures de FBG avancées est développé. Différentes méthodes sont présentées pour atteindre la capacité à inscrire des structures arbitrairement complexes avec une grande qualité. À l'aide de la réflectométrie fréquentielle, une nouvelle méthode pour suivre la position du cœur de la fibre est démontrée. Durant le processus d'écriture, la position de chaque modification d'indice de réfraction est contrôlée grâce à une stratégie pour suivre et synchroniser la position des plateformes de translation. Cette stratégie de contrôle est utilisée pour implémenter une puissante technique d'apodisation s'appuyant sur la modulation de phase. Pour fabriquer des FBGs avec une réflectivité élevée et une perte d'insertion faible, une approche multi-pulse est investiguée.

Afin d'illustrer le potentiel du système d'écriture directe, plusieurs FBGs typiquement difficiles à fabriquer sont réalisés. En premier lieu, la capacité à inscrire un profil d'apodisation ou de phase arbitrairement complexe est démontrée par la fabrication d'un FBG nécessitant un contrôle précis de l'apodisation sur une large plage dynamique et avec une haute résolution spatiale. Par la suite, des capteurs de forme distribués sont produits dans des fibres avec un revêtement en polyimide et d'une longueur de l'ordre du mètre. Finalement, deux nouveaux filtres de phase servant au traitement de signal optique sont fabriqués et testés. Le premier de ces filtres est un FBG de 69 mm de longueur pour la compensation de la dispersion de la vitesse de groupe des signaux haute-vitesse traversant un lien de télécommunication de 70.56 km. Le design novateur de ces filtres permet de créer des dispositifs dont la longueur est 2.2 fois plus petite qu'un FBG conventionnel *chirpé* linéairement. Le second filtre est un FBG unique d'une longueur de 213 mm pouvant induire un déphasage de π sur une bande passante étroite de 1 GHz. Cette résolution fréquentielle

est 10 fois plus petit que celle d'un *waveshaper* optique commercial. Le filtre est utilisé pour démontrer un inverseur (porte logique NOT) passif à une vitesse de 45 Gbps.

ABSTRACT

Fiber Bragg gratings (FBGs) are key components in many fiber optics systems. The main topic of this thesis is on the fabrication of FBGs using femtosecond laser direct-writing. Direct-writing refers to the techniques employed to modify the refractive index of glass compounds over a controlled and localized area. For the fabrication of FBGs, these techniques can be used to create a periodic refractive index variation in a fiber, one period at the time.

In this work, a flexible direct-writing system capable of inscribing advanced FBG structures is developed. Different methods are presented to achieve the ability of inscribing any arbitrary complex structures with high quality. Using optical frequency domain reflectometry, a novel method to track the fiber core position is demonstrated. During the writing process, the position of each refractive index modification is controlled using a strategy based on position synchronized output tracking of the translation stages. This control strategy is used to implement a powerful apodization technique relying on phase modulation. To achieve FBGs with high reflectivity and low insertion loss, a multi-pulse approach is investigated.

To show the potential of the direct-writing system, several challenging gratings are realized. First, the ability to inscribe any types of arbitrary complex apodization or phase profiles is demonstrated by fabricating an FBG that requires control of apodization over a high dynamic range, and with a spatial resolution of at most 10 μm. Then, fully distributed optical fiber shape sensors are produced in meter-long polyimide coated fibers. Finally, two novel phase-only filters for signal processing are fabricated and tested. The first is a 69 mm long FBG for group velocity dispersion compensation of high-speed data signals passing through a 70.56 km telecommunication link. The novel design of this filter enables devices with a length 2.2x smaller than a conventional linearly chirped FBG. The second filter is a unique 213 mm ultra-long FBG that can impart an exact π phase shift over a narrow bandwidth of just 1 GHz. This frequency resolution is 10x better than that of a commercial optical waveshaper. The filter is used to demonstrate a fully-passive inverter (logic NOT gate) at a speed of 45 Gbps.

TABLE OF CONTENTS

LIST OF TABLES

LIST OF FIGURES

LIST OF SYMBOLS AND ABBREVIATIONS

CMT	Coupled-mode theory
CW	Continuous wave
DFB	Distributed feedback
DUT	Device under test
FBG	Fiber Bragg grating
FOSS	Fiber optic shape sensor
FS	Femtosecond
GVD	Group velocity dispersion
IL	Insertion loss
IR	Infrared
LCGA	Linearly chirped Gaussian apodized
NA	Numerical aperture
NRZ	Non-return-to-zero
OBR	Optical backscatter reflectometer
OFDR	Optical frequency domain reflectometry
OOK	On-off keying
PD	Polarization dependency
PSD	Power spectrum density
PSO	Position synchronized output
RBS	Random bit sequence
RI	Refractive index
RIM	Refractive index modification

RIU	Refractive index unit
RZ	Return-to-zero
TMM	Transfer matrix method
UV	Ultraviolet
WBG	Waveguide Bragg grating

LIST OF APPENDICES

CHAPTER 1 INTRODUCTION

1.1 Context and motivation

Fiber optics play an important role in our daily life, often unknowingly. Able to collect, transport, and manipulate light at high speed and over long distances, optical fibers are a significant component in a wide variety of technologies such as telecommunication networks, optical sensing, lasers, medical instruments, and more. In 1978, Hill *et al.* [1] showed that by exposing the core of an optical fiber to visible light radiation, permanent photo-induced refractive index change could be produced, and the discovery of this photosensitivity has led to the development of an essential device of today's fiber optic systems: Fiber Bragg gratings (FBGs). These devices consist of a periodic modulation in the refractive index (RI) of the fiber core, which fulfil the function of an inline wavelength-dependent dielectric mirror or filter [2].

Since then, a whole new research field about the theory and fabrication of FBGs has emerged, opening the door to countless applications possibilities. In the late 80s, a major breakthrough was made by Metlz *et al.* [3], who demonstrated a reliable method to produce FBGs by laterally exposing the core of a fiber to a coherent ultraviolet (UV) two-beam interference pattern produced by a phase mask. During the next decade, this technique became the state-of-art for FBG fabrication due to its high fidelity, and UV inscribed gratings were in great demand during the development of the telecommunication industry in the 90s [2].

However, in 1996, a new fabrication method started to gain some attention when Hirao *et al.* [4] showed that tightly focussed femtosecond (FS) laser pulses could be used to directly modify the RI inside the bulk of transparent materials. Because FS pulses are absorbed via nonlinear interactions with the material, this method has revealed some unique microfabrication capabilities compared to techniques based on linear absorption of UV radiation [5]. For instance, multiphoton absorption of FS pulses allows to induce strong refractive index modifications (RIMs) in almost any kind of glass compounds, with reduced constraints for photosensitivity. Also, since the RIM is confined in the focal spot of the laser, FS methods can be used to form three-dimensional structures with complex geometries.

Shortly after this discovery, in the early 2000s, FS laser processing systems started being exploited to inscribe FBGs using either phase mask methods [6, 7] or direct-writing methods [8].

Over the years, these different fabrication methods evolved into two distinct fields of research. While the phase mask technique has shown to produce FBGs with similar characteristics to those made by conventional UV inscription, it became popular for its stability and abilities for mass production. On the other hand, direct-writing methods have provided the ability to control the exact position of each RIM, giving them much more flexibility to produce devices with unique architecture. Since many FS lasers operate in the infrared (IR) wavelength range, FS inscription has also made it possible to inscribe FBGs directly through the polymer coating that protects optical fibers, as most acrylate are transparent to IR [9, 10].

At Polytechnique Montreal, Pr. Kashyap's group has been involved in the development of cutting-edge UV interferometric FBG inscription techniques for many years [2, 11-13]. However, a FS direct-writing system has long been desired to leverage on its unique attributes and to diversify the range of technology available for the fabrication of FBGs. As such, a direct-writing method could be used to quickly prototype different types of grating design with much more flexibility and reconfigurability than with a phase mask method. Hence, the purpose of this thesis is to describe the development and implementation of a FS laser direct-writing system that can be used to fabricate advanced FBG structures in many types of fiber.

1.2 Femtosecond direct-writing of fiber Bragg grating.

Ideally, the fabrication of FBGs with FS lasers should be simple, flexible, and modular, with the ability to fabricate any user defined structure, in many types of fiber. The system should be able to produce high-quality FBGs presenting strong index modification, low insertion loss (IL), low polarization dependence (PD), low coupling to cladding mode and yield repeatable results. It should also minimize the number of experimental requirements such as the preparation of fiber, calibration of the system, alignment, etc. Over the years, many techniques have been refined and optimized towards one or many of these attributes, but so far, a fabrication method combining all the aforementioned qualities has been hard to achieve and many challenges still remain for direct-writing techniques. For instance, the fabrication of any arbitrary complex FBG structure requires the ability to control the amplitude and phase profile of the grating with extreme precision [14], something that is still difficult today. This is even more difficult for ultra-long gratings [11], as

this precision needs to be maintained over a long distance, and any perturbation or error during the writing process can cause the FBG to deviate from its target spectral response.

In this context, this thesis is focussed on studying the different fabrication methods that were already proposed, in order to implement a direct-writing system featuring as much of the qualities mentioned above as possible. It is also in the scope of this work to propose new solutions to some of the known problems in the field of direct-writing of FBGs. Of course, the aim of research project is important because improvement of direct-writing techniques could lead to the realization of FBGs with advanced spectral functionalities, something that has great potential for further development of sophisticated optical sensors and filters.

1.3 Research objectives

This research project is structured around the following objectives:

1) Understand the current limitations of direct-writing techniques.
2) Propose new solutions to improve the capabilities of direct-writing systems.
3) Develop and implement a complete femtosecond direct-writing system capable of inscribing advanced FBGs in many types of fiber.
4) Demonstrate the capabilities of the writing system by inscribing different types of sensors and filters.

1.4 Thesis outline

This manuscript-based thesis is organized in 7 chapters. In Chapter 2, a complete literature review about the theory and fabrication methods of FBG is given, with the focus on FS laser processing. Chapter 3 introduces the manuscript that is presented in the thesis. More specifically, it gives information about the methodology used during this work and the findings that led to publication of an article. It also reveals the capabilities of the writing system by showing some examples of typical FBGs. Chapter 4 contains the manuscript [15] that was accepted for publication in Optics Express, which describes the different techniques developed to achieve high-quality inscription of first-order FBGs with arbitrary complex apodization. It includes 4 propositions to improve direct-writing methods: a novel alignment method for high accuracy

tracking of the fiber core position, a phase control strategy allowing to control the exact position of each RIM, an apodization method based on phase modulation, and the use of a multi-pulse regime to induce strong RIMs with low insertion loss. Chapter 5 presents two applications made possible by the writing system that was implemented. The first application is for 3D optical shape sensors, while the second concerns the realization of advanced filters for high-speed signal processing. Finally, Chapter 6 discusses about the results presented in this thesis. It also highlights some of the limitations and gives recommendations for further improvements. Chapter 7 concludes about this research.

CHAPTER 2 LITERATURE REVIEW

This chapter present the theory and literature review on the state-of-the-art fabrication techniques for fiber Bragg gratings (FBG). First, a theoretical description of an FBG is presented, along with current simulation models. Then, the physical mechanisms of refractive index (RI) modification by laser material processing are described. This includes the exposure of a photosensitive fiber to ultraviolet (UV) laser radiation or the use of a focussed femtosecond laser (FS) pulses to modify the RI in transparent material. Finally, a review of the different fabrication techniques used to produce FBG is given. More specifically, a detailed description of FS direct-writing techniques is given, as it is the main topic of this thesis.

2.1 Fiber Bragg gratings

This section reviews the fundamentals of FBG necessary to understand the content of this thesis. The typical spectral characteristics of uniform grating are derived from the coupled-mode theory, and the simulation tools required to calculate the spectral response of more complex structures are reviewed.

2.1.1 Basic model of fiber Bragg gratings

FBGs are produced by inducing a periodic modulation of the effective RI in the guiding region of an optical fiber [16-18]. A representation of the structure is shown in Figure 2.1. Mathematically, the effective RI change ($\Delta n_{eff}(z)$) of an FBG can be modelled as sinusoidal modulation:

$$\Delta n_{eff}(z) = n_{eff}(z) - n_0 = \overline{\Delta n_{eff}}(z)\left(1 + v(z)\cos\left(\frac{2\pi z}{\Lambda_g} + \phi(z)\right)\right) \qquad (2.1)$$

where $n_{eff}(z)$ is the effective RI along the longitudinal axis z of the fiber, n_0 is the effective RI of the unperturbed fiber, Λ_g is the grating period, $\overline{\Delta n_{eff}}(z)$ is the average RI change over a period, $v(z)$ is the grating visibility and $\phi(z)$ is the additional phase of the grating, generally used to introduce a chirp or phase shift. Note the coordinate system presented in Figure 2.1, it will be used throughout the rest of this thesis: z will be the longitudinal axis of the fiber, and the x and y axis will be its transverse plane.

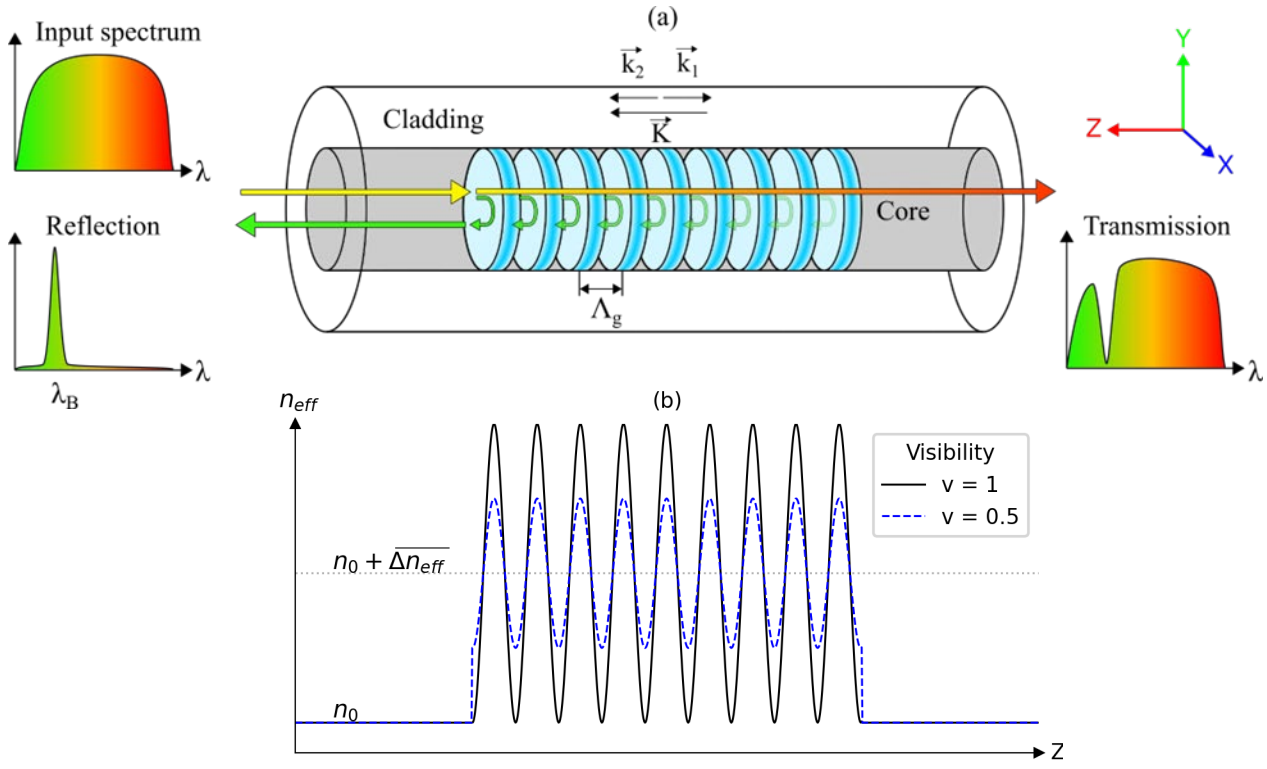

Figure 2.1: (a) Illustration of a uniform fiber Bragg grating structure. (b) Representation of the sinusoidal effective refractive index change for a visibility of 0.5 and 1.

Technically, the refractive index modification (RIM) induced by the laser is not necessarily sinusoidal and could be described by some other periodic functions. However, Eq. (2.1) can be seen as the first Fourier component of such functions and, in most situation, is a suitable approximation to describe the index modulation of an FBG and the effect it has on guided light.

In the case of a reflection grating, the light guided through the fiber experiences multiple Fresnel reflections at each of the grating planes and coupling between modes travelling in opposite directions can occurs. When in phase, the light reflected from each interface interferes constructively over a narrow wavelength range, which is reflected very efficiently by the grating, at what is called the Bragg wavelength (λ_B). On the contrary, out of phase light undergoes destructive interference and only weak reflection is observed. The Bragg condition is derived from the laws of momentum and energy conservation, applied to a diffraction grating [18]. The conservation of momentum implies that the wavevector of the incident light wave ($\vec{k}_1$), plus the grating wavevector ($\vec{K} = m2\pi/\Lambda_g$), should be equal to the diffracted wavevector ($\vec{k}_2$). With the

wavevector amplitude being equal to the propagation constant such that $|\vec{k}| = \beta = 2\pi n_{eff}/\lambda$, we get:

$$\vec{k}_2 = \vec{k}_1 + \vec{K} \quad \rightarrow \quad -\beta_2 = \beta_1 - m\frac{2\pi}{\Lambda_g}, \tag{2.2}$$

where m is the grating order. In the case of a short-period reflection grating, as illustrated in Figure 2.1, β_2 and m have a negative value since the reflected light propagates in the opposite direction relative to the incident light wave. By rearranging Eq. (2.2), the Bragg wavelength is expressed as:

$$\lambda_B = \left(n_{eff,1} + n_{eff,2}\right)\Lambda_g/m. \tag{2.3}$$

Usually, the fabrication of an FBG in a standard single-mode fiber implies that $n_{eff,1} = n_{eff,2}$. However, the notation of Eq. (2.3) highlights the possibility of coupling to cladding modes, to the higher-order modes of a multimode fiber, or to a mode with an orthogonal polarization in the case of a birefringent fiber. It should also be noted that FBG can be sorted into two categories: reflection and transmission gratings. Transmission gratings were not studied during this thesis, so let's consider them only briefly. If β_2 and m had a positive value, Eq. (2.3) could be rewritten as:

$$\lambda_B = \left(n_{eff,1} - n_{eff,2}\right)\Lambda_g/m. \tag{2.4}$$

Coupling to forward propagating modes at a particular wavelength is therefore possible, but the required Λ_g is much longer, which is why transmission gratings are also called long-period grating.

2.1.2 Coupled-mode theory

The optical properties of an FBG, such as the reflection and transmission spectral response, are fundamentally determined by $\Delta n_{eff}(z)$. They are usually modelled using the coupled-mode theory (CMT) [16, 17], which is one of the most widely used tool to study FBGs. Let's consider the most important results using the formulation given by Erdogan [16].

The transverse component of the electric field (E_t) of a guiding medium can be defined as a superposition of all the possible j guided modes:

$$E_t(x,y,z,t) = \sum_j \left(A_j(z)e^{i\beta_j z} + B_j(z)e^{-i\beta_j z}\right)\vec{e}_{jt}(x,y)e^{-i\omega t}, \tag{2.5}$$

where $A_j(z)$ and $B_j(z)$ are the field amplitudes of the forward and backward travelling j^{th} mode, $\vec{e}_{jt}(x,y)$ is the normalized transverse mode field, and β_j is the propagation constants of the mode.

The energy exchange between the modes of amplitude $A_j(z)$ and $B_k(z)$ can be described by the coupled-mode equations [16]. It is generally assumed that coupling predominantly occurs between identical counter-propagating modes, and, by only considering this type of interaction, the coupled-mode equations can be written as:

$$\frac{dR}{dz} = i\hat{\sigma}R(z) + i\kappa S(z), \tag{2.6}$$

$$\frac{dS}{dz} = -i\hat{\sigma}S(z) - i\kappa^* R(z), \tag{2.7}$$

where $R(z)$ and $S(z)$ are respectively the forward (reference) and the coupled backward (signal) fields defined as:

$$R(z) = A_j(z)e^{(i\delta z - \phi(z)/2)}, \tag{2.8}$$

$$S(z) = B_j(z)e^{(-i\delta z + \phi(z)/2)}. \tag{2.9}$$

The parameter δ is the detuning from the phase matching condition:

$$\delta = \beta - \frac{\pi}{\Lambda_g} = \frac{2\pi n_{eff}}{\lambda} - \frac{\pi}{\Lambda_g}. \tag{2.10}$$

At the wavelength for which $\delta = 0$, the phase matching condition is said to be satisfied and maximum coupling occurs. This requires $\lambda = 2n_{eff}\Lambda_g$, which is the same result that was found in Eq. (2.3), as the phase matching condition can also be thought of as momentum conservation.

The coefficient $\hat{\sigma}$ is the general "dc" coupling coefficient, and is defined as:

$$\hat{\sigma} = \delta + \sigma - \frac{1}{2}\frac{d\phi}{dz}. \tag{2.11}$$

It encompasses the different process that can affect the local phase matching condition of the grating, such as the average RI change $\overline{\Delta n_{eff}}(z)$ (related to σ) and the local phase variation. Finally, σ and κ are the so-called "dc" and "ac" coupling coefficient. κ, one of the most important parameters, determines how strong is the coupling between the modes. Both σ and κ are defined by an overlap integral between the guided mode fields and the cross-sectional shape of the RIM ($\overline{\Delta n_{eff}}(x, y, \mathrm{z})$) given by:

$$\sigma(z) = \frac{\omega}{2}\iint_{-\infty}^{\infty} n_{eff}(x, y, \mathrm{z})\, \overline{\Delta n_{eff}}(x, y, \mathrm{z})\, \vec{e}_{kt}(x, y)\, \vec{e}_{jt}^{*}(x, y)\, dx\, dy, \tag{2.12}$$

$$\kappa(z) = \frac{v(z)\sigma(z)}{2}. \tag{2.13}$$

In the case of a single-mode fiber, and if the RIM is constant and homogeneous across the fiber core, the coupling coefficients can be simplify to [16]:

$$\sigma = \frac{2\pi}{\lambda}\overline{\Delta n_{eff}}M, \tag{2.14}$$

$$\kappa = \frac{\pi}{\lambda}v\overline{\Delta n_{eff}}M, \tag{2.15}$$

where M is the overlap integral of the fundamental mode inside the core, which can be seen as the fraction of that mode power contained inside the core.

2.1.2.1 Uniform Bragg grating

A uniform FBG is the simple case where all the grating parameters ($\overline{\Delta n_{eff}}$, v, ϕ) are kept constant along the z axis. The RI modulation can be reduced to:

$$\Delta n_{eff}(z) = \overline{\Delta n_{eff}}\left(1 + v\cos\left(\frac{2\pi z}{\Lambda_g}\right)\right). \tag{2.16}$$

For a uniform FBG of length L, Eq. (2.6) and (2.7) of the CMT described above can be solved analytically. The amplitude reflection coefficient $\rho = S(0)/R(0)$ and the power reflection coefficient $r = |\rho|^2$ can be expressed as:

$$\rho = \frac{-\kappa \sinh\left(\sqrt{\kappa^2 - \hat{\sigma}^2}L\right)}{\hat{\sigma}\sinh\left(\sqrt{\kappa^2 - \hat{\sigma}^2}L\right) + i\sqrt{\kappa^2 - \hat{\sigma}^2}\cosh\left(\sqrt{\kappa^2 - \hat{\sigma}^2}L\right)}, \tag{2.17}$$

$$r = \frac{\sinh^2\left(\sqrt{\kappa^2 - \hat{\sigma}^2}L\right)}{\cosh^2\left(\sqrt{\kappa^2 - \hat{\sigma}^2}L\right) - \frac{\hat{\sigma}^2}{\kappa^2}}. \tag{2.18}$$

From Eq. (2.17) and (2.18), two important properties can be derived: The peak reflectivity (r_{max}) and the bandwidth ($\Delta\lambda$) of the grating. They are given by:

$$r_{max} = \tanh^2(\kappa L), \tag{2.19}$$

$$\Delta\lambda = \frac{\lambda_B^2}{2\pi n_{eff} L}\sqrt{(\kappa L)^2 + \pi^2}. \tag{2.20}$$

Note that the product of κL is often referred to as the strength of the FBG, and this terminology will be used for the rest of this thesis.

Using Eq. (2.18), Figure 2.2 shows an example of the reflection and transmission spectra for two different uniform FBGs: one with a strength of $\kappa L = 2$ (black curve) and the other with $\kappa L = 6$ (blue curve). A length of 5 mm is considered for both. As it can be seen, the weaker FBG has a narrower bandwidth. Since $\Delta\lambda$ also depends on the length, keep in mind that for the same κL product, a longer FBG would exhibit a narrower bandwidth and vice-versa. The presence of side-lobes outside the main stop band can be explained by the sudden square shape of the RI profile at the extremity of the grating (see Figure 2.1 (b)), for which the Fourier transform contains multiple high order harmonics. These side-lobes are undesirables for many applications that require high attenuation at out-of-band wavelengths, but they can be substantially attenuated by smoothing the RI profile through a process called apodization [19].

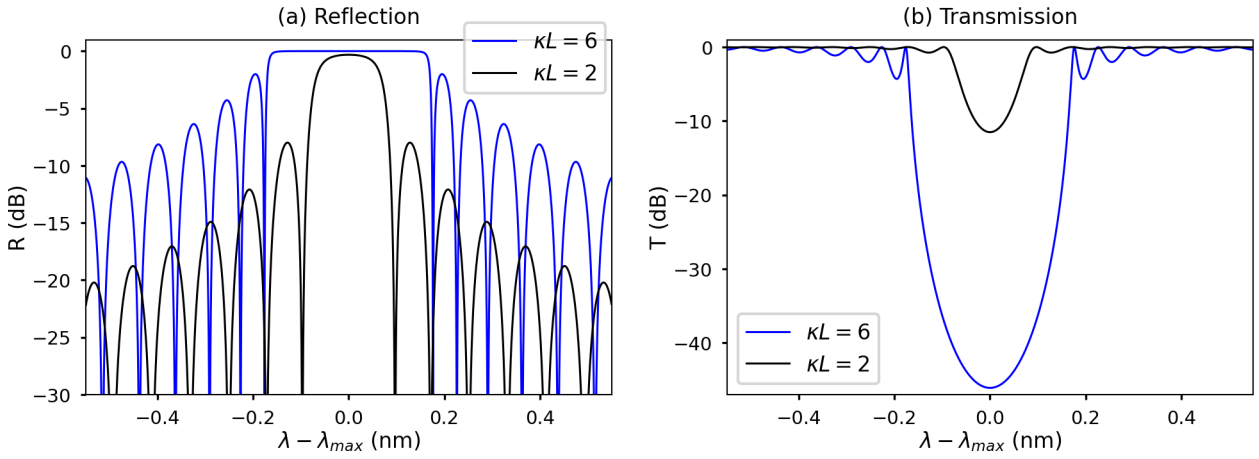

Figure 2.2: Example of the reflection and transmission spectrum for two uniform FBGs. In both cases, the length is set to 10 mm, but the grating strength (κL) is set to 2 (black) or 6 (blue).

2.1.2.2 Non-uniform Bragg grating

Despite their numerous applications, the spectral response of uniform FBGs is limited to a single stop band with important side-lobes at neighbouring wavelengths. Non-uniform FBGs offers the possibility to freely tailor the optical properties of the grating by adjusting some of its parameters along the length, such as the average RI change $\overline{\Delta n_{eff}}(z)$, the visibility $v(z)$ or the phase $\phi(z)$ [16, 18]. As an example, different non-uniform structures and their reflection spectra are shown in Figure 2.3. The process of apodization [19] is typically achieved by varying either of $\overline{\Delta n_{eff}}(z)$ or $v(z)$ to smooth out the envelope profile of the grating. It can be noted from Eq. (2.12) and (2.13) that a spatial variation of $\overline{\Delta n_{eff}}(z)$ affects both σ and κ, which causes an asymmetrical spectral response on the short-wavelength side, as illustrated in Figure 2.3 (a). Preferably, the apodization of $v(z)$ allows to maintain a constant $\overline{\Delta n_{eff}}$ along the grating, making the spectral response symmetric on both side of λ_B, with stronger side-lobes suppression, as depicted in Figure 2.3 (b). Moreover, $\phi(z)$ can also be varied to create a chirp in the grating structure and customized its dispersive characteristics. For example, Figure 2.3 (c) shows a linearly chirped FBG, and Figure 2.3 (d) shows a structure with a π phase shift in the middle.

Put together, apodization and chirping of FBGs gives the flexibility required to design optical devices with arbitrary complex spectral response, something that is very important for many practical applications.

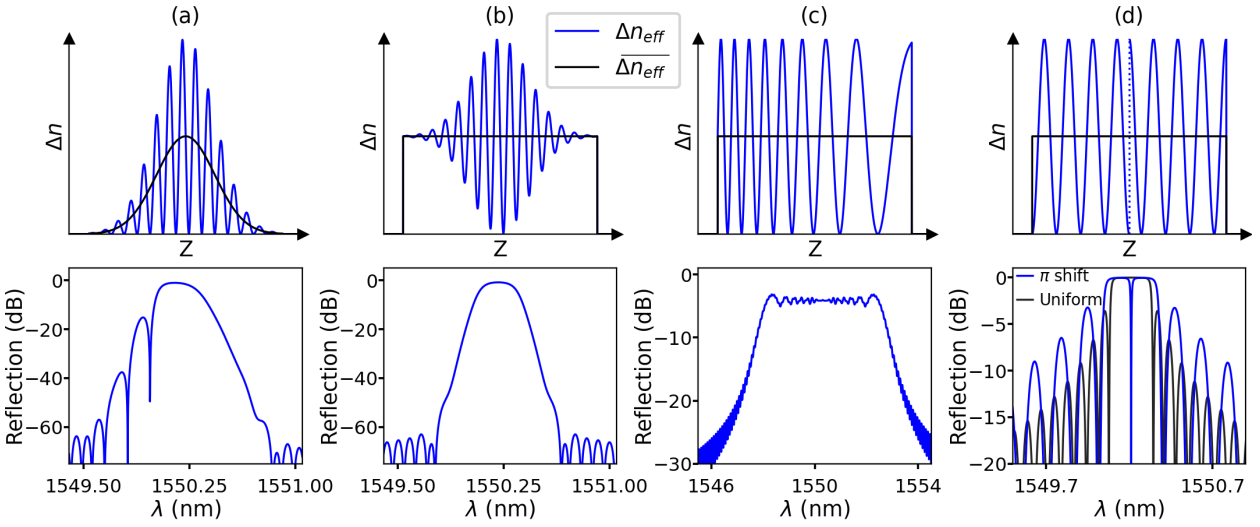

Figure 2.3: Different type of FBG RI profiles and their associated reflection spectra. The spectral simulations are done using the CMT TMM method, and assuming a length of 10 mm and $\overline{\Delta n_{eff}} = 2 \cdot 10^{-4}$. (a) Gaussian apodization of $\overline{\Delta n_{eff}}$. The non-uniform RI change induces a non-linear chirp in the grating structure, effectively shifting the Bragg wavelength at the extremities of the FBG. In this example, the extremities would reflect shorter wavelengths, causing the FBG to act as a Fabry-Perot cavity and resulting in an asymmetrical spectral response on the short wavelength side. (b) Gaussian apodization of $v(z)$. Maintaining a constant $\overline{\Delta n_{eff}}$ allows for a symmetric spectral response. (c) Linearly chirped FBG, with a chirp rate of 0.5 nm/mm. Since the FBG is not apodized, many oscillations are still present in the stop band. For this example, $\overline{\Delta n_{eff}} = 3 \cdot 10^{-4}$ (d) FBG with a π phase shift. The spectral response is compared to a uniform FBG of identical parameters.

2.1.3 Simulation techniques

To tailor complex spectral response, it is often required to engineer the FBG parameters ($\overline{\Delta n_{eff}}(z)$, $v(z)$, $\phi(z)$, …) with complex, sometimes discontinuous functions. Since the coupled-mode equations do not have a simple analytical solution for non-uniform gratings, simulation tools are required to calculate their spectral response. Many simulation techniques can be employed, but most of them falls under two categories. The first one contains techniques that directly solves the coupled-mode equations using numerical methods, either by direct integration,

or by a transfer matrix method (TMM) [16, 17]. The second includes methods that treat the grating as a multilayer structure which can be divided into many homogeneous layers [17].

2.1.3.1 Transfer matrix method for CMT

Even if it is possible to solve Eq. (2.6) and (2.7) by direct integration, this method is not the fastest and the preferred approach is to use the TMM [16, 17]. This method uses a piecewise approach, where the grating is divided into M uniform pieces, as represent in Figure 2.4. The propagation of light through each of the i^{th} grating sub-section is described by a 2x2 transfer function matrix ($\boldsymbol{F_i}$), which are then multiplied together to represent the whole grating:

$$\begin{bmatrix} R_i \\ S_i \end{bmatrix} = \boldsymbol{F_i} \begin{bmatrix} R_{i+1} \\ S_{i+1} \end{bmatrix}, \tag{2.21}$$

$$\boldsymbol{F_i} = \begin{bmatrix} \cosh(\gamma_B \Delta z) - i\dfrac{\hat{\sigma}}{\gamma_B}\sinh(\gamma_B \Delta z) & -i\dfrac{\kappa}{\gamma_B}\sinh(\gamma_B \Delta z) \\ i\dfrac{\kappa}{\gamma_B}\sinh(\gamma_B \Delta z) & \cosh(\gamma_B \Delta z) + i\dfrac{\hat{\sigma}}{\gamma_B}\sinh(\gamma_B \Delta z) \end{bmatrix}, \tag{2.22}$$

where R_i and S_i are the forward and backward field amplitude of the i^{th} grating sub-section and $\gamma_B = \sqrt{\kappa^2 - \hat{\sigma}^2}$.

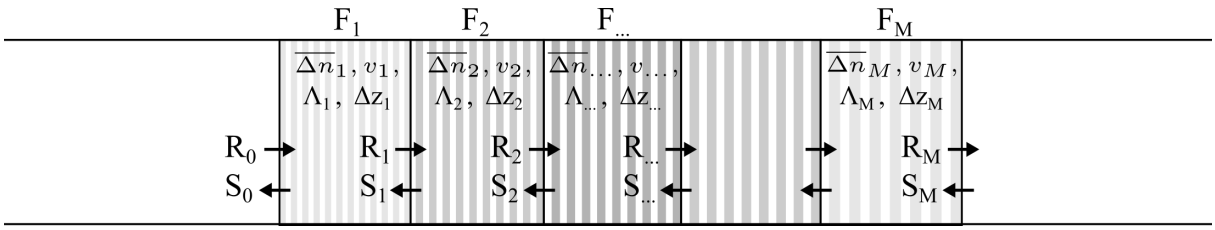

Figure 2.4: Representation of the grating structure with the CMT TMM.

To model the presence of a phase shift ($\Delta\phi_i$) in the grating structure, it is also possible to add a phase-shift matrix ($\boldsymbol{F_{\phi_i}}$) between the proper i^{th} and $(i+1)^{th}$ sections, given by:

$$\boldsymbol{F_{\phi_i}} = \begin{bmatrix} e^{-i\Delta\phi_i/2} & 0 \\ 0 & e^{i\Delta\phi_i/2} \end{bmatrix}; \quad \frac{\Delta\phi_i}{2} = \frac{2\pi n_{eff}}{\lambda}\Delta z_i. \tag{2.23}$$

By multiplying all the individual matrix together, the output field amplitude of the grating can be expressed as:

$$\begin{bmatrix} R_0 \\ S_0 \end{bmatrix} = \boldsymbol{F} \begin{bmatrix} R_M \\ S_M \end{bmatrix}; \qquad \boldsymbol{F} = \begin{bmatrix} \boldsymbol{F_{11}} & \boldsymbol{F_{12}} \\ \boldsymbol{F_{21}} & \boldsymbol{F_{22}} \end{bmatrix} = \boldsymbol{F_1} \cdot \ldots \cdot \boldsymbol{F_i} \cdot \ldots \cdot \boldsymbol{F_{M-1}} \cdot \boldsymbol{F_M}. \tag{2.24}$$

Assuming that the backward travelling field at the output ($z = L$) is $S_M = S(L) = 0$, the power reflection (r) and transmission (t) coefficients of the whole structure can be calculated by:

$$r = |\rho|^2 = \left|\frac{S_0}{R_0}\right|^2 = \left|\frac{F_{21}}{F_{11}}\right|^2, \tag{2.25}$$

$$t = |\tau|^2 = \left|\frac{R_M}{R_0}\right|^2 = \left|\frac{1}{F_{11}}\right|^2. \tag{2.26}$$

2.1.3.2 Multilayer analysis

The simulation methods under this category are based on segmenting the grating as a stack of multiple thin dielectric layers. Instead of using the coupled-mode equations to compute the transmission through each section, multilayer analysis represents each layer with two matrices. The reflection and transmission matrix ($\boldsymbol{T_i}$) models the effect of each interface using complex Fresnel coefficients, and the phase shift matrix ($\boldsymbol{P_i}$) is associated to the propagation in the medium. Different formulation of the method can be found in [17, 20-23].

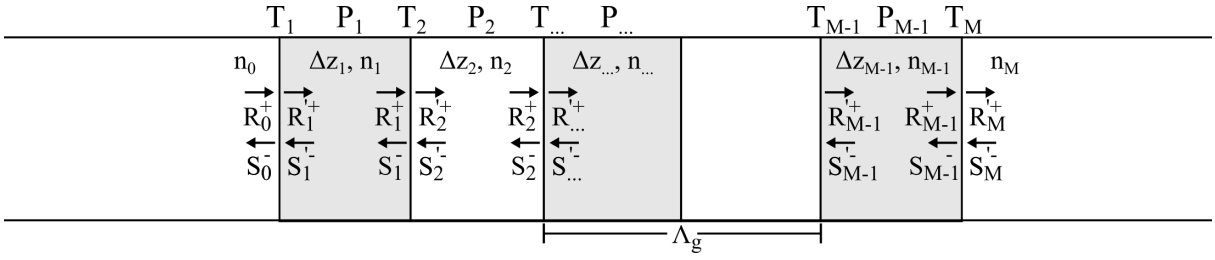

Figure 2.5: Illustration of the grating structure as a stack of thin dielectric layers.

Figure 2.5 shows an illustration of this method, where the forwards and backward propagating fields at each interface are related to each other with the following transmission ($\boldsymbol{T_i}$) and phase shift ($\boldsymbol{P_i}$) matrices:

$$\begin{bmatrix} R_{i-1}^{+} \\ S_{i-1}^{-} \end{bmatrix} = \boldsymbol{T_i} \begin{bmatrix} R_i'^{+} \\ S_i'^{-} \end{bmatrix}; \qquad \boldsymbol{T_i} = \frac{1}{\tau_i} \begin{bmatrix} 1 & \rho_i \\ \rho_i & 1 \end{bmatrix}, \tag{2.27}$$

$$\begin{bmatrix} R_i'^{+} \\ S_i'^{-} \end{bmatrix} = \boldsymbol{P_i} \begin{bmatrix} R_i^{+} \\ S_i^{-} \end{bmatrix}; \quad \boldsymbol{P_i} = \begin{bmatrix} e^{i\Delta\phi_i} & 0 \\ 0 & e^{-i\Delta\phi_i} \end{bmatrix}. \tag{2.28}$$

The phase shift $\Delta\phi_i$ associated to a layer of thickness Δz_i and the reflection (ρ_i) and transmission (τ_i) coefficients of each layer are given by:

$$\rho_i = \frac{n_i - n_{i-1}}{n_i + n_{i-1}}; \quad \tau_i = \frac{2n_i}{n_i + n_{i-1}}; \quad \Delta\phi_i = \frac{2\pi n_i}{\lambda}\Delta z_i. \tag{2.29}$$

Combining Eq. (2.27) and (2.28), the whole grating structure can be represented by:

$$\begin{bmatrix} R_0 \\ S_0 \end{bmatrix} = \boldsymbol{F} \begin{bmatrix} R_M \\ S_M \end{bmatrix}; \quad \boldsymbol{F} = (\boldsymbol{T_1} \cdot \boldsymbol{P_1}) \cdot \ldots \cdot (\boldsymbol{T_i} \cdot \boldsymbol{P_i}) \cdot \ldots \cdot (\boldsymbol{T_{M-1}} \cdot \boldsymbol{P_{M-1}}) \cdot \boldsymbol{T_M}. \tag{2.30}$$

Again, the reflection (r) and transmission (t) coefficient can be calculated using Eq. (2.25) and (2.26). Compared to the CMT TMM, where each sub-sections may have a length of multiple grating periods, the multilayer analysis must be computed for every variation of the RI, which can be time consuming. However, multilayer analysis can be advantageous when the spacing between each grating planes is not constant and varies rapidly [21], as the CMT TMM is limited when the sub-sections are too small, or when the apodization or phase profile of the grating are not slowly varying function [16, 17]. This will be the case later in the thesis.

Finally, Rouard's method could also be included in this category of multilayer analysis. Instead of a single transfer matrix for each interface of different RI, this method subdivides each of the grating period into further subsections. It can be used to accurately simulate different types of RI modulation which are not sinusoidal or square. Different formulations can be found in [24-26].

2.2 Mechanism of refractive index modification

Before describing the many techniques that can be used to fabricate FBG, this section reviews the different mechanisms involve in laser-induced refractive index modification of glass material.

2.2.1 Linear absorption of laser radiation

When the energy of a photon is higher than the band gap of a dielectric material, it can be absorbed linearly by the material and cause a permanent modification to its structure. This

phenomenon, called photosensitivity [27], can be used to change the RI of glass materials, which have a band gap that lies in the UV wavelength range (around 9 eV for pure fused silica [28]).

In the case of optical fibers, their photosensitivity to UV light has been exploited to inscribe FBGs by exposing the core of the fiber to the radiation of a UV laser [11, 29]. A detailed description of the photosensitivity of optical fibers is given in [27]. Standard telecommunication fiber, such as the SMF-28, are made with a pure fused silica cladding and a germanium doped core. Pure silica itself is transparent to UV light (down to 190 nm), but the presence of germanium-oxide defects in the core have been found to induce photosensitivity to wavelength between 190 - 270 nm [11, 27]. Naturally, the photosensitivity of germanosilicate fiber is highly correlated to the concentration of GeO defect in its matrix. In the case of a typical SMF-28 fiber, the low concentration of Ge in its core makes it only weakly photosensitive to UV radiation. To increase this photosensitivity, photosensitization methods, such as hydrogen loading, are typically employed [27].

2.2.2 Modification of refractive index by femtosecond laser

The RI of glass materials can also be modified with FS laser pulses, which is the main topic of this thesis. Several books and publications have been written on this rich subject, but an excellent starting point can be found in the book by Osellame *et al.* [5] or in [30, 31].

Instead of being absorbed linearly by the bandgap of the GeO defects present in the germanosilicate glass lattice [32], FS pulses can modify the RI of transparent materials through non-linear optical processes [5, 30, 31]. When tightly focussed, FS pulses can easily achieve high peak intensities in the order of 10 TW/cm^2 and above, which is enough to initiate non-linear photoionization of the electrons by multiphoton absorption [33]. The electrons that are promoted to the conduction band can also absorb the laser light linearly until they have enough energy to ionize another electron that is bound to its nucleus, resulting in a process of avalanche ionization and the generation of a free-electron plasma. Of course, the dynamics of this plasma depend on the pulse parameters, and the ratio between multiphoton absorption and avalanche ionization can be affected by the pulse duration [34]. The energy contained in the photo-generated plasma is then transferred back to the material via different physical relaxation mechanisms [5], causing

permanent structural modification within the focal region where the light intensities is above the non-linear photo-ionization threshold.

In general, FS pulses between ~100 – 500 fs are used for FBG inscription. Compared to picosecond (PS) pulses, the absorption of a FS pulse is decoupled from thermal effects since the lattice heating time is on the order of ps, allowing for a more precise machining. Further, since the peak power of PS pulses is lower, they are less likely to be absorbed non-linearly and the avalanche breakdown process is seeded by stochastic thermal electrons instead of multiphoton ionization. With shorter and more intense FS pulses, multiphoton ionization starts seeding the avalanche breakdown, making this process more deterministic and efficient [5, 34]. However, at very short pulse duration (< 10 - 100 fs), photoionization dominates avalanche ionization, and dispersion of the pulse in the beam delivery system can become an issue [5].

2.2.3 Types of femtosecond-induced refractive index modifications

Depending on the parameters of the plasma, the energy can be transferred back to the material via different physical processes of plasma recombination and heat diffusion, causing different types of RIMs. Naturally, many experimental parameters can affect the RIM formation, such as the pulse energy, pulse duration, repetition rate, wavelength, polarization, and numerical aperture of the objective. Yet, a parameter that has a big impact when processing pure fused silica with a standard FS system is the pulse energy [5], as it can be adjusted easily to achieve different types of RIMs.

At low pulse energies, just above the index modification threshold, a smooth and isotropic RIM is obtained, and the grating has low propagation losses. This type of RIM is typically referred to as a type-I modification [18, 35] and is commonly used to fabricate high-quality photonic devices. However, type-I FBG can be erased at relatively low temperature (around 200°C) [18]. In the case of intermediate pulse energies, anisotropic RIM and nanograting perpendicular to the laser polarization can start to form, causing birefringence in the grating. Finally, at high pulse energies, ultra-high pressures are generated in the focal point, creating a shock wave and the formation of micro-explosion and micro-void. This type of modification can produce very high RI change and is often called a type-II modification. It is usually associated with optical damage

and high scattering loss of the sample [5], but the gratings can withstand very high temperature (800°C) for several hours [18].

2.2.4 Refractive index modification by multiple femtosecond pulses

Instead of using a single pulse interaction to modify the RI of a given region in the sample material, it is possible to induce the modification by overlapping multiple pulses [5]. Multi-pulse approach has been used widely in the fabrication of Bragg gratings waveguides [36-38], for which it provides control over the physical size and the overlap of the RIM, the deposited energy, and where cumulative effect allows for a stronger RI change ($\overline{\Delta n_{eff}}$), with a spatially smoother distribution and lower propagation loss, while keeping the pulse energy well under the optical damage threshold of glass.

In this situation, the RIM is not only affected by the pulse energy, but also the repetition rate of the laser. In the case of a high repetition rate (>100 kHz), thermal accumulation can start to build up near the focal point, and the volume of the RIM increases over time. For lower repetition rates, the time between successive pulses is long enough to allow the heat generated by the plasma to be fully diffused away before the arrival of the next pulse. In this case, each pulse adds up to the cumulative effect independently. Of course, the threshold between a thermal vs. a non-thermal regime is highly related to the material being used.

2.2.5 Geometry of the focal spot and optical aberrations

For FS direct inscription, the 3D shape of the RIM that take place in the focal region is important to consider, as it is has profound impact on the grating coupling coefficients κ and σ, which are given by the overlap integral between the mode field and the cross-sectional shape of $\overline{\Delta n_{eff}}(x, y, \mathrm{z})$, as indicated in Eq. (2.12) and (2.13).

Ideally, the cross-section of $\overline{\Delta n_{eff}}(x, y, z)$ should be uniform across the fiber core (independent of x and y), or at least symmetric across the core. When $\overline{\Delta n_{eff}}(x, y, z)$ is uniform, the coupling coefficient only depends on the mode field overlap such as:

$$\sigma \propto \kappa \propto \iint_{-\infty}^{\infty} \vec{e}_{kt}(x,y)\, \vec{e}_{jt}^{*}(x,y)\, dy\, dz. \tag{2.31}$$

In this situation, the orthogonality relationship between the modes suggests that coupling is only allowed for identical counter-propagating modes, as it is the only case where the overlap integral is nonzero [17]. In practice, the approximation of a uniform RIM is often used for UV-based interferometric writing techniques but can't be used for FS direct-writing schemes. In the more realistic case where $\overline{\Delta n_{eff}}(x,y,z)$ is either off-centered or has a non-symmetric ellipsoidal shape, coupling to higher order modes and photo-induced birefringence becomes possible because of symmetry breaking, leading to a nonzero overlap integral [17, 39-44]. This situation also leads to an increase in the scattering losses. For different applications, these effects can be desirable or not, making it important to properly control, or at least understand the impact of the physical shape of the FS focal spot.

Since the RIM emerges from the nonlinear absorption of the laser, its spatial profile is highly related to intensity profile of the focal spot. Let's assume a laser beam that is focalized through the side of an optical fiber. To get a good representation of the focal spot, it is important to consider the optical aberrations that can affect the beam propagation from the laser to the fiber core center. Effects such as dispersion, diffraction, chromatic aberration, spherical aberration, nonlinear process (self-focusing, plasma defocusing, energy depletion) and the index mismatch at the air-fiber interface of the fiber are well described in [5]. Considering that chromatic aberration and spherical aberration can be mitigated be employing aspherical optics or aberration-corrected objectives, and neglecting the possible nonlinear interactions, the main cause of aberration still present is the index mismatch at the air-fiber interface. Since the fiber can be seen as small cylindrical lens, the focal point suffers from astigmatism, and most authors describe the light propagation using an astigmatic Gaussian beam model [39, 45-47], where the optical system is asymmetric around the optical axis. To be consistent with the coordinate system presented in Figure 2.1, note that the axis of propagation for the laser beam will be define along y. The elliptical intensity profile of a focussed astigmatic beam propagating along y can be described as [39, 47]:

$$I(x,y,z) = I_0 \frac{\omega_{0,z}\omega_{0,x}}{\omega_z(y)\omega_x(y)} \exp\left[-2\left(\left(\frac{z}{\omega_z(y)}\right)^2 + \left(\frac{x}{\omega_x(y)}\right)^2\right)\right], \tag{2.32}$$

with

$$\omega_z(y) = \omega_{0,z}\sqrt{1+\left(\frac{y-y_0}{y_{R,z}}\right)^2}, \qquad \omega_x(y) = \omega_{0,x}\sqrt{1+\left(\frac{y}{y_{R,x}}\right)^2}, \tag{2.33}$$

$$\omega_{0,i} = M^2\frac{\lambda}{\pi\,\mathrm{NA}_i}, \qquad y_{R,i} = M^2\frac{n\lambda}{\pi\,\mathrm{NA}_i^2}, \tag{2.34}$$

where I_0 is the normalized maximum intensity, M^2 is the beam quality, n is the refractive index of the glass, NA_i is the numerical aperture of each focussing axis (y and z), $\omega_{0,i}$ and $y_{R,i}$ are the focal beam waist and Rayleigh range, and y_0 is the offset distance between the focal position of each axis, called the astigmatism difference.

To better illustrate this concept, Figure 2.6 compares the beam propagation for the case where all optical aberrations are neglected to that where the focal point suffers from astigmatism. As shown in Figure 2.6 (a), the typical shape of a tightly focussed aberration-free focal spot is much smaller than the core area and its cross-section is usually asymmetrical in the xy-plane and elongated along the y axis. In Figure 2.6 (b), the refraction at the air-fiber interface leads to a splitting of the focal position between the two orthogonal focussing planes, with an astigmatism difference that can be estimated to 38 µm. This causes the focal spot to be distorted and elongated along the longitudinal z-axis [45, 48].

To mitigate the aberrations caused by the cylindrical shape of the fiber, methods based on immersing the fiber into an index-matching oil are commonly used. For example, a V-groove covered by a glass plate and filled with oil and can be used to hold the fiber [49-52], as illustrated in Figure 2.7 (a). Drawing the fiber through D-shaped glass ferrule filled with oil is another option [14, 53], as shown in Figure 2.7 (b). In both cases, the flat glass interface between the objective and the fiber makes the refraction homogeneous around the optical axis and the index-matching oil prevents further refraction at the fiber interface.

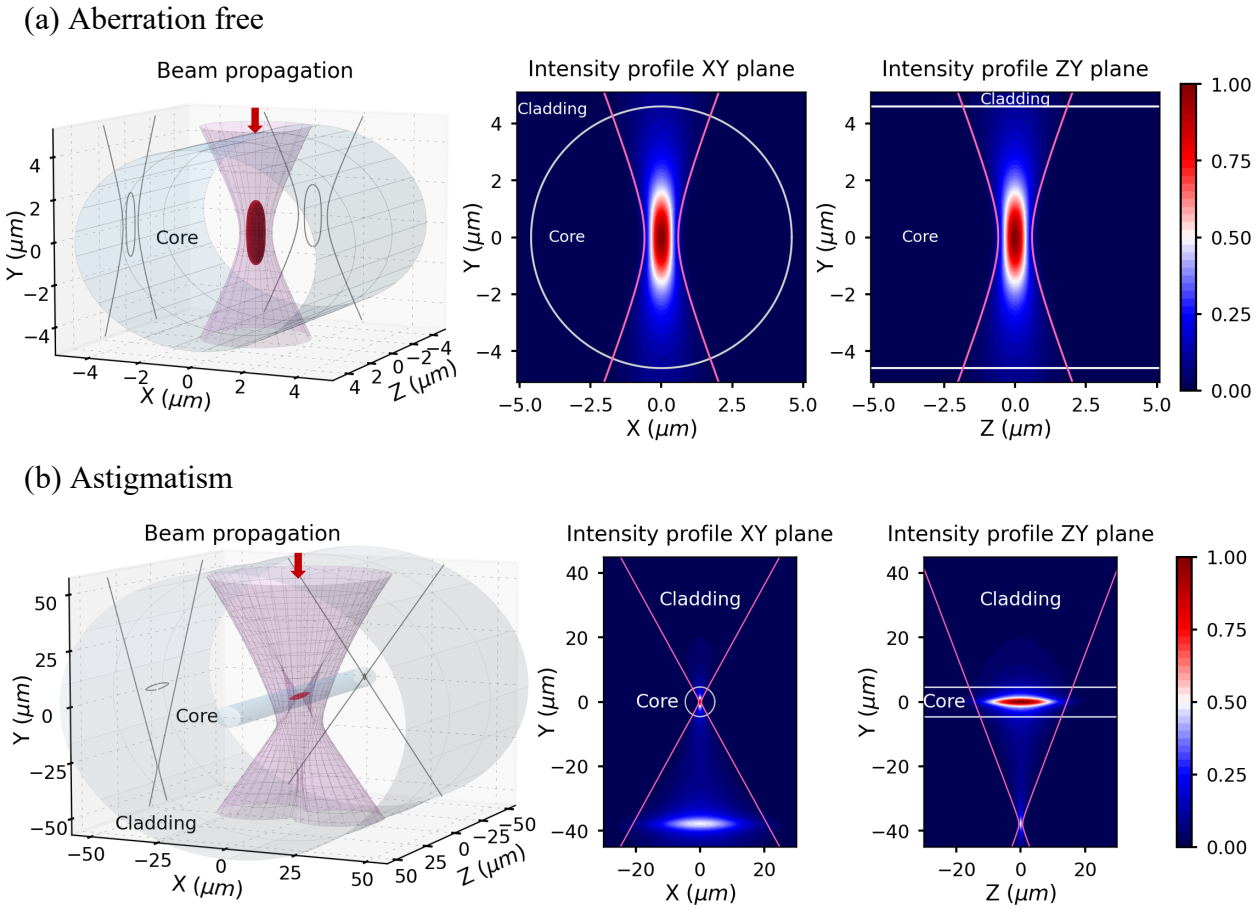

Figure 2.6: 3D Illustration of the beam propagation in an uncoated SMF-28 fiber. (a) All optical aberrations are neglected. (b) The refraction at the air-fiber interface is considered and the focal spot suffers from astigmatism induced by the fiber geometry. On the left, the 3D shape of the focal spot is represented by an ellipsoid showing the position where the intensity profile drops by a factor of two: $I(x, y, z) = I_0/2$. The beam waist size is illustrated in light pink. On the right, the cross-sections of the intensity profile in the xy and zy planes are shown. This simulation considers the geometry of an uncoated SMF-28 fiber with a RI of 1.45, an objective lens with a NA of 0.55 and a wavelength of 1030 nm. Using simple geometric optics arguments, the astigmatism difference between the focal position of both axis is $y_0 = 38$ µm.

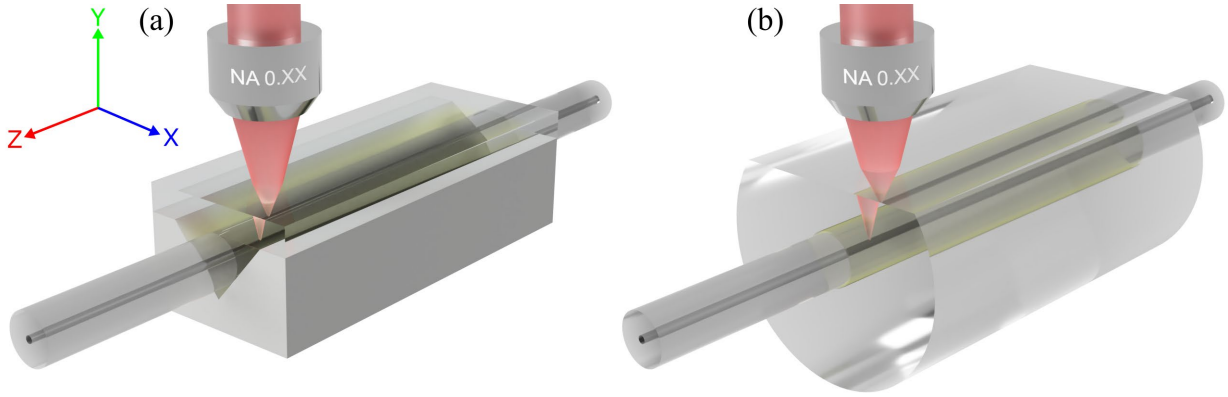

Figure 2.7: Index-matching oil immersion compensation techniques. (a) V-groove covered by a glass plate and filled with oil. (b) Glass ferrule with a polished flat side and filled with oil.

However, oil immersion compensation techniques are impractical from a manufacturing point-of-view, as the preparation of the fiber is more complicated, and the fiber must be cleaned afterward. The oil can also potentially degrade the coating or damage the silica cladding, and the additional required components (V-groove or ferrule) are usually not available off-the-shelf or may need a custom design for different fiber dimension. These constraints make it hard to scale up the fabrication process for high-throughput or for large scale FBG device. To avoid immersion oil, different beam shaping techniques can also be used. For instance, adaptive optics using spatial light modulator or deformable mirror [48], or astigmatism beam-shaping relying on a cylindrical telescope [45] have been used to correct the aberrations caused by the fiber geometry.

2.2.6 Beam shaping techniques

As its name suggest, beam shaping techniques can be used with FS laser micromachining to control the shape of the focal spot and the RIM spatial profile. For FS direct-writing, these methods have been used to correct for the astigmatism induced by the cylindrical shape of the fiber, to symmetrize the RIM cross-section, and to increase the dimension of the RIM cross-section to get a better overlap with the mode field.

There are many techniques to achieve beam shaping, but most of them rely on controlling the NA of both the z and x axis to adjust the beam waist of each axis independently. For example, astigmatic beam shaping [40, 45, 47] uses an arrangement of cylindrical lenses to control the NA ratio ($\mathrm{NA}_z/\mathrm{NA}_x$), or to adjust the astigmatism difference y_0 (see Eq. (2.33)). The slit beam

shaping technique [39, 46, 54] can also be used to achieve similar results by placing a rectangular slit in the beam path. This method is simple, as it does not require additional optical components to be aligned, but it is less adjustable compared to a system where fine tuning of the astigmatism difference is possible. Also, most of the laser energy is lost due to the small size of the slit. Another group of techniques uses adaptative optics to shape the beam wavefront [48, 55].

To illustrate how beam shaping can be beneficial, Figure 2.8 shows an example where the NA ratio is set to $\mathrm{NA}_z/\mathrm{NA}_\mathrm{x} = 10$. Compared to Figure 2.6 (a), the cross-section of the focal spot in the xy-plane covers a much bigger area of the core and is way more symmetrical. Even when considering the refraction at the air-fiber interface, the astigmatism has almost no effect in this situation because the beam waist size of the xy-plane is very large.

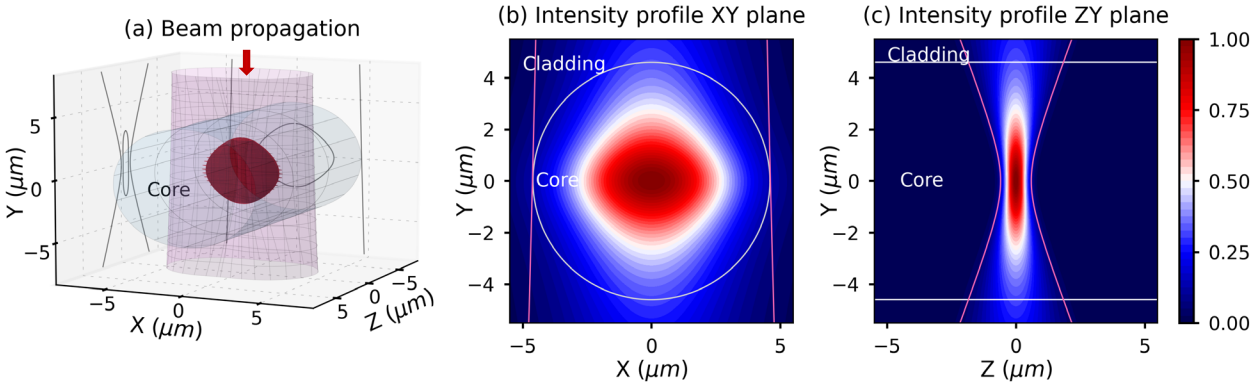

Figure 2.8: Representation of the focal spot obtain by using a beam shaping techniques where the NA ratio is $\mathrm{NA}_z/\mathrm{NA}_x = 10$. Information on the simulation model is given in 0.

2.3 Fiber Bragg grating fabrication techniques

In the present section, the conventional FBG fabrication techniques are reviewed. To produce high-quality FBGs, it is necessary to control the magnitude of the RIM ($\overline{\Delta n_{eff}}(z)$) with great precision and accuracy. High spatial resolution is also required because of the sub-micrometer spacing between each grating plane. For instance, an FBG with a reflection at a Bragg wavelength of $\lambda_B = 1550$ nm would require a period $\Lambda_g = 530$ nm, according to Eq. (2.3) and assuming $n_{eff} = 1.462$. For advance applications, a proper control of $v(z)$ and $\phi(z)$ is also needed, requiring an advance control system to accurately manage the relative position of each RIM.

In this context, laser-based techniques combined with high-precision motorized stage and optoelectronics systems are employed to photo-induced RIMs with sufficient precision. The fabrication techniques for FBGs can be classified in two main categories, namely, interferometric, and direct-writing techniques [29].

2.3.1 Interferometric writing techniques

Interferometric techniques have been refined since many years and are the most frequently used for industrial production of FBG. This group of techniques relies on the production of a periodic fringe pattern, which can be achieved by interfering two coherent beams. By exposing the core of an optical fiber to this periodic interference pattern, FBGs can be formed through different mechanisms of RI modification, as discussed in section 2.2. An exhaustive list and description of these techniques can be found in [11, 29].

Different types of laser sources can be used, such as CW or Q-Switched UV lasers, either in the format of gas or diode pumped solid-state lasers [11]. Since UV radiation is absorbed by polymers, the removal of the acrylate coating of the fiber is often required to allow the UV light to reach the core. However, usage of UV transparent coating has been reported [56], but is not very common. FS lasers at various wavelengths can be also employed with interferometric techniques, but the production of a high-quality fringe pattern is more difficult to achieve because of the short coherence length of such laser sources.

2.3.1.1 Phase mask

The operation principle of the phase mask technique [6, 29] is illustrated in Figure 2.9 where the incident laser beam is focussed in the fiber core with a cylindrical lens. Before reaching the fiber, a phase mask splits the beam into its different diffraction orders, $m = 0, \pm 1, \pm 2, \ldots$. As it stands today, most phase masks are designed to minimize transmission of the zeroth order and maximize the ±1 order. Near the phase mask, the interference of the overlapping ±1 diffracted orders produces a fringe pattern which is used to inscribe the FBG. The laser beam can be also scanned along the z axis to produce FBGs longer than the beam spot size [29, 57]. At normal incidence, the period of the fringe pattern (Λ_g) is related to the period of the phase mask (Λ_{pm}) by [29]:

$$\Lambda_g = \frac{m\lambda_B}{2n_{eff}} = \frac{\Lambda_{pm}}{2} \tag{2.35}$$

Because the phase mask technique is excellent for its simplicity, stability, reproducibility, and ability for mass production, it is attractive for industrial production of FBGs. The cross-section of the RIM produced by this method is also quite homogeneous and allows for high spectral quality, low coupling to cladding modes, low polarisation dependent loss, and low insertion loss [58]. However, since the grating structure is linked to the phase mask geometry, each grating design requires a custom phase mask, which can be expensive, difficult to fabricate, and limited in length. Therefore, writing behind the phase mask does not provide the same flexibility attributed to direct-writing techniques, which are explained in section 2.3.2.

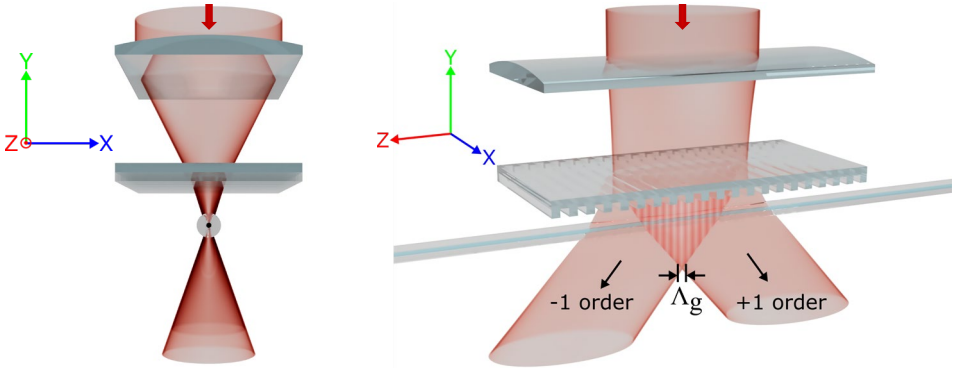

Figure 2.9: Illustration of FBG inscription behind the phase mask.

For FS writing, the phase mask technique is the most frequently used interferometric technique, as both the ±1 diffracted orders are spatially and temporally aligned, alleviating the difficulties caused by the short coherence length of FS pulses.

2.3.1.2 Talbot interferometer

Another writing scheme based on a Talbot interferometer [11] is illustrated in Figure 2.10, where a scanning phase mask (a) or phase modulators (b) are used to synchronize the position of the interference pattern with a moving fiber. Compared to the phase mask technique, this inscription method is much more sophisticated and can be used to fabricate gratings of any arbitrary length and with complex phase profiles. However, it requires a superior motion control system and additional optoelectronic components to maintain a perfect synchronization between the moving

fiber and the fringe pattern, which is crucial to fabricate FBGs with low phase errors. This continuous writing scheme is currently implemented at Polytechnique Montreal and was able to produce FBGs with outstanding quality [11, 12].

Both UV or FS lasers can be used with the Talbot interferometer technique, but the production of FBGs with this kind of setup is much more difficult to achieve with a FS laser [58]. As opposed to a CW or Q-switched UV laser, the short coherence length of FS lasers requires the Talbot interferometer to be extremely stable and the optical alignment to be perfectly executed in order to produce an interference pattern of good quality. The wide spectral width of the FS pulse leads to additional dispersion, further deteriorating the overlap of the interfering beams.

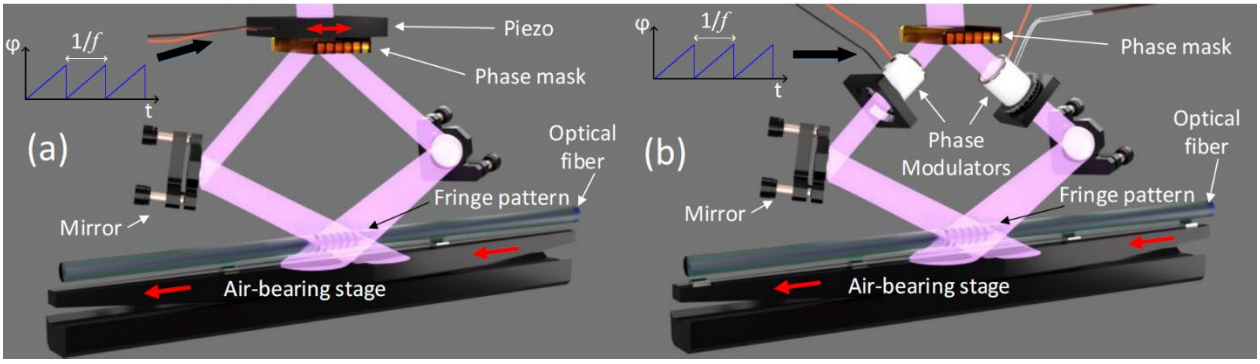

Figure 2.10: FBG writing using a UV laser with a Talbot interferometer. A) A phase mask stacked on a piezoelectric actuator is used to move the fringe pattern. B) Phase modulators are used instead. Reproduced with permission. © S. Loranger, 2018 [11].

2.3.2 Direct-writing techniques

Instead of writing the FBG with an interference pattern that imprints multiple fringes at once, direct-writing techniques, such as the point-by-point (PbP) [8], the line-by-line (LbL) [59] or the plane-by-plane (Pl-b-Pl) [40], consist of inscribing one RIM at a time, as illustrated in Figure 2.11. A good review of the different techniques is given in [58].

One of the main benefits of direct-writing techniques is their flexibility to control the exact position of each RIM. Hence, the grating parameters such as the Bragg wavelength, chirp, length, apodization profile or cladding mode coupling can be adjusted and reconfigured easily using direct inscription, which is not possible with the phase mask technique, where the grating design

is imprinted in the phase mask geometry [5]. Again, both UV and FS lasers can be used with direct-writing techniques as there is almost no difference in the working principle.

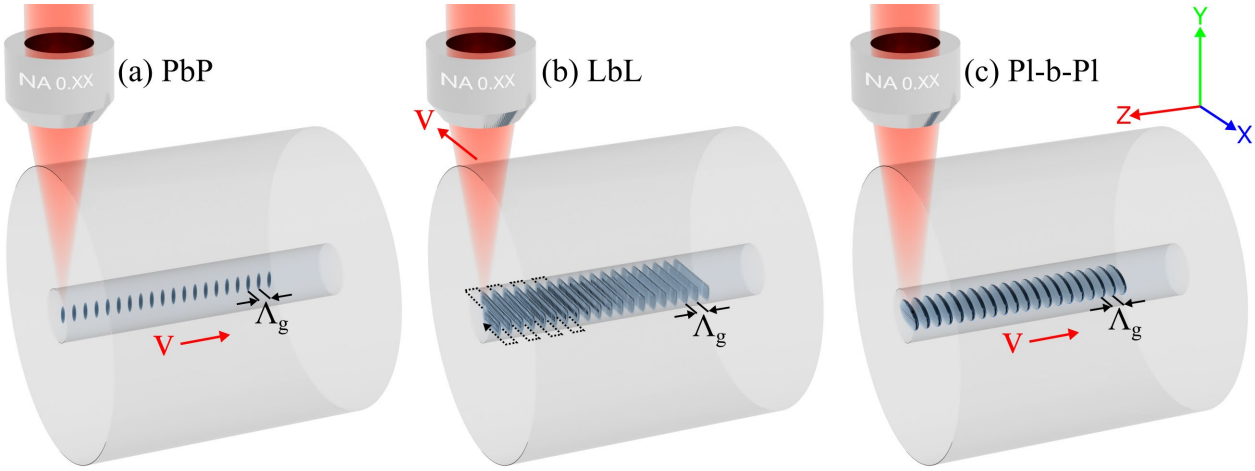

Figure 2.11: Illustration of the direct-writing techniques. (a) For the PbP method, the fiber is translated along its longitudinal axis and each RIM is formed by tightly focussing a FS laser pulse down the core. (b) With the LbL method, the laser beam is scanned across the transverse y-axis to create a line of RIM. Each line is spaced by Λ_g. (c) The Pl-b-Pl method is like the PbP, but additional beam-shaping elements are used to achieve a RIM that covers a larger area.

2.3.2.1 Point-by-point

The PbP method [8] is the most straightforward direct-writing approach, where each RIM is formed by tightly focussing a single laser pulse or a burst of pulses into the fiber core. To achieve a periodic spacing of Λ_g, the fiber is clamped to a translation stage whose motion is synchronized to the repetition rate of the pulsed FS laser. The process is illustrated in Figure 2.11 (a). Usually, high NA objectives are required to achieve a RIM with the proper sub-micrometer size. Because of this, the geometry of the RIM is asymmetric and overlaps poorly with the mode field, as shown in Figure 2.6 (a). Under these conditions, the RI must be modified by a very large amount to produce FBGs with a strong κ. High power density at the focal spot is required to do so and it can lead to type-II RIM with high scattering loss. The small size of the RIM also makes the PbP scheme highly sensitive to any misalignment between the focal point and the core. Another important aspect of the PbP method is the necessity to mitigate the astigmatism induced by the cylindrical shape of the fiber, as shown in Figure 2.6 (b). As noted previously, oil immersion

compensation techniques [14, 49-53] such as the ones illustrated in Figure 2.7 are a common solution, but different beam shaping techniques can also be employed [45, 48].

2.3.2.2 Line-by-line

The LbL method [59] is illustrated in Figure 2.11 (b). As its name suggest, each RIM is formed by scanning the laser in a linear motion across the transverse axis of the fiber. The shutter of the laser is then closed, and the fiber is translated to the next line position before the process is repeated. Each line is inscribed with a spacing of Λ_g. This writing scheme has the advantage to produce a more homogeneous RIM, which covers a wider area of the core. The increased overlap between the RIM and the mode field allows for a stronger κ, with lower insertion losses, polarisation dependent losses, photo-induced birefringence, and coupling to cladding modes compared to the PbP method. However, since the longitudinal position of the fiber must be at rest to inscribe each line, the LbL scheme is severely limited in terms of speed. Also, the same aberration correction techniques used for the PbP method are required. Another variant of the LbL scheme was also demonstrated in [49, 60] where the fiber core is exposed to a continuous sinusoidal scanning motion instead of a simple linear motion.

2.3.2.3 Plane-by-plane

Similar to the PbP writing scheme, the Pl-b-Pl method [40] relies on the implementation of additional beam shaping techniques to produce a more planar RIM instead of a point-like modification. By controlling the width and depth of the focal spot, the RIM can be made more circular and symmetrical, while covering a larger area of the core, as illustrated in Figure 2.11 (c) and Figure 2.8. Compared to the PbP method, this allows to significantly increase the overlap with the mode field, resulting in a stronger κ for the same energy density at the focal spot, making it easier to produce Type-I FBGs. The Pl-b-Pl method is also much faster than LbL, as the RIM is produced in a single step instead of a sweeping motion of the laser beam across the core. In comparison to both PbP and LbL, Pl-b-Pl achieves FBGs that show higher spectral quality, lower losses, and lower polarisation dependent effects. The focal distortion caused by the astigmatism aberration can also be mitigated without the use of index-matching oil, making it possible to inscribe FBGs in fibers that are free-standing in air.

As mentioned earlier, many beam shaping technique can be used to shape the focal spot into a plane. Astigmatic beam shaping can be achieved by placing a long focal length cylindrical lens [40] or by placing a cylindrical telescope [45, 47] in front of the focussing objective. The slit beam shaping technique has also shown great results [39, 46, 54].

2.4 Apodization of femtosecond laser inscribed FBG

In addition to the fabrication methods presented above, different apodization techniques can be implemented to produce non-uniform FBGs. This section reviews the techniques that can be incorporated specifically to FS fabrication methods, such as the phase mask or direct-writing schemes.

2.4.1 Phase mask apodization

For FBGs made behind the phase mask, the simplest apodization method would be to change the laser power while scanning the phase mask [61], or by using a simple amplitude mask in front of the phase mask itself [19]. However, the variation of the resulting average RI change also induces an undesirable non-linear chirp leading to an asymmetrical spectral response, as illustrated in Figure 2.3 (a). This can be mitigated by postprocessing the fiber with a secondary exposure through another amplitude mask [19, 62]. Alternatively, phase masks can be made with a variable diffraction efficiency [19, 63, 64] to control the visibility of the fringe pattern while maintaining a constant $\overline{\Delta n_{eff}}$ along the grating. This allows to inscribe FBG with a single exposure step instead of a two-step process. Those phase masks are produced by varying the duty cycle or the groove depth of the corrugations, but they are more difficult to produce and much more expensive than a simple amplitude mask [62].

2.4.2 Direct-writing apodization

For direct-writing techniques, different apodization methods have also been demonstrated. Using a PbP or Pl-b-Pl scheme, $\overline{\Delta n_{eff}}(z)$ can be controlled by adjusting the laser pulse energy along the fiber length [65, 66]. Similarly, the LbL method can inscribe apodized FBGs by varying the writing velocity [67] or the length [68] of each line to adjust to total energy deposited along the fiber, as shown in Figure 2.12 (b). A major disadvantage with these methods is the non-linear

relationship between the magnitude of the RIM and the exposure parameters, which requires establishing an empirical calibration between $\overline{\Delta n_{eff}}$ and pulse energy for the PbP methods, or between $\overline{\Delta n_{eff}}$ and the length of each line for the LbL method. Since this process depends strongly on the experimental parameters, variable results are to be expected when changing the experimental conditions, which is impractical from a manufacturing perspective. Ultimately, the precision and accuracy with which the apodization can be performed are limited by the calibration process itself, which is prone to errors and environmental perturbation.

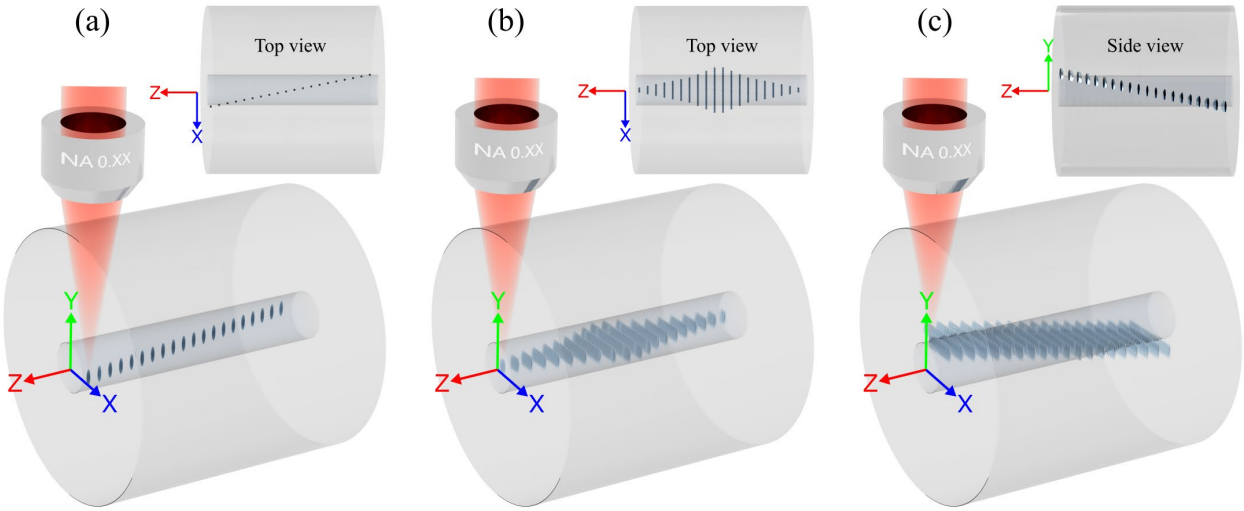

Figure 2.12: Different apodization techniques for direct-writing methods. (a) PbP apodization by transverse displacement of the focal spot. (b) LbL apodization by controlling the length of each line. (c) LbL apodization by transverse displacement of each line.

Another approach to apodize the grating is by varying the transverse position of the RIM from the center of the fiber core, as it was demonstrated using the PbP [14, 69, 70] or LbL [68] scheme. Figure 2.12 (a) and (c) shows an example of this method. For PbP, it is assumed that the focal spot is much smaller than the mode field and therefore κ, which is proportional to $\overline{\Delta n_{eff}}$, should varies approximately as a Gaussian function of the transverse displacement [70], such as:

$$|\kappa(\delta x, \delta y)| = \kappa_0 e^{-\left(\left(\frac{\delta x}{\omega/4}\right)^2 + \left(\frac{\delta y}{\omega/4}\right)^2\right)}, \tag{2.36}$$

where δx and δy are the transverse displacements, and ω is the $1/e^2$ mode diameter. However, this relation between κ and the displacement is only valid when the RIM is approximated as a

Dirac delta function. This limits the ability to use this model under different focussing conditions, such as with LbL and Pl-b-Pl, where the RIM is much bigger. In such situations, the dependency between κ vs the displacement could be evaluated using the overlap integral of Eq. (2.13), but this would not be very precise as the true shape of the RIM depends on many parameters and is hard to measure. Again, the practical solution would be to perform a calibration, which adds errors and is time consuming. In addition, lateral misalignment from core center can give rise to strong cladding mode resonance and birefringence [43], which is usually undesirable.

Despite the progress, all the apodization techniques mentioned above also have the major disadvantage of inducing a spatial variation in the average RI change, resulting in an asymmetrical spectral response.

2.4.3 Apodization by phase modulation

Apodization by phase modulation is another technique that is compatible with direct-writing techniques [71-73]. Due to its high flexibility and performance, this technique enables the fabrication of FBGs with arbitrary complex apodization profiles, which makes it possible to tailor advanced spectral functionalities. Previously, this method has been used for the apodization of waveguide Bragg gratings (WBG) [71-73] and FBGs made by UV continuous writing techniques [11, 19]. Surprisingly, it has not yet been demonstrated for the fabrication of FBGs using direct-writing methods. Since this will be the case in this thesis, let's describe the fundamental of this method and the benefits it can bring.

Instead of achieving apodization through the variation of $\overline{\Delta n_{eff}}(z)$, this method is based on modulating the phase of the grating with a periodic function of variable amplitude. As it will be demonstrated below, modulating the grating phase has the same effect as apodizing the grating visibility. This has a significant advantage as it maintains a constant average RIM, mitigating the challenge of handling highly non-linear RIM vs exposure parameters. By maintaining constant exposure parameters and focussing conditions, this method can target different apodization profiles with high precision and accuracy, as well as offering a spatial resolution down to just a few grating periods, which is essential for a precise control of the spectral response. This is because the precision/accuracy of this apodization method is only dictated by the ability to

inscribe a complex phase profile in the fiber instead of relying on the precision of the variation of $\overline{\Delta n_{eff}}(z)$.

Apodization by phase modulation is achieved by incorporating an additional periodic function with a slowly varying amplitude to the grating phase [71]. Doing so, the RI modulation of the grating can be written as:

$$\Delta n_{eff}(z) = \overline{\Delta n_{eff}}\left(1 + v\cos\left(\frac{2\pi z}{\Lambda_g} + \phi_g(z) + A(z)g(z)\right)\right), \tag{2.37}$$

where $A(z)$ is the slowly varying amplitude of the phase modulation and $g(z)$ is the additional periodic function of period Λ_ϕ. By assuming that $A(z)$ is approximately constant over a period Λ_ϕ, and by expanding $A(z)g(z)$ as a Fourier series, the RI modulation can be expressed as:

$$\Delta n_{eff}(z) = \overline{\Delta n_{eff}}\left(1 + v\sum_{m=-\infty}^{\infty} F_m(z)\cos\left(\frac{2\pi z}{\Lambda_g} + \phi_g(z) + m\frac{2\pi z}{\Lambda_\phi}\right)\right), \tag{2.38}$$

$$F_m(z) = \frac{1}{\Lambda_\phi}\int_0^{\Lambda_\phi} e^{iA(z)g(\mathrm{Z})}e^{-i2\pi m\mathrm{Z}/\Lambda_\phi}d\mathrm{Z}, \tag{2.39}$$

where F_m is the m^{th} Fourier coefficient, which depends on the choice of the periodic function g. It can be seen from Eq. (2.38) that the periodic modulation gives rise to new frequency components. The 0^{th} Fourier component ($m = 0$) is related to the main Bragg stop band, and the $\pm m^{th}$ components are optical superlattice sidebands, which appear in the spectral response as multiple peaks on both side of the main Bragg stop band. The wavelength spacing between each frequency component is given by:

$$\Delta\lambda = \lambda_B/\left(\frac{2n_{eff}\Lambda_\phi}{\lambda_B} + 1\right). \tag{2.40}$$

Most of the time, these sidebands are of no interest, and a sufficiently small period Λ_ϕ should be chosen to ensure they are outside of the optical operation band of the FBG. By considering only the 0^{th} Fourier component, the RI modulation can be simplified to:

$$\Delta n_{eff}(z) = \overline{\Delta n_{eff}}\left(1 + v\, F_0(z)\cos\left(\frac{2\pi z}{\Lambda_g} + \phi_g(z)\right)\right), \tag{2.41}$$

$$F_0(z) = \frac{1}{\Lambda_\phi}\int_0^{\Lambda_\phi} e^{iA(z)g(\mathrm{Z})}d\mathrm{Z}. \tag{2.42}$$

From Eq. (2.41), it can be seen that $F_0(z)$ acts as the envelope function of the grating, i.e. similar to the visibility. Hence, to achieve apodization, $F_0(z)$ should be equal to the normalized target apodization profile, $\kappa_n(z)$. This can be done by calculating the proper amplitude profile $A(z)$ for which $F_0(z) = \kappa_n(z)$. Of course, $A(z)$ will depend on the choice of $g(z)$, which can be any periodic functions (sinusoidal, square, sawtooth, …) [71].

For example, if $g(z) = \sin(2\pi z/\Lambda_\phi)$, Eq. (2.42) can be evaluated using a Bessel function, and $A(z)$ is related to the target apodization profile by an inverse Bessel function:

$$F_0(z) = J_0\big(A(z)\big) = \kappa_n(z) \;\rightarrow\; A(z) = J_0^{-1}\big(\kappa_n(z)\big), \tag{2.43}$$

where J_0 and J_0^{-1} represent the Bessel and inverse Bessel functions.

Once the amplitude profile of the phase modulation is calculated, the last step is to map the total phase of the grating to the physical distance between every laser-induced modification.

$$\Delta z_n = \Lambda_g\left(1 - \frac{\phi_{tot}\big(n\Lambda_g\big) - \phi_{tot}\left((n-1)\Lambda_g\right)}{2\pi}\right), \tag{2.44}$$

$$\phi_{tot}(z) = \frac{2\pi z}{\Lambda_g} + \phi_g(z) + A(z)g(z). \tag{2.45}$$

Δz_n is the n^{th} spacing between the grating planes, and ϕ_{tot} is the total grating phase.

A more visual interpretation of the process described above is presented in Figure 2.13, which shows an example for a Gaussian apodization and an exaggerated linear chirp of 75 nm/mm. First, the target apodization $\kappa_n(z)$ and phase $\phi_g(z)$ profiles of the grating are presented in Figure 2.13 (a). Then, by considering a sinusoidal modulation signal with period of $\Lambda_\phi = 10$ µm, the amplitude profile $A(z)$ can be computed from $\kappa_n(z)$ using Eq. (2.43). This modulation signal is

shown in Figure 2.13 (b). Finally, the prescribed distance between each grating planes is computed from Eq. (2.44), and is illustrated in Figure 2.13 (c).

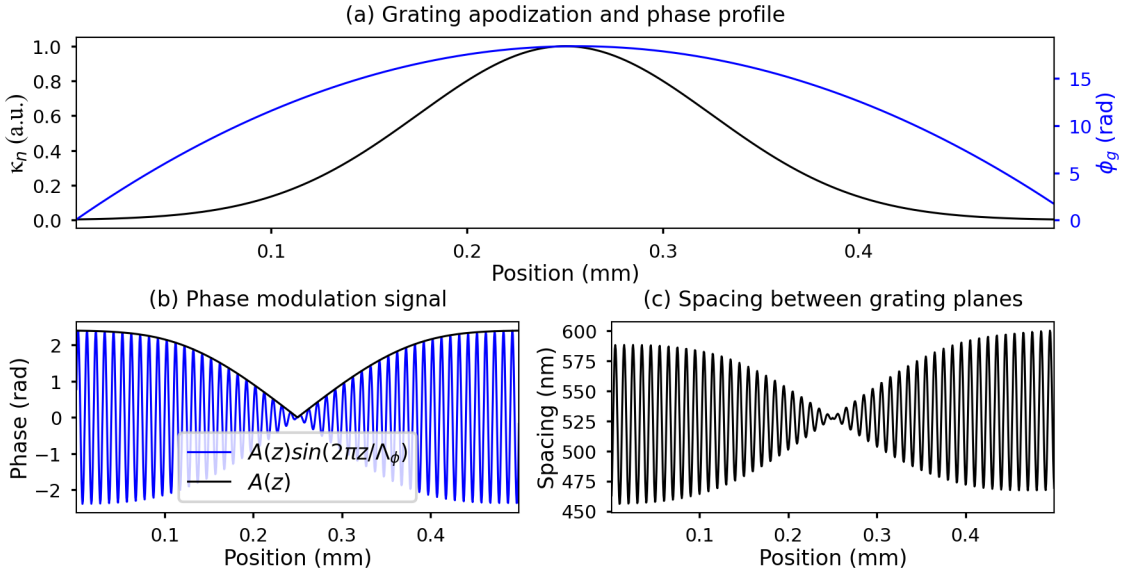

Figure 2.13: (a) Example of a Gaussian apodization profile and quadratic phase profile that produces a linear chirp over a distance of 5 mm. (b) To achieve apodization, a phase modulated signal, represented by the blue curve, is added to the total phase of the grating. The black curve represents the amplitude of the modulation. The sinusoidal function (blue curve) has a modulation period $\Lambda_\phi = 10\,\mu m$. (c) Corresponding prescribed distance between each RIM as calculated by Eq. (2.44). The spacing oscillates around 525 nm to target a central Bragg wavelength of 1550 nm.

2.5 Motion and phase control strategy

In order to fabricate high-quality gratings with complex phase profiles and low phase noise, a precise control of the spacing between each grating plane (i.e. the grating phase) is required. For example, Figure 2.13 (c) shows that phase modulation requires modulating the spacing between each of the grating planes, which can be difficult to achieve with high precision. This section discusses the different techniques that can be used with direct-writing to control the periodicity of the grating during the fabrication process.

The most basic way to control the position of each RIM is to stop the translation stage at each required position, and then trigger the laser. This method is mostly used with the LbL scheme

[59, 67], as the stage needs to be at rest before inscribing a line. It is very simple to implement, and the RIM position can be controlled with high precision and accuracy, which is mostly limited by precision of the stage itself. However, this method is significantly time consuming, as the stop-and-go motion requires many acceleration and deceleration events plus the time to stabilize the stage between each laser triggering events.

For the PbP or Pl-b-Pl schemes, the simplest and most efficient method to achieve a periodic spacing of Λ_g is to synchronize the motion of the translation stage to the repetition rate (f_{rep}) of the pulsed FS laser [5]. From Eq. (2.3), the relation between λ_B, f_{rep} and the translation speed (v) of the stage can be written as:

$$\lambda_B(z) = \frac{2n_{eff}}{m}\Lambda_g(z) = \frac{2n_{eff}}{m}\frac{v(z)}{f_{rep}(z)}. \tag{2.46}$$

To fabricate chirped grating with local phase variation, it was previously proposed to control the speed or acceleration profile of the translation stage during the inscription [49, 74]. However, due to the inertia and the limited acceleration of the stage, it can be hard to accurately predict the dynamics of its motion, which leads to errors in the RIMs positions [40]. Hence, the modulation of $v(z)$ limits the FBG phase profile to linear chirps or continuous and slowly varying chirps.

Instead of adjusting the speed of the stage, the repetition rate of the laser trigger clock can be modulated to control the longitudinal position of each RIM [14, 40]. This has the advantage of writing at constant velocity, but it requires additional electronics components. Because $f_{rep}(z)$ can be modulated much faster than $v(z)$, more complex phase profile can be implemented with this method. Nevertheless, for the two methods, the precision and accuracy of $\lambda_B(z)$ depends on the precision and accuracy of both $v(z)$ and $f_{rep}(z)$, and just a slight deviation of either of those parameters is enough to induce substantial phase noise and reduce the spectral quality of the grating.

2.6 Alignment consideration for direct-writing

When writing FBGs, it is important for the RIM to be well-centered with the guiding region of the fiber to ensure a good overlap between the RIM and the mode field [39, 40]. Referring to the

overlap integral of Eq. (2.13), we understand that the coupling coefficient κ is only maximized when the RIM and the mode field overlap perfectly. A highly accurate alignment is especially important for direct-writing methods, because the dimension of the RIM can be much smaller than the size of the fiber core, and any deviation from the core center can significantly reduce κ, induce spatial variation of κ, increase coupling to higher order modes, and increase photo-induced birefringence [17, 39-42]. Different applications can take advantage of these effects, reinforcing the importance of a proper control of the alignment.

The most common technique for alignment is to directly image the core of the fiber with a camera system [39, 40, 52, 75]. This can be achieved by incorporating a dichroic mirror in the optical path of the laser, as illustrated in Figure 2.14. With proper calibration and optical alignment, both the camera and laser can share the same optical path and focal point, and the core position can be tracked with high accuracy. However, the ability to visualize the core ultimately depends on the focusing condition of the optical system and the fiber properties such as the core-cladding RI difference, the core size, the presence of a coating, etc. In some cases, it can be quite difficult to visualize the core boundaries, for example if the core-cladding RI difference is too small, if the presence of a coating induces too much absorption, or if the focal point suffers from optical aberrations. This also means that the alignment process can lead to variable result with different types of fiber. Using a V-groove [49-51] or a drawing ferrule [14, 53] can also help to maintain a proper alignment, since fixing the position of the fiber alleviates the requirement of tracking the catenary shape it would take if it was freely-standing in air.

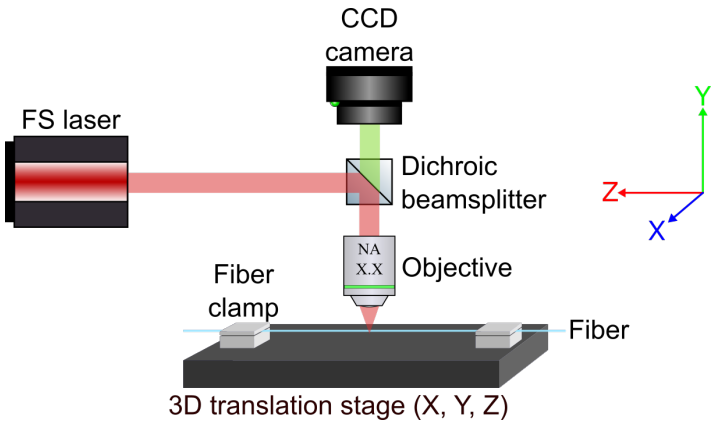

Figure 2.14: Representation of a direct-writing experimental setup, where the alignment between the focal spot and the fiber core can be monitored using a CCD camera.

2.7 Through the coating inscription

One of the main benefits of FS lasers is their ability to induce RI changes in material that are transparent and not necessarily photosensitive to the laser wavelength [5]. This gives the flexibility to choose between many available wavelengths to perform the inscription. Since many polymers absorb UV radiation, the protective coating of optical fiber must be removed when using UV lasers to fabricate FBGs. Stripping the coating makes the fibers more fragile, which reduces their overall mechanical strength and long-term reliability. This process is also time consuming, and re-coating of the fiber is usually required to ensure adequate protection, making the process undesirable from a manufacturing perspective and for mass production.

By exploiting an infrared (IR) FS laser, the process of fiber stripping and recoating can be totally avoided as most polymers are somewhat transparent to IR radiation [5]. As it stands today, FBGs inscribed directly through the protective coating of fibers have been demonstrated many times for both the phase mask [9, 76-79] and direct-writing [10, 45, 52, 53, 68, 80, 81] schemes, with very little degradation of the fiber integrity and strength. To do so, the laser has to be tightly focussed down the core of the fiber, so that the light intensity at the core is high enough to initiate non-linear absorption, but remains low enough when passing through the coating to avoid burning or damaging it [76]. Therefore, high NA focussing lenses are often used for through-coating inscription.

However, polymer coatings tend to suffer from nonuniformities such as thickness, curvature, or density variation along the length of the fiber. This can induce uncontrollable fluctuation of the focussing conditions and distorts the shape or position of the focal spot, reducing the quality of the spectral response [45]. To avoid these kinds of distortion, as well as the astigmatism induced by the cylindrical shape of the fiber, most of the standard methods listed above rely on oil immersion compensation techniques.

CHAPTER 3 DEVELOPMENT OF FEMTOSECOND DIRECT-WRITING SYSTEM

Since the manuscript [15] included in this thesis only contains an abridgment of methods, this chapter give additional details about the methodology used in conducting this research project. More specifically, it provides information about the components of the FS direct-writing system (optics, hardware, scientific instruments) that was developed, and describes important aspects of the FBG fabrication and characterization process. Details on how the data were gathered and analysed are also given. Overall, this introduces the findings and improvement that led to the publication of a manuscript and to the development of novel optical sensors and filters.

3.1 Experimental setup & writing scheme

The experimental setup that was developed to fabricate FBGs with a FS direct-writing scheme is represented schematically in Figure 3.1. An 8 W Pharos IR laser from Light Conversion is used. It has a wavelength of 1030 nm, a pulse duration of 250 fs, a beam diameter of 3.3 mm, and a repetition rate of 606 kHz which can be tuned with the embedded pulse picker. It was selected because of the possibility to inscribe FBGs directly through the polymer coatings of many optical fibers, which are transparent to IR wavelengths, as discussed in section 2.7. A beam expander is used to match or adjust the NA of the focussing objective, and a half waveplate and polarizing beam splitter cube are used to precisely adjust the laser power. The beam is focused into the core of the fiber through a plano-convex aspheric lens (Newport, NA = 0.55) that is mounted on a 2D (X, Y) air-bearing Aerotech translation stage. The fiber itself is clamped on a high-precision 1D (Z) air-bearing Aerotech translation stage, which is controlled by an interferometric laser-based encoder and has a maximum travel length of 1 m. To keep the fiber straight and reduce the sag of its natural catenary shape, a small tension is applied before clamping the fiber.

Two common types of fibers were regularly used to perform inscriptions: an uncoated SMF-28 fiber from Corning [82], and a polyimide coated SM1250(10.4/125)P fiber from Fibercore [83]. Their physical properties are listed in Appendix C. Through-the-coating inscriptions were performed using the polyimide coated fiber as its coating is thinner. The acrylate coating of the SMF-28 was stripped chemically with methylene chloride.

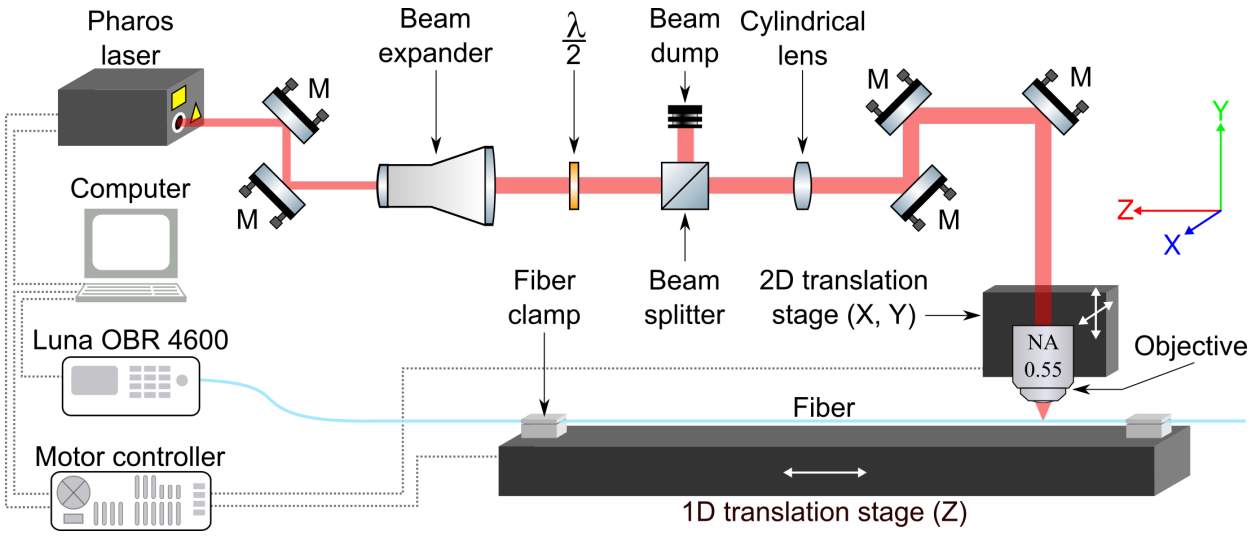

Figure 3.1: FS direct-writing experimental setup. The beam passes through a beam expander to match the objective NA. A half waveplate ($\lambda/2$) and polarizing beam splitter cube are used to adjust the power. A cylindrical lens with a focal length of 1 m is placed before the objective (NA = 0.55) to shape the focal spot to a plane. The fiber is held onto a 1D Aerotech stage with the help of clamps. The fabrication process is monitored using a Luna 4600 optical backscatter reflectometer (OBR). The gray dotted lines represent the electrical wiring used for communication between the equipment.

As described in section 2.3.2, a Pl-b-Pl writing scheme [40] was selected over the PbP or LbL schemes, as it provides a solution to mitigate the effect of astigmatism caused by the cylindrical shape of the fiber without having to use any index-matching oil compensation techniques, which would have been difficult to implement on this large translation stage. For example, since it was desired to be able to inscribe ultra-long FBGs (up to 1 m), the V-groove option was not practical, and drawing the fiber through a ferrule makes the fabrication process more complicated. The Pl-b-Pl scheme is also much faster than the LbL, and the increased overlap between the RIM and the mode field allows the production of stronger gratings, with lower IL and PD, as well as higher spectral quality than both the PbP and LbL approaches.

The beam shaping technique that was selected to shape the focal spot into a planar stripe is illustrated schematically in Figure 3.2 (a). It consists of placing a cylindrical lens with a long focal length in front of the focussing objective to reduce the size of the beam entering the objective along the x-axis [40]. By doing so, the NA of the focussed beam is reduced over the x-

axis ($\mathrm{NA}_x < \mathrm{NA}_z$), resulting in a focal spot that has a larger waist size and Rayleigh range compared to the z-axis ($\omega_{0,x} > \omega_{0,z}$; $y_{R,x} > y_{R,z}$). In this work, a cylindrical lens with a focal length of 1 m is used. Of course, other beam shaping techniques could have been employed to achieve this effect (see section 2.2.6), but the cylindrical lens method was the simplest to implement.

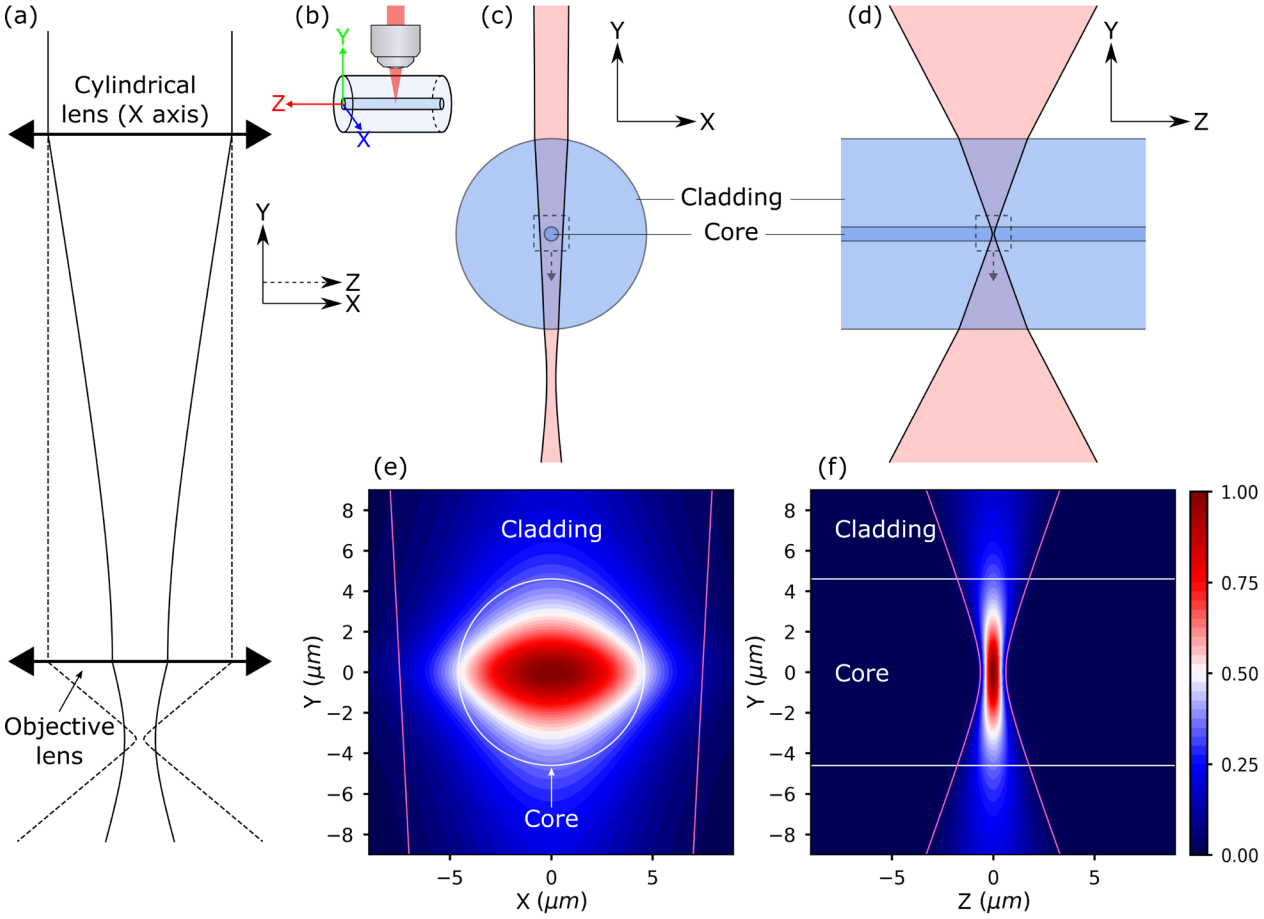

Figure 3.2: (a) Illustration of the long focal length cylindrical lens beam shaping technique. By positioning the focal point of the cylindrical lens directly on the objective lens, the size of the beam is reduced over the x-axis when entering the objective lens, lowering the NA, and increasing the beam waist size at the focal spot compared to the z-axis. (b) Coordinate system. (c)-(d) Beam evolution in the xy and zy planes of the fiber, calculated from the ABCD matrix method (see 0). (e)-(f) Illustration of the normalized intensity profile of the focal spot in both planes. This simulation considers a 1 m focal length cylindrical lens, a focussing objective with a NA of 0.55, $\lambda = 1030$ nm, the geometry of an SMF-28 fiber, and a RI of 1.45.

Assuming the experimental parameters indicated above, a simple ray transfer matrix analysis has been conducted to calculate the evolution of the Gaussian beam parameters as it propagates through the different elements of the optical system (See 0 for more details). Figure 3.2 (c)-(d) shows the beam propagation in the xy and zy planes as it passes through the fiber. It is worth noting how the refraction at the air-fiber interface impacts both focussing axes differently, inducing a large astigmatism. Using the beam parameters calculated with the matrix method, Figure 3.2 (e)-(f) shows the intensity profile of the focal spot as computed from the astigmatic Gaussian beam model given in Eq. (2.32)-(2.34). Since this setup contains many degrees of freedom, simulations considering different experimental parameters are also included in 0. Specifically, Table A.2 shows how changing the beam size, or the objective lens parameters can affect the focal spot, while Table A.3 shows how positional variation of the cylindrical lens can impact the beam propagation in the xy-plane.

3.2 Multi-pulse approach

An interesting feature of the Pharos laser used during this work is its burst mode, from which an exact number of pulses can be extracted by triggering the laser with an external signal. This allows to modify the RI of the fiber using a multi-pulse approach (see section 2.2.4), increasing the flexibility of the writing system. Hence, to control the coupling coefficient κ of the grating, two parameters were studied: The laser pulse energy, and the number of pulses per grating plane.

When using a burst of multiple low-energy pulses instead of a single high-energy pulse to inscribe the grating, it was found that it was possible to induce much stronger RI change while maintaining low insertion loss. With this approach, κ value of up to 600 m^{-1} could be achieved in an uncoated SMF-28 when using 200 pulses/plane, with out-of-band IL below 0.1 dB/cm. For comparison, the maximum κ value that was achieved with a single-pulse while still writing in a low-loss regime was about 200 m^{-1}. Since this discovery played an important role towards the realization of high-quality first-order FBGs, the results of the multi-pulse approach are presented in the manuscript of CHAPTER 4, where a complete study of the coupling coefficient and the IL as a function of the pulse energy and the number of pulses per grating plane can be found.

A distinction between single-pulse and multi-pulse system is the speed at which the translation stage can move. For a multi-pulse approach, it is important to keep writing speed low enough to avoid overlapping between adjacent RIMs. For this reason, the distance travelled by the stage during a single burst should be just a fraction of the grating period. The following equation has been derived to calculate the appropriate writing speed (v), as a function of the repetition rate of the laser (f_{rep}), the number of pulses per grating plane (N) and the fraction (in %) of the grating period travelled during a single burst, which is defined here as ξ. ξ is kept between 1-3%.

$$v = \xi \frac{m\lambda_B}{2n_{eff}} \frac{f_{rep}}{N}. \tag{3.1}$$

3.3 Phase control: Position synchronized output tracking

To control the spacing between each grating plane, different approaches compatible with the Pl-b-Pl scheme were presented in section 2.5. However, because of their limitation, it would have been difficult to use them to inscribe FBGs with any arbitrary complex phase profiles, since it requires a highly accurate control of the grating phase (i.e. spacing between the planes). For this reason, it was decided to investigate and implement a novel phase control strategy which relies on a special feature of the Aerotech motor controller: the position synchronized output (PSO) tracking [84]. This approach is far more sophisticated than the ones reviewed in Section 2.5, as it enables to control the grating phase with ultra-high resolution, while moving the fiber at constant speed. This allows to truly inscribe arbitrary complex apodization and phase profile, something that has been previously hard to achieve with FS direct-writing schemes.

As its name suggest, the PSO feature can be used to trigger all sorts of external hardware devices (camera, laser, sensor, data acquisition, etc.) based on the distance traveled by the stage instead of the amount of time passed. This process, which is illustrated in Figure 3.3, avoids trigger errors emerging from acceleration, deceleration, or other velocity instability of the stage. The PSO feature consist of two main elements: a distance counter and a pulse generator. The distance counter uses the closed loop feedback signal from the encoder of the translation stages to track the position of one or multiple axis (x, y, z). After a specified distance is travelled, the distance counter generates a firing event, which triggers the pulse generator to produce an electrical pulse

sequence at the output of the controller. In this work, this output signal is used to trigger the laser to emit a burst of N pulses at specific positions along the fiber.

Because of its high-speed (triggering at up to 12.5 MHz), low latency (120 ns), and the nm accuracy of the laser-based encoder, PSO tracking is well-adapted to the direct-writing of FBGs, as it allows to control the location of each laser spot accurately. Since variations in velocity do not affect the spacing between each laser firing event, this type of control increases quality and throughput when compared to control methods based on modulating the stage velocity or the laser frequency, or the ones relying on a stop-and-go motion (see section 2.5).

As illustrated in Figure 3.4, two operational modes have been implemented to generate different types of firing events. The fixed-distance firing mode uses the distance counter to generates firing events at fixed intervals, while the array-based firing mode uses a custom pre-programmed array of positions to specify the intervals between each firing event. This enables the flexibility required for the fabrication of uniform or arbitrary complex grating structures, which is one of the main goals of this thesis.

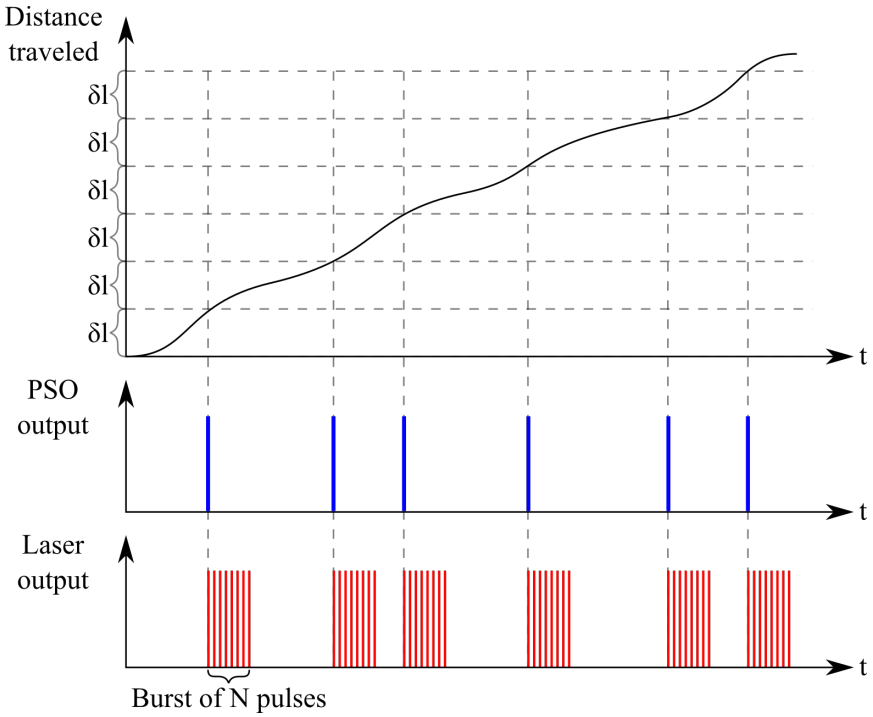

Figure 3.3: Illustration of the PSO output used to trigger laser firing based on the distance traveled (δl) instead of the time passed. The laser is programmed to emit a burst of N pulses at

each trigger event. Note that δl is the total distance travelled by the three axes of the translation stages such that $\delta l = \sqrt{\delta x^2 + \delta y^2 + \delta z^2}$.

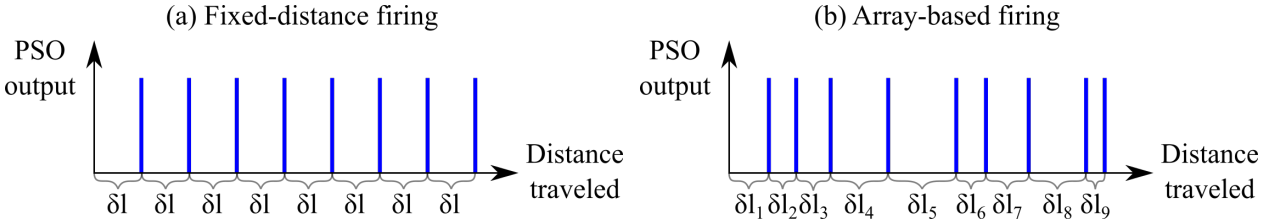

Figure 3.4: (a) PSO firing events generated at a fixed distance, enabling fabrication of uniform gratings. (b) The distances between firing events are specified in a custom array of positions.

3.4 FBG Characterization

Monitoring of the fabrication process and characterization of the resulting FBGs is performed by optical frequency domain reflectometry (OFDR), using a Luna 4600 optical backscatter reflectometer (OBR) system. OFDR systems use swept-wavelength coherent interferometry to characterize the full scalar response of optical components [85, 86]. Specifically, this technique measures the complex transfer function (i.e. spectral response), $H(\omega) = \rho(\omega)e^{i\phi(\omega)}$, of the device under test (DUT), which includes information about the amplitude (ρ) and phase (ϕ) response. By applying a Fourier transform to $H(\omega)$, the impulse response of the DUT, $h(t)$, can be also obtained. In the time domain (or spatial domain with a proper space-to-time mapping), $h(t)$ gives the information on the reflection as a function of the position in the device. With $H(\omega)$ and $h(t)$, all the useful characteristic of the FBG (group delay, instantaneous frequency, insertion loss, etc.) can be extracted in both the spectral and time/spatial domain. The OBR used in this work can operates over the C and L bands, from 1530 to 1620 nm.

In practice, measuring the reflection or transmission spectra of the DUT is quite simple with the OBR, and the characterization setup is shown in Figure 3.5. The IL can also be measured in both cases. In reflection, the IL is given directly by the "differential loss" returned by the OBR [87]. In transmission, the IL can be measured by subtracting a reference spectrum (taken before writing the FBG), to the sample spectrum.

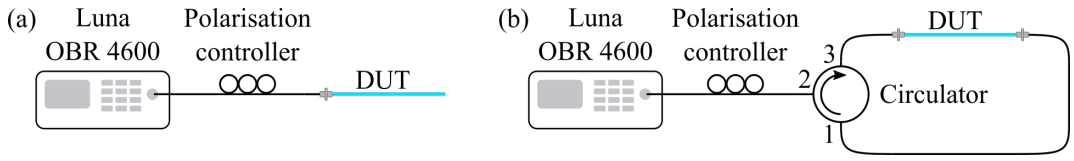

Figure 3.5: Characterization of the DUT in reflection (a), or transmission (b).

3.5 Alignment between the focal spot and the core center

As explained in section 2.6, the small size of the focal spot requires direct-writing methods to maintain a highly accurate alignment between the focal spot and the center of the fiber core to obtain a good overlap between the RIM and the mode field. Typically, this is done by employing a camera system to directly image the fiber core. Because the ability of such an imaging system to distinguish the core boundaries strongly depends on the experimental conditions and the physical properties of the fiber, any systematic change requires realignment and recalibration of the offset between the focal point of the camera and the laser, making this process tedious and prone to calibration errors.

Due to the limitations of this technique, a novel camera-free alignment method was developed during this thesis, with the ability to track the core position of almost any kind of fiber automatically and precisely, without requiring any calibration steps. The development of this method started out as a simple experiment to test if it was possible to track the position of the fiber core only with small probe gratings, instead of a having to setup a camera imaging system. It soon became clear that the goal of tracking the core position could be achieved with a surprisingly high resolution. Hence, the method was optimized, fully automated and was successfully used for the fabrication of all the FBGs made during this project.

In summary, the alignment method proposed in this work is based on optimizing the position where the objective lens (or focal spot) should be placed to maximize the coupling coefficient κ of a grating. This is done by writing a cascade of small uniform FBGs, called alignment probes, at various transverse displacements $(\delta x, \delta y)$ around the fiber core center, as illustrated in Figure 3.6. By measuring the strength of each probe with an OFDR system, we can find the position (x, y, z) where the focussing objective should be located to maximize κ, which corresponds to the position where the RIM is the most centered with the fiber core. Figure 3.7 shows an example of

typical outputs obtained from this alignment procedure, where the core position of both an uncoated SMF-28 fiber and a polyimide coated SMF-28 fiber was mapped over a length of 100 mm.

Because the core position of an optical fiber should vary smoothly, a low-pass filter is applied to remove the experimental noise from the position signal. However, care must be taken when choosing the cut off frequency of the filter. If it is too high, additional high frequency noise degrades the grating phase, while if it is too low, precious information about the core position can be lost. From this filtered signal, the alignment precision can be estimated by measuring the standard deviation of the residual noise. Typically, the standard deviation is found to be below 0.1 µm for an uncoated fiber, and below 0.25 µm for a polyimide coated fiber, making it possible to claim a sub-micrometer alignment precision over the x and y-axis.

Since the development of this method was a major part of this master's project and has proven to be effective, it is presented in the manuscript contained in this thesis. Further details can also be found in Appendix B.

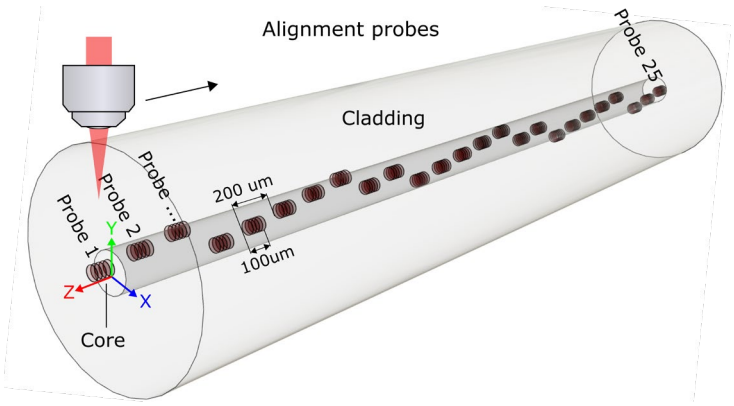

Figure 3.6: Several weak uniform FBGs are inscribed at various transverse displacement around the fiber core to serve as alignment probes. Each probe has a length of 0.1 mm and are separated 0.1 mm from each other. Their strength can be measured using OFDR.

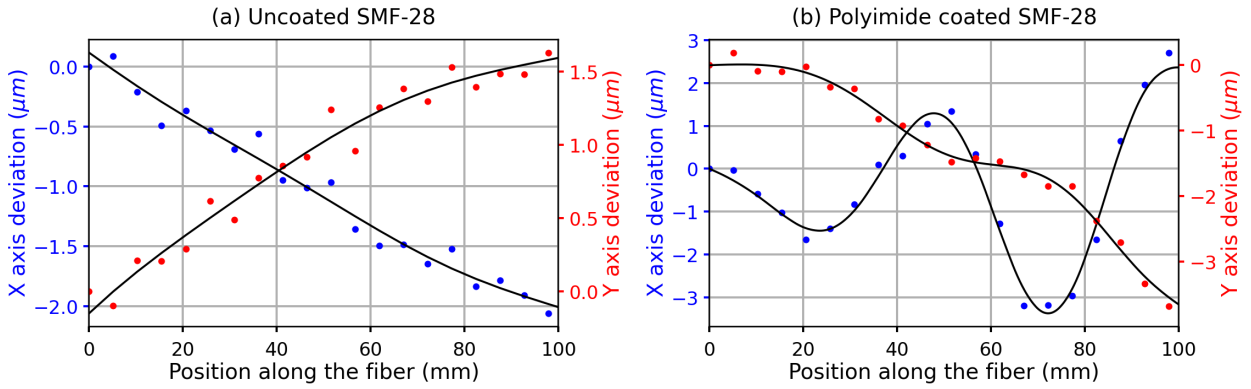

Figure 3.7: Fiber core position mapping for (a) an uncoated SMF-28 fiber and (b) a polyimide coated SMF-28 fiber. The deviation is relative to the initial position (x_0, y_0, z_0) of the focusing objective. The black curves show the data filtered with a low-pass filter.

3.6 Apodization

Even though many apodization methods have been demonstrated for the inscription of FBGs made by FS direct-writing (see section 2.4.2), the complexity to precisely control the amplitude of κ along the length of the grating and the difficulty to induce a constant average RI change have made it very challenging to perform high-quality apodization in a simple, reliable and efficient way. In fact, to be capable of writing any arbitrary complex apodization functions would require controlling κ with a much higher degree of precision and accuracy, and with much wider dynamic range than what is possible with the reviewed methods.

Towards this aim, a different approach based on phase modulation was explored. This apodization method, which is reviewed in section 2.4.3, has the benefits of maintaining a constant average RI change, while providing a high dynamic range and an extremely precise and accurate control over the amplitude of κ, making it ideal for realization of any arbitrary complex grating designs. However, despite its qualities, this method requires the ability to control the position of each grating plane with very high accuracy, as modulating the phase also induces a modulation of the planes position. This difficult constraint might be one of the reasons why this method has not yet been demonstrated with FS direct-writing scheme. To solve this problem, the phase control strategy based on PSO was developed, which was the key to implement apodization by phase modulation. By combining both methods, it became possible to inscribe any arbitrary complex

apodization and phase profile, making this technique one of the most advanced, yet simple apodization scheme.

Another interesting fact about this method is the ultra-high spatial resolution it can achieve. For example, complex apodization functions might, sometimes, contain sharp or even discontinuous variation of the coupling coefficient. These features can be difficult to resolve using traditional UV interferometric writing schemes, as the spatial resolution is limited by the area where the two interfering beams overlap, which is set to about ~100 μm for practical reasons [11]. However, with the phase modulation approach described above, the spatial resolution is limited by the period (Λ_ϕ) of the modulation, which can be set to just a few grating planes.

3.7 Simulation

After an FBG is fabricated, it is important to compare its response with a theoretical model to conclude if the fabrication process has been successful or to identify potential problems. Hence, a good simulation model is essential to validate experimental results, especially for complex structures.

During this work, the spectral response of the FBGs was simulated using a multilayer analysis, which is presented in section 2.1.3.2. This model was selected instead of the popular transfer matrix method of the coupled-mode theory (CMT-TMM) because it better represents the physical structure of FBGs made under the phase modulation approach. For example, when using the CMT-TMM, the first step is to discretize the grating profiles into many uniform subsections, which are then used for the calculation of the transfer matrix. However, when modulating the phase of the grating, the distance between each period is always varying, and the structure cannot be modelled as a stack of uniform FBGs described by the coupled-mode equations. For the multilayer analysis, the grating profile is first converted into a physical structure, consisting of a discrete array of distances between each grating plane. For the phase modulation method, these distances are calculated from the total phase of the grating, using Eq. (2.44) and (2.45). Then, this discrete physical structure is used to calculate the transfer matrix of the multilayer analysis, which is based on Fresnel equations instead of the coupled-mode equations.

3.8 Example of FBGs

Here are some examples of standard FBGs made with the methodology presented in this chapter. It demonstrates the ability of the writing system to inscribe various types of structure by comparing their spectral response to simulations. Figure 3.8 shows a uniform grating of 30 mm and Figure 3.9 to Figure 3.11 shows non-uniform gratings made with the phase modulation approach (Gaussian apodized, sinc apodized and linearly chirped FBGs, respectively), all with a length of 50 mm. In all cases, the measured spectral response correspond well to the simulation and low insertion loss < 0.1 dB/cm are observed. PD is also very low and is discuss in the manuscript.

Note this important detail: When a non-linear phase function is desired, such as for the chirped FBG of Figure 3.11, the amplitude of κ_n (normalized coupling coefficient) must be set to a value < 1. This is because the PSO feature can only send trigger signal at discrete values of the encoder position. For the translation stage that we use, the encoder resolution is set to 0.31 nm. This means that we can only increment the distance between each grating plane by this value, which is not enough to create chirped structures in a continuous manner. If we recall Eq. (2.43) the amplitude of the phase modulation is given by $A(z) = J_0^{-1}(\kappa_n(z))$. When $\kappa_n = 1$, $A = 0$. By setting $\kappa_n < 1$, we effectively "activate" the phase modulation since $A > 0$. This trick allows to slightly modulate the distance between planes around the desired period, and the averaging effect of the modulation makes it possible to effectively induce continuous chirp.

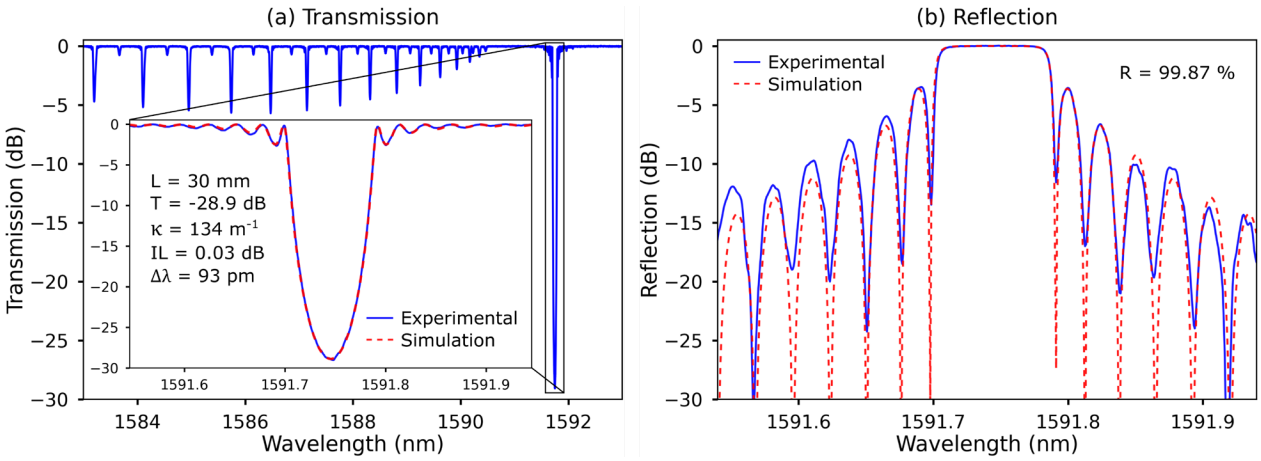

Figure 3.8: 30 mm uniform FBG, measured in transmission (a) and reflection (b).

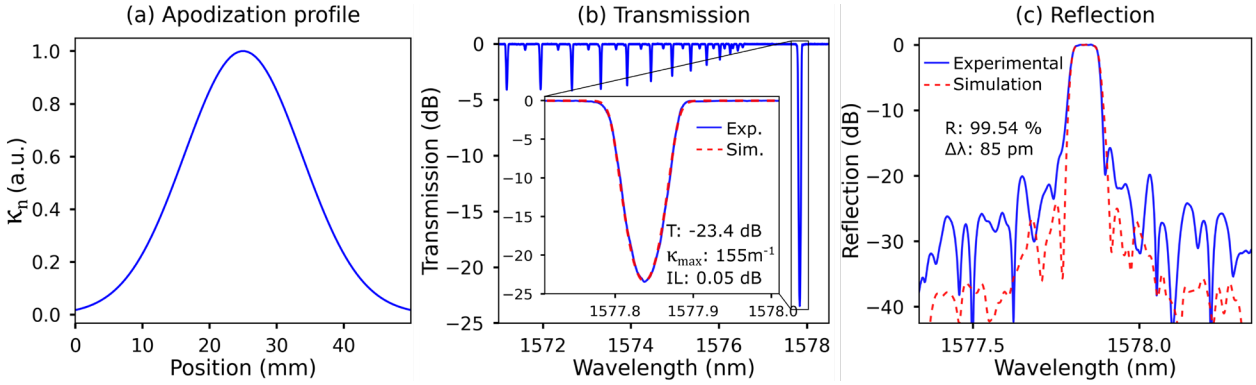

Figure 3.9: 50 mm Gaussian apodized FBG. (a) Normalized coupling coefficient. (b, c) Transmission and reflection

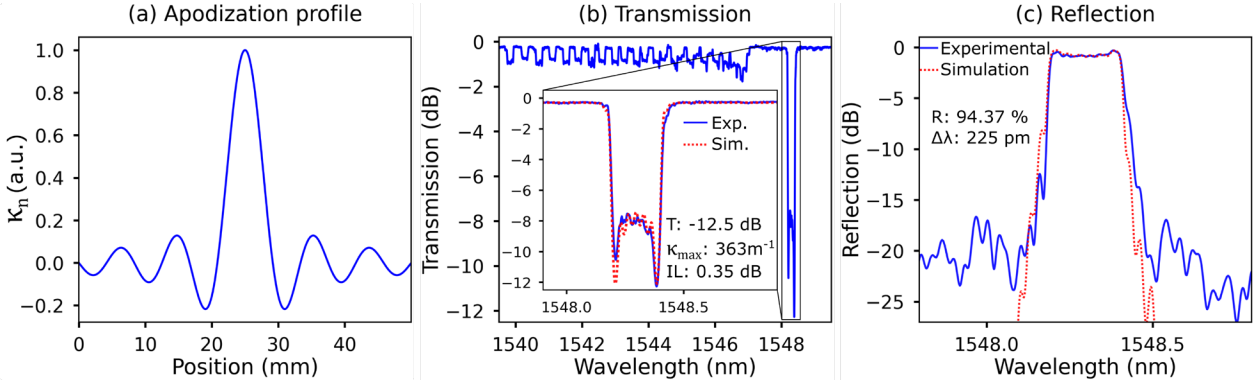

Figure 3.10: 50 mm sinc apodized FBG. (a) Normalized coupling coefficient. (b, c) Transmission and reflection

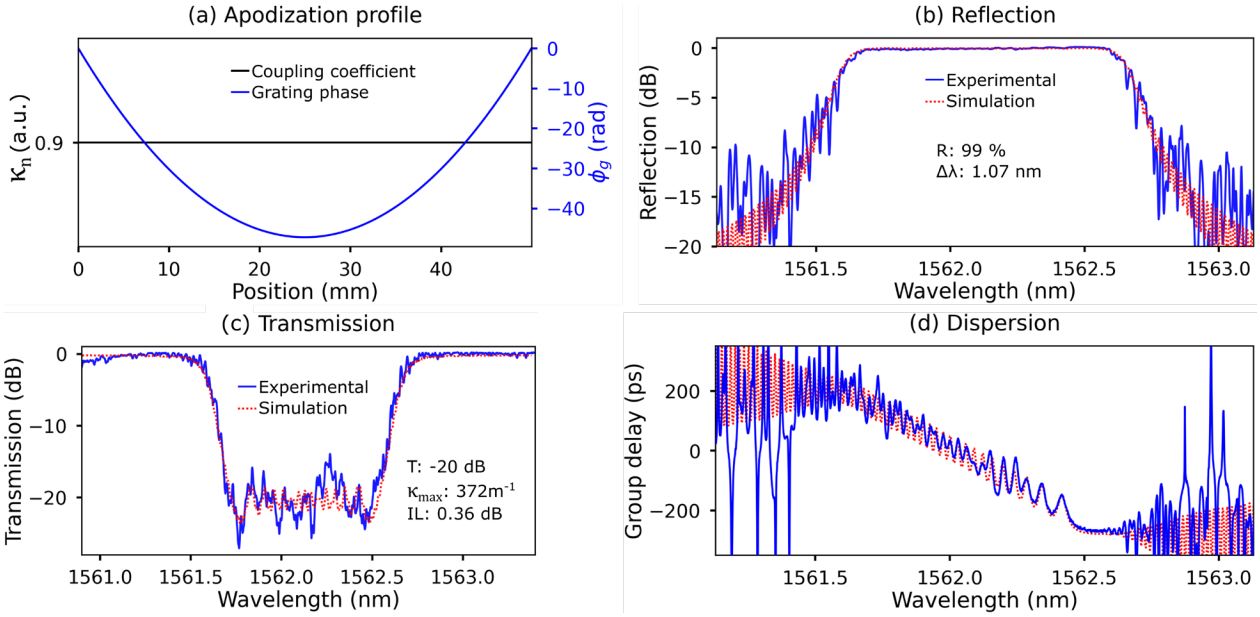

Figure 3.11: 50 mm linearly chirped FBG (0.02 nm/mm). (a) Normalized coupling coefficient and phase of the grating. A quadratic phase function is used to obtain a linear chirp. (b, c) Reflection and transmission. Note that the oscillations are expected since no apodization was applied. (d) Group delay. The slope is measured at -500 ps/nm, which corresponds to the design chirp of 0.02 nm/mm.

CHAPTER 4 ARTICLE 1: FEMTOSECOND LASER DIRECT-WRITING OF HIGH QUALITY FIRST-ORDER BRAGG GRATINGS WITH ARBITRARY COMPLEX APODIZATION BY PHASE MODULATION

Authors: Anthony Roberge[1], Sébastien Loranger[2], Jean-Sébastien Boisvert[1], Frédéric Monet[1], and Raman Kashyap[1,2]

[1]Department of Engineering Physics, Polytechnique Montreal, 2500 Chemin de Polytechnique, Montréal H3T 1J4, Canada

[2]Department of Electrical Engineering, Polytechnique Montreal, 2500 Chemin de Polytechnique, Montréal H3T 1J4, Canada

4.1 Foreword

This chapter consists of the manuscript [15] that has been accepted for publication in Optics Express, July 26, 2022. The work was realized using the methodology outlined in CHAPTER 3 and consists of the main findings regarding the development of a direct-writing method which can be used to inscribe first-order high-quality FBGs with arbitrary complex apodization and phase profiles using FS laser direct-writing.

4.2 Abstract

Femtosecond laser direct-writing is an attractive technique to fabricate fiber Bragg gratings and to achieve through-the-coating inscription. In this article, we report the direct inscription of high-quality first-order gratings in optical fiber, without the use of an index-matching medium. A new alignment technique based on the inscription of weak probe gratings is used to track the relative position between the focal spot and fiber core. A simple and flexible method to precisely control the position of each grating plane is also presented. With this method, periodic phase modulation of grating structures is achieved and used to inscribe arbitrary apodization and phase profiles. It is shown that a burst of multiple laser pulses used to inscribe each grating plane leads to a significant increase in the grating strength, while maintaining low insertion loss, critical for many applications.

4.3 Introduction

With their abilities to photo-induce strong refractive index modification (RIM) in a wide variety of materials and through the coating of fibers, femtosecond (FS) lasers have enabled the fabrication of fiber Bragg grating (FBG) with an extensive number of functionalities [10, 53, 58]. The phase mask [6] and direct-writing method [8] are the two most widespread techniques to inscribe FBG using FS lasers. While the phase mask technique is excellent for its simplicity, stability, reproducibility, spectral quality, and for mass production, it does not provide the same flexibility attributed to direct-writing methods [40, 58]. In particular, the requirement of a custom apodized phase mask [64, 88] severely limits the potential to quickly prototypes various complex grating design, as they can be expensive, difficult to make and are limited in length.

Instead of being imprinted in the phase mask, the grating parameters such as the Bragg wavelength, chirp, length, apodization profile or cladding mode coupling can be adjusted and reconfigured easily using direct inscription. However, several improvements are still needed to enhance the performance of the current fabrication methods. For instance, due to the small size of the laser focal cross-section, a highly accurate alignment between the focal spot and the fiber core is of crucial important to ensure a good overlap between the RIM and the mode field [39, 40]. Deviation from the core center can significantly reduce the coupling coefficient (κ), increase coupling to higher order modes and increase photo-induced birefringence [2, 39-42]. Alignment methods based on imaging the fiber core [52] can achieve good results, but often require some extra calibration steps for different types of fiber, which can yield variable result. Another attractive feature of direct-writing methods is their potential to fabricate any user defined structure. Even though many apodization [14, 65, 68] and phase control [14, 49, 67] schemes have been demonstrated, the ability to control amplitude and phase is not trivial, making it difficult to achieve high quality FBGs with true arbitrary complex profiles. Furthermore, despite the fact that FS direct-writing of first-order gratings have been demonstrated [40, 60, 89, 90], achieving high κ together with low insertion loss, low polarization dependency and low coupling to cladding mode has been difficult because of the tradeoff between pulse energy, grating visibility and scatter loss. To overcome these difficulties and the requirement of a sub-

micrometer RIM, many have resorted to writing high-order gratings [14, 48, 68, 89] with larger periods.

The aim of this article is to present a different approach that can be implemented with FS direct-writing techniques to improve the ability to fabricate high-quality first-order gratings with arbitrary complex apodization and phase profile. First, a novel alignment technique is proposed and demonstrated with the inscription of multiple weak probe gratings to map the position of the fiber core with respect to the laser focus. Then, we show that a burst of multiples pulses can be used to significantly increase the grating strength while maintaining low insertion loss and high spectral quality. Finally, we present how apodization by periodic phase modulation [71] can be used to control the amplitude of the grating with high precision and with a spatial resolution down to a few grating periods. To precisely control the position of each grating plane, a simple and efficient phase control strategy based on position synchronized output (PSO) tracking [84] is demonstrated.

4.4 Writing scheme

4.4.1 Experimental setup

The experimental setup used to fabricate FBGs by our direct-writing method is shown in Figure 4.1. A plane-by-plane (Pl-b-Pl) writing scheme [40] was chosen, as it allows for a larger overlap between the RIM and the mode field, which helps to achieve lower broadband losses, smaller coupling to cladding modes and higher grating strength [39, 40, 91] compared to the point-by-point (PbP) [8] or line-by-line (LbL) [59] techniques.

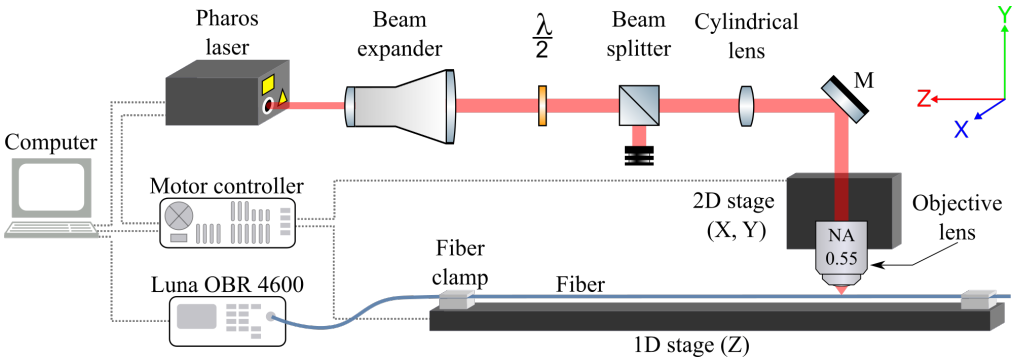

Figure 4.1: Experimental setup for direct-writing of FS FBGs. The beam passes through a beam expander to match the objective NA. A half waveplate (λ/2) and beam splitter are used to adjust the power. A cylindrical lens with a focal length of 1 m is placed before the objective (NA = 0.55) to shape the focal spot into a plane. The fiber is held onto a 1D Aerotech stage with the help of clamps. The fabrication process is monitored using a Luna 4600 optical backscatter reflectometer (OBR). The polarization of the laser is perpendicular to the longitudinal axis (z).

An 8 W Pharos laser from Light Conversion is used. The laser, operating at a wavelength of 1030 nm, has a pulse duration of 250 fs and repetition rate of 606 kHz which can be tuned with a pulse picker. The beam is focused through a plano-convex aspheric lens (Newport, NA = 0.55) that is mounted on a 2D air-bearing Aerotech translation stage. The fiber is clamped on a high-precision 1D air-bearing Aerotech stage which has a travel length of 1 m controlled by an interferometric laser-based encoder [12]. The inscriptions are performed over free-standing fibers and without index-matching oil. If needed, the coating can be removed using methylene chloride, followed by cleaning the fiber. A small tension (~150 g) is applied to the fiber to minimize its sag. A 1 m focal length cylindrical lens is placed before the objective to shape the focal spot into a planar stripe [40]. Much like the PbP approach, each plane is written in a single step, making the scheme faster than the LbL method [59, 60].

A multi-pulse approach is used, where each grating plane is formed with a burst of lower-energy pulses instead of a single high-energy pulse [5, 36-38]. The advantages of such method will be described in section 4.2. The writing speed is adjusted relative to the repetition rate and number of pulses per grating plane. It is set to keep the distance travelled by the stage during a single burst to a fraction of the grating period. Speeds of 0.03-0.3 mm/s are normally used.

All the FBGs reported in this work are written in the first order.

4.4.2 Phase control strategy

In order to fabricate gratings with complex spectral profiles, a precise control of the grating phase is required. For example, the method of apodization presented in this paper, i.e. phase modulation, requires a precise control over the position of each grating plane. For FS direct-writing many phase control methods have been proposed, each of them having their own limitations. For instance, controlling the speed/acceleration profile of the stage [49, 74] is limited to continuous and slow-varying chirps, modulation of the laser repetition rate [14, 40] requires additional electronics and is also limited in terms of phase control, and the stop-and-go scheme used with LbL method [67] is slow compared to PbP.

To address these limitations, the position synchronized output (PSO) feature of the motor controller is used to synchronize the triggering of a laser pulse (or burst of pulses for a multi-pulse approach) with the position of the stage, as it moves at constant speed [84]. The PSO functionality is provided with most of Aerotech motion controllers. It uses direct feedback from the encoder of the stage to track the position of multiple axis, and it sends trigger signals very precisely at specified positions, allowing precise control of the phase which is critical for the apodization method described in this work. This enables the fabrication of uniform or arbitrary complex grating structures.

4.5 Fiber core position mapping

4.5.1 Alignment principle

A common technique for fiber alignment is to image the core of the fiber with a camera system [39, 40, 52, 75]. With proper calibration and optical alignment, both the camera and laser can share the same optical path and focal point, but the ability to visualize the core ultimately depends on the focusing conditions and the fiber properties such as the core-cladding refractive index difference, the core size, the type of coating, etc. Using a V groove with a coverslip [49-51], a drawing ferrule [14, 53], and index-matching oil can help to maintain a proper alignment and to visualize the core, but these methods require additional custom components, and oil immersion can degrade the fiber and requires the fiber to be cleaned after the inscription.

The indirect alignment technique proposed here is based on optimizing the position where the laser focal spot maximizes the coupling coefficient κ of a grating. To do so, a cascade of small uniform FBGs, called alignment probes, are written at various transverse displacements around the core of the fiber, as shown in Figure 4.2-A. The probes are evenly spaced along the z-axis, within a characterization section which is assumed to be relatively uniform. The strength of the probes is orders of magnitudes weaker than the final intended grating, hence they do not affect its spectral response nor degrade the fiber. The relative strength of each probe, proportional to κ, is then measured using an optical frequency domain reflectometry (OFDR) system which can not only detect very weak scatter events, but also discriminate their positions along the fiber [87]. As the exposure is equal for all probes, variation in probe signal is proportional to the overlap between the focal spot and the mode field. Therefore, this signal should vary approximately as a Gaussian function of the transverse displacement [70].

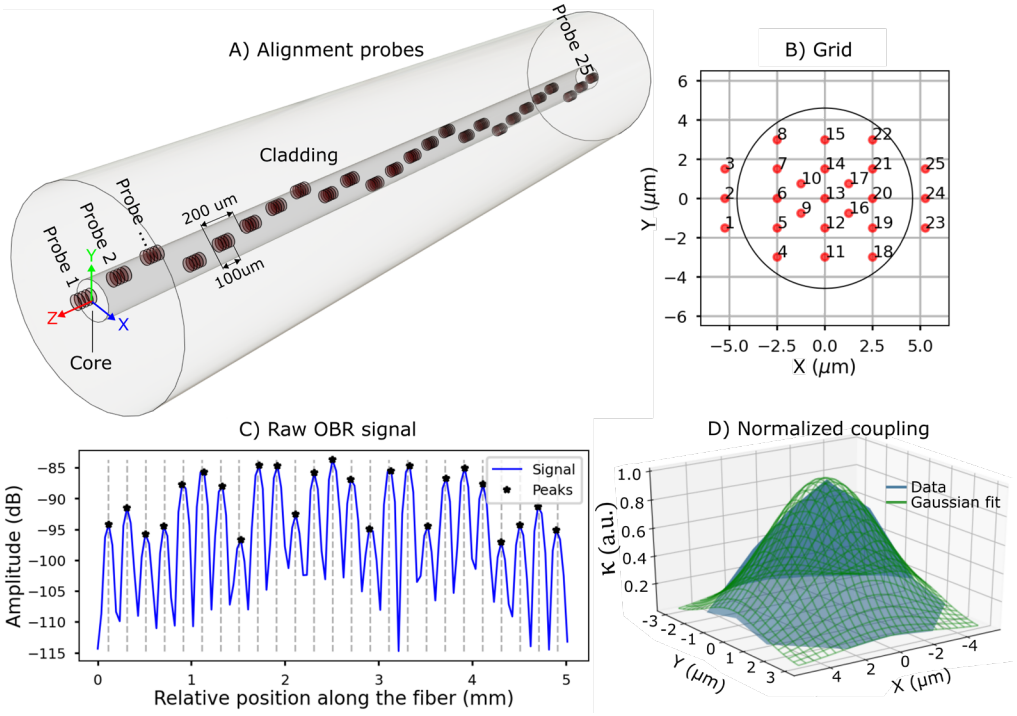

Figure 4.2: A) Illustration of the alignment probes, consisting of several uniform FBGs. Each probe has a length of 0.1 mm and are spaced 0.1 mm from each other. B) Grid that represent the position of each probe in the transverse plane (x-y) of the fiber. The circle depicts the mode field diameter of an SMF-28 fiber. The numbers represent the longitudinal order (along z) in which they are inscribed. C) Spatial impulse response acquired by the OBR for one iteration of the

mapping process (25 probes). Each peak corresponds to one probe for which the amplitude is proportional to κ. D) The same data can be rearranged into a 2D map representing the normalized peak amplitude of each probe in the iteration, for which a Gaussian fit can be applied to find the center point. Each iteration takes about 20 seconds, repeated every 5 mm.

Inscription of alignment probes in a single characterization section is shown schematically in Figure 4.2-A, where 25 alignment probes are written near what is thought to be the center of the fiber. The probes are 100 μm long and are separated from each other by 100 μm, resulting in a mapping resolution along the longitudinal axis of the fiber of 5 mm. To ensure uniform RIM and avoid a slight effective index modulation, exposure is kept constant even between the probes. Probes are switched ON/OFF by apodization, which is explained later in the article. The relative position of each probe forms a 2D grid which cover the whole core of the fiber, as shown in Figure 4.2-B. The spatial measurement of the strength of the probe FBGs by OFDR is shown in Fig. 2-C. The peak amplitude of each probe is then rearranged in 2D where a Gaussian curve can be fitted to find the position of best alignment, as shown in Fig. 2-D. This procedure is then repeated automatically with the help of an in-house software until the whole region of interest of the fiber is mapped. Note that the initial position of the focal spot must be within ~10 μm from the core position to get a signal. It can be found by inscribing trial probes over a larger area than the grid of Figure 4.2-B.

4.5.2 Mapping result

Using the alignment procedure and experimental setup presented in Figure 4.2, the fiber core position of both an uncoated and a polyimide coated SMF-28 fiber were mapped over a length of 500 mm. Both fibers were free standing in air (no index-matching medium). Figure 4.3 shows the alignment position, where a low-pass filter is used to remove the noise in the position signal.

In the case of an uncoated fiber (Figure 4.3-A), the geometry of the fiber is usually found to be very uniform along its length, and the core position varies smoothly with respect to the laser focal spot. The core can be tracked with sub-micrometer precision, as the residual standard deviation of the signal noise is below 0.1 μm for both the x and y axis.

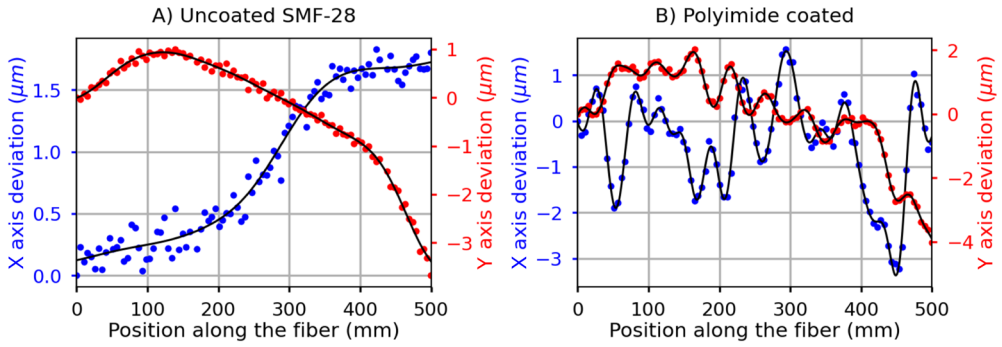

Figure 4.3: Mapping of the core position of two different fibers. The mapping is presented as a relative deviation from the initial position of the focusing objective. The raw data is filtered with a low-pass filter. A) Uncoated SMF-28. B) Polyimide coated SMF-28 fiber.

This high level of precision becomes critically useful with a coated fiber where strong oscillations of a few µm can be observed (Figure 4.3-B) as a function of the position. These are attributed to the inhomogeneous nature of the polymer coating, which is prone to significant thickness and curvature fluctuations along the fiber, thus creating optical aberrations of the focal spot shape and position. This is especially true in an air-based system, where the refractive index mismatch is large. Nevertheless, it is still possible to track the slow fluctuations of the core position of coated fibers with high accuracy. However, it should be noted that this tracking does not correct for focal spot shape distortion, which adds amplitude and phase noise to the grating while writing through a polyimide coated fiber, making it more difficult to inscribe high-quality grating over long lengths.

4.6 Grating fabrication

4.6.1 Uniform grating

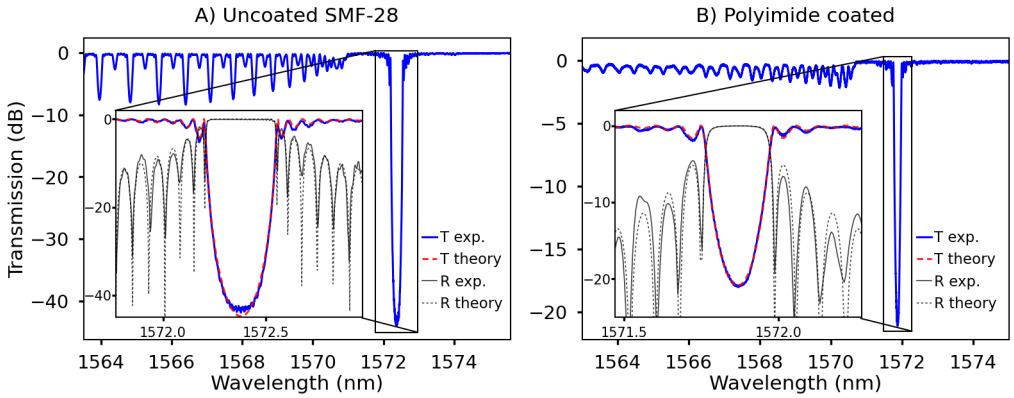

Figure 4.4: Experimental (Exp.) and theoretical (dashed lines) spectra of the transmission and reflection of 10 mm long FBGs made in an uncoated (bare) SMF-28 fiber (A) and a polyimide coated fiber (B), the latter being written at the maximum energy without damage to the coating.

To demonstrate the performance of our writing scheme, we start by showing the reflection and transmission spectra of uniform FBGs in Figure 4.4. Two first-order gratings were inscribed in both an uncoated SMF-28 (Figure 4.4-A) and a polyimide coated SMF-28 fiber (Figure 4.4-B). They had a length of 10 mm and a central wavelength of 1572 nm. The grating fabricated in the uncoated SMF-28 was written at a speed of 60 $\mu m/s$, using a laser repetition rate of 606 kHz, a pulse energy of 270 nJ (measured before the objective) and with a burst of 150 pulses/plane. The grating made through the polyimide coating was written at a speed of 15 $\mu m/s$, a laser repetition rate of 60.6 kHz, a pulse energy of 290 nJ and with a burst of 50 pulses/plane. When writing through the coating, a slower repetition rate is used to prevent heat accumulation effects, which degrade the coating and spectral response. The dashed lines show the theoretical response for a uniform grating, fitted to the data.

The FBG spectra shown in Figure 4.4 are strong ($\kappa L > 3$), with a very symmetric and high-quality spectral response, as can be seen from the excellent agreement between the experimental data and the theoretical fits to the spectra. The resulting coupling coefficients κ for both FBGs, calculated from their peak reflectivity [16], are respectively, 575 m^{-1} and 308 m^{-1}. Out-of-band insertion loss of < 0.1 dB is measured for both the uncoated and coated grating. A more detailed

characterization of the insertion loss is given in the next section. As seen from Figure 4.4, strong coupling to cladding modes can be observed. This is expected as the laser focusing condition used in this work produces an asymmetrical RIM that does not cover the entire core cross section [39]. However, we believe coupling to cladding mode can be further decreased by modifying the focal spot geometry with additional beam shaping techniques [39, 45, 47, 48, 54].

Figure 4.5 shows the polarization dependence of a 10 mm FBG with a transmission dip of -25 dB, made under similar conditions. The birefringence (Δn_B) is measured at 6.2 x10^{-6} RIU, which is near the intrinsic birefringence of SMF-28 (10^{-6} RIU), and therefore at the limit of our measuring capability. This confirms low polarization dependency of the Pl-b-Pl scheme.

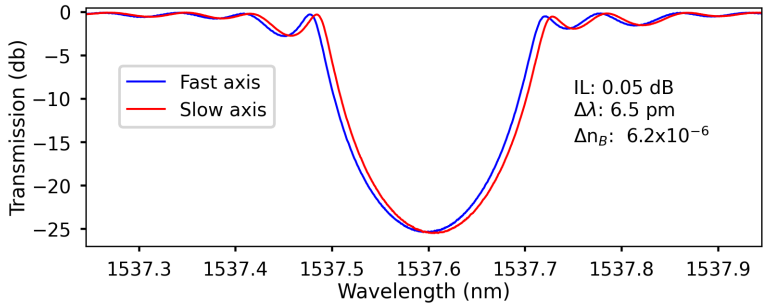

Figure 4.5: Polarization dependence of a uniform FBG made with the Pl-b-Pl scheme and a burst of 150 pulses/plane.

4.6.2 Single-pulse vs. multi-pulse approach

Multi-pulse approach has been widely used in the fabrication of Bragg gratings, waveguides, and the combination the two [5, 36-38]. It provides control over the physical size and the overlap of the RIM, the deposited energy, and cumulative effect allows for a smoother RIM, with stronger refractive index change and lower loss, while keeping the pulse energy well below the damage threshold.

To understand how the multi-pulse approach affects the refractive index change, κ was measured as a function of the pulse energy and for different number of laser pulses per grating plane. This was done by writing several FBGs in both an uncoated SMF-28 fiber and a polyimide coated fiber, the results of which are shown in Figure 4.6-A-B. In all cases, κ grows with the pulse energy up to a certain threshold (indicated with dashed lines) where a local maximum can be

observed. This is followed by a local minimum (or small plateau as shown in the inset of Figure 4.6-A). This type of transition was also observed in [38], but the exact mechanism responsible for it is still being investigated. When writing with pulse energies below the transition, high spectral quality and low insertion loss are observed, while writing above this transition yields lossy grating (several dB/cm), as shown in Figure 4.6-C-D, with a deterioration of the spectral response (See Figure D.1 in the supplementary material, found in Appendix D). We believe this threshold could be caused by a transition from type-I to type-II structures, usually associated with optical damage and high scattering loss of the sample [38].

To arrive at a better understanding of the losses induced by this writing scheme, Figure 4.6-C-D show the out-of-band insertion loss measured for FBGs written at pulse energies above and below the transition and for different number of laser pulses per grating plane. This was measured by subtracting a reference transmission spectrum from the sample spectrum and by evaluating the average loss for wavelengths above the Bragg wavelength. In both types of fiber, low insertion losses < 0.1 dB/cm were measured for pulse energies below the transition, which is in good agreement with the loss measured in [40], even for high κ value.

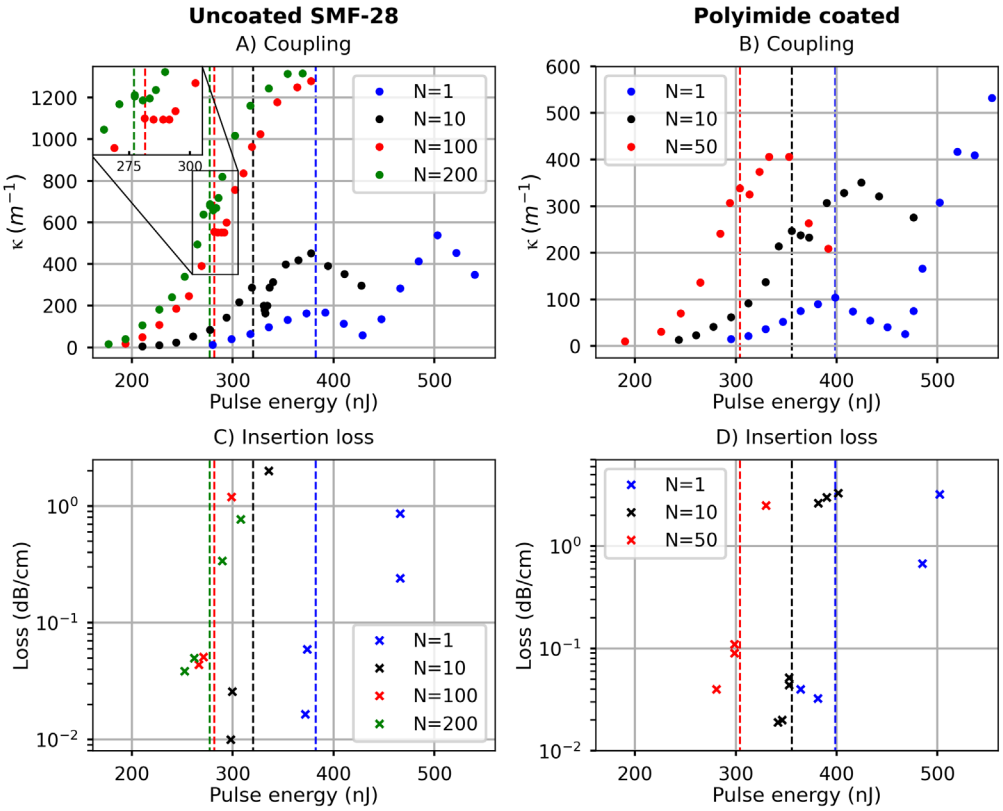

Figure 4.6: A) and B) Coupling coefficient for FBGs inscribed as a function of the pulse energy and the number of pulses per grating plane (N). The dashed lines indicate the pulse energy threshold where a transition between two writing regimes can be observed. C) and D) Out-of-band insertion loss for FBGs inscribed above and below the transition pulse energy threshold as indicated by the dashed lines. The study was made using both an uncoated SMF-28 fiber (A and C), and a polyimide coated SMF-28 fiber (B and D).

Most interestingly, this experiment suggests that the multi-pulse approach can increase the maximum κ value at which low-loss gratings can be inscribed compared to what is possible with a single pulse. With lower energy pulses, the focal region where the light intensity is just above threshold for RIM is reduced. Unfortunately, this also reduces the Fourier component of the fundamental period. With each additional pulse, the RIM region expands through nonlinear multiphoton absorption, as well as from the total fluence, increasing the κ value. This improvement emerges from the cumulative effect of multiple pulses. On the other hand, a single high intensity pulse being closer to the damage threshold of the fiber is more likely to lead to

Type-II grating very quickly. Further studies are in progress to clarify the physical mechanisms contributing to this improvement and will be reported on in a future publication.

When writing through a polyimide coating, we note that it was not possible to obtain a κ value as strong as for the uncoated fiber before observing a degradation of the spectral response and higher losses. A different focusing arrangement may of course, be used to optimize the RIM cross-section or make a better overlap to begin with using a single pulse, and hence increase the kappa values even more. This could be achieved with advanced beam shaping techniques [39, 45, 47, 48, 54].

4.7 Apodization by phase modulation

4.7.1 Apodization

For FS direct-writing, various amplitude apodization techniques were previously proposed. For instance, $\kappa(x)$ can be controlled by varying the transverse position of the RIM [69, 70] or by pulse energy regulation [65, 66]. These ideas were also implemented with the LbL method [67, 68], where apodization is achieved by adjusting the writing velocity, length, or transverse position of each line. Despite the progress, all these techniques induce a spatial variation in the average RIM which causes asymmetric non-linear chirp. Ideally, apodization should be performed by keeping the average RIM constant. This can be achieved by controlling the grating visibility instead of the exposure or RIM position.

Towards that end, the technique of apodization by phase modulation [71-73] is proposed and applied to our direct-writing scheme. By simply modulating the phase of the grating, this technique enables apodization with constant laser power and exposure, hence maintaining a constant average RIM and mitigating the challenge of handling highly non-linear induced RIM vs laser power [65, 67]. Apodization by phase modulation is achieved by incorporating an additional periodic function with a slowly varying amplitude to the grating phase. Any periodic function can be used [71], but in this article, a sinusoidal function is chosen. The refractive index modulation of the grating can be expressed as:

$$\Delta n(z) = \overline{\Delta n}(z)\left(1 + v(z)\cos\left(\frac{2\pi z}{\Lambda_g} + \phi_g(z) + A(z)\sin\left(\frac{2\pi z}{\Lambda_\phi}\right)\right)\right) \tag{4.1}$$

where z is the position along the fiber, Λ_g is the grating period, $\overline{\Delta n}$ is the average refractive index change over Λ_g, v is the visibility, ϕ_g is the grating phase and $A(z)\sin\left(2\pi z/\Lambda_\phi\right)$ is the additional phase modulation function of period Λ_ϕ and amplitude profile, $A(z)$. Traditionally, apodization is achieved by controlling $\overline{\Delta n}(z)$ or $v(z)$ to modify the grating envelope. In a phase modulation scheme, both are kept constant, and the profile of $A(z)$ determines the grating apodization. By expanding Eq. (4.1) in a Fourier series, the refractive index modulation becomes [73]:

$$\Delta n(z) = \overline{\Delta n}\left(1 + v\sum_{m=-\infty}^{\infty} J_m\left(A(z)\right)\cos\left(\frac{2\pi z}{\Lambda_g} + \phi_g(z) + m\frac{2\pi z}{\Lambda_\phi}\right)\right), \tag{4.2}$$

where J_m is the m^{th} Fourier component, defined by a Bessel function of the same order. The 0^{th} Fourier component ($m = 0$) is related to the main Bragg resonance, and the $\pm m^{th}$ are optical superlattice sidebands due to the periodic modulation. To ensure that these sidebands are outside of the optical operation band of the FBG, a sufficiently small period Λ_ϕ should be chosen [71]. Considering only the 0^{th} component of Eq. (4.2), $J_0\left(A(z)\right)$ acts as the envelope function of the grating, i.e. similar to the visibility. Hence, $A(z)$ is related to the normalized target apodization profile $|\boldsymbol{\kappa_n}(z)|$ by an inverse Bessel function:

$$A(z) = J_0^{-1}(|\boldsymbol{\kappa_n}(z)|). \tag{4.3}$$

Note that for the following demonstration, the grating profile is represented with a complex coupling coefficient $\boldsymbol{\kappa_n}(z)$, where the amplitude specifies the normalized apodization profile and where ϕ_g is incorporated as the phase.

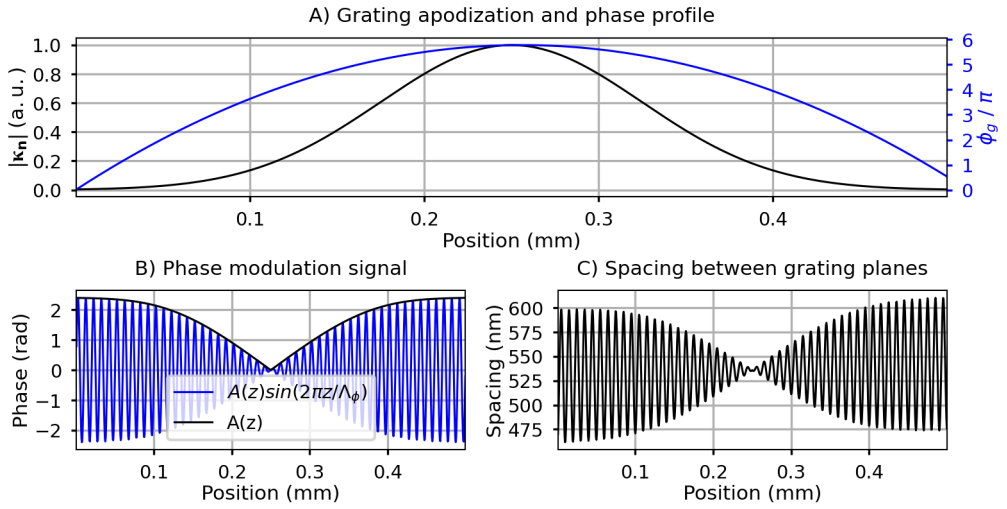

Figure 4.7: A) Example of a Gaussian apodization profile and quadratic phase profile that produces a linear chirp. B) To achieve apodization, a phase modulated signal, represented by the blue curve, is added to the total phase of the grating. The black curve represents the modulation amplitude. The sinusoidal function has a modulation period $\Lambda_\phi = 10$ µm. C) Corresponding prescribed distance between each laser-inscribed modification as calculated by Eq. (4.4).

To apply this phase modulation to our FS writing scheme, the total grating phase is mapped to the physical distance between every laser-induced modification by:

$$\Delta z_n = \Lambda_g \left(1 - \frac{\phi_{tot}(n\Lambda_g) - \phi_{tot}\left((n-1)\Lambda_g\right)}{2\pi} \right), \tag{4.4}$$

$$\phi_{tot}(z) = \frac{2\pi z}{\Lambda_g} + \phi_g(z) + J_0^{-1}(|\boldsymbol{\kappa_n}(z)|)\sin\left(\frac{2\pi z}{\Lambda_\phi}\right), \tag{4.5}$$

where Δz_n is the n^{th} spacing between the grating planes. A more visual interpretation of the process described above is presented in Figure 4.7. which shows an example for a Gaussian apodization and an exaggerated linear chirp of 75 nm/mm. The modulation period was fixed at $\Lambda_\phi = 10$ µm. The target apodization $|\boldsymbol{\kappa_n}(z)|$ and phase $\phi_g(z)$ profiles are presented in Figure 4.7-A. $|\boldsymbol{\kappa_n}(z)|$ is used to compute $A(z)$ using Eq. (4.3), and the modulation signal is shown in Figure 4.7-B. The distance between each grating planes is computed from Eq. (4.4) and (4.5), and is illustrated in Figure 4.7-C.

4.7.2 Arbitrary complex apodization profile

Combined with our high precision phase control strategy, the phase modulation apodization technique presented above allows the fabrication of arbitrary complex grating structures at very high spatial resolution, i.e. with very sharp phase and/or apodization change. To demonstrate our ability to write challenging apodized FBGs, we designed a structure that combines three non-uniform FBGs typically used as a benchmark to show apodization performance, but all in a single structure written in a single pass. This includes a square-top FBG (sinc apodization), a linearly chirped Gaussian apodized (LCGA) FBG and a π phase-shifted distributed feedback (DFB) FBG, each centered at different Bragg wavelengths. The LCGA FBG is centered at $\lambda_B = 1568.7$ nm and has a chirp rate of 1 nm/mm. The DFB and sinc apodized FBGs are shifted by ±20 nm, respectively. The maximum strength of the DFB was intentionally lowered to present a reflectivity spectrum with similar maximum reflectivity for the three sub-structures. Eq. (4.6) and (4.7) represent the total apodization profile of this design and Eq. (4.8) to (4.10) are the apodization and phase functions of each sub-structure.

$$\boldsymbol{\kappa_n}(z) = \exp(iK_0 z)\left\{\sum_{m=1}^{3} \left|\boldsymbol{\kappa_{n,m}}(z)\right| \exp\left(i\left(\Delta K_m z + \phi_{g,m}(z)\right)\right)\right\} \tag{4.6}$$

$$\Delta K_m = -\frac{4\pi n_{eff}}{\lambda_B^2}\Delta\lambda_m \tag{4.7}$$

$$S = \mathrm{sinc}\left(\frac{2\pi N_0}{L}(z - L/2)\right), \qquad \left|\boldsymbol{\kappa_{n,1}}(z)\right| = |S|, \qquad \phi_{g,1}(z) = \pi\left(\frac{\mathrm{sign}(S)+1}{2}\right) \tag{4.8}$$

$$\left|\boldsymbol{\kappa_{n,2}}(z)\right| = \exp\left(-\frac{1}{2}\left(\frac{z - L/2}{\sigma L/2}\right)^2\right), \qquad \phi_{g,2}(z) = \frac{c}{2}z^2 \tag{4.9}$$

$$\left|\boldsymbol{\kappa_{n,3}}(z)\right| = 0.12, \qquad \phi_{g,3}(x) = \begin{cases} 0\,; z < L/2 \\ \pi\,; z \geq L/2 \end{cases} \tag{4.10}$$

Where m is the sub-structure number, K_0 is the central wavevector given by $2\pi/\Lambda_g$, ΔK_m and $\Delta\lambda_m$ are the wavevector or wavelength offset, $\left|\boldsymbol{\kappa_{n,m}}(z)\right|$ is the normalized apodization profile amplitude, $\phi_{g,m}$ is the grating phase, and L is the length. In the case of the LCGA structure, $\sigma =$

0.3, $c = (K_{\Lambda_f} - K_{\Lambda_i})/L$. The parameter N_0 for the sinc apodized structure is $N_0 = 6$. The DFB has a π phase shift located in the middle of the grating.

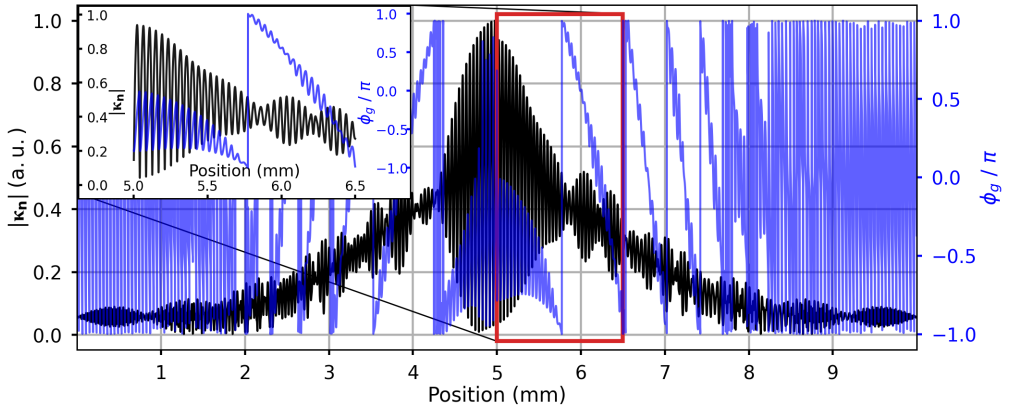

Figure 4.8: Design of the apodization and phase profile used to demonstrate the ability to write arbitrary complex grating. The smallest feature has a periodicity of 20 µm.

Figure 4.8 shows the resulting complex normalized coupling coefficient $\boldsymbol{\kappa_n}(z)$, calculated using Eq. (4.6). Designing the FBG with a large bandwidth yields a structure with some high frequency features, where the amplitude and phase profile oscillate with a period as small as 20 µm. The design proposed in Figure 4.8 was inscribed at first order in an uncoated SMF-28 fiber using the methods described above. The FBG had a length of 10 mm, was written at 50 µm/s and a burst of 175 pulses per grating plane was chosen. The laser pulse energy was 275 nJ which corresponded to a maximum κ of about 525 m^{-1}. To resolve the small features, the period of the sinusoidal phase function was set to $\Lambda_\phi = 2.5$ µm.

Figure 4.9 shows the reflection spectra of this FBG along with its numerical simulation. The simulation was performed using a simple thin-film method [21]. The typical features of the three FBG sub-structures, covering a bandwidth of 40 nm, are clearly distinguishable: The sinc function FBG shows a square response with 6 obvious oscillations (associated with $N_0 = 6$), the group delay of the LCGA FBG has a slope of -10.15 ps/nm, matching the designed chirp of 1 nm/mm, and the DFB resonant mode is well centered with the main Bragg resonance. The first side lobe levels of the sinc function and DFB gratings are respectively -16 dB and -12.5 dB, slightly higher than the predicted level. However, considering the complexity of the design and the good agreement between the numerical simulation and the fabricated FBG, this result proves

the ability of the phase modulation method to perform apodization with high precision and high spatial resolution using a FS direct-writing method. It also shows that our phase control strategy based on PSO tracking is well adapted to precisely control the position of individual grating planes, even when their relative distance is aggressively modulated. The writing's imperfections are due to residual sources of noise such as high-frequency noise induced by the stage, vibrations, slight deviation from the core center, and laser power fluctuations. The effects of these can be observed as noisy and high-level side-bands straying from expected simulated profile.

It should be noted that this method of apodization is well adapted to any direct-writing scheme (PbP, LbL or Pl-b-Pl) where it is possible to control the exact position of each laser induced modification.

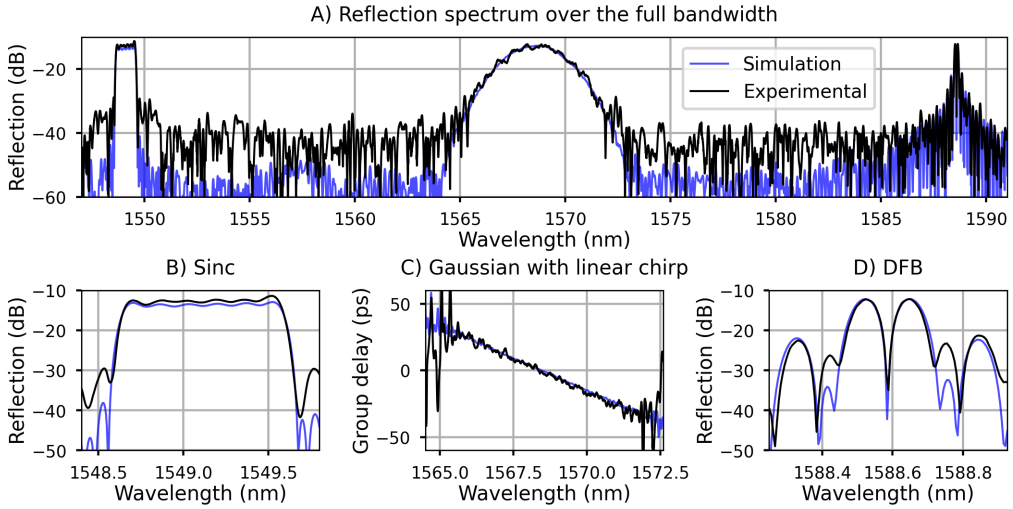

Figure 4.9: Simulated vs. experimental reflection spectra of the complex-apodized FBG written in a single pass using the function described in Figure 4.8. A) Broadband reflection spectrum. B) Zoom of the sinc function apodization response. C) Group delay of the linearly chirped and Gaussian apodized part. D) Zoom of the DFB response.

4.7.3 Complex ultra-long FBGs

To demonstrate the ability of our technique to maintain high quality over a longer distance, a phase-only filter, which requires a long FBG (>100 mm) to ensure a narrow spectral phase response, was designed [92] and successfully fabricated.

Figure 4.10-A shows the grating profile, which targets a square amplitude spectral response with a peak reflectivity of 50 % and a bandwidth of 50 GHz. It is designed to impart a rectangular π phase shift to the central frequency of the main stopband, with a bandwidth of just 2 GHz. The FBG was written in an uncoated SMF-28, with a length of 106 mm, a target κ of 362 m^{-1}, and a modulation period of $\Lambda_\phi = 10$ µm. Figure 4.10-B and C shows the simulated and measured spectral response (amplitude and phase) of this FBG. This result highlights the capacity of maintaining an excellent amplitude and phase control over a long distance, which is an essential requirement to achieve such narrow spectral phase response. The limitation toward even longer FBG may ultimately depends on the amplitude and phase error that can be tolerated.

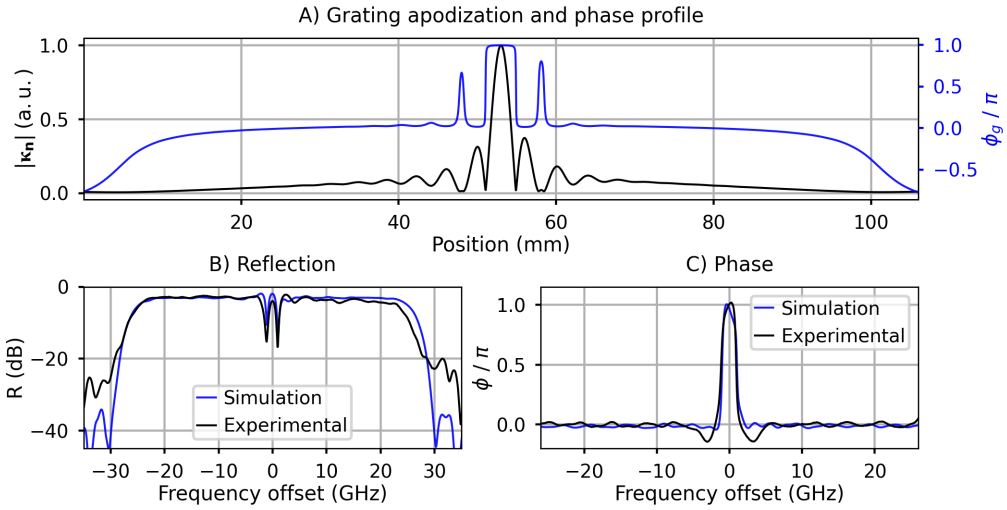

Figure 4.10: A) Design of the grating apodization and phase profile of a 106 mm long FBG. B) and C) Simulated vs. measured reflection and phase response of the filter.

4.8 Conclusion

This article proposed and demonstrated four different refinements that may be used together to enhance the capabilities for fabricating FBGs with direct-writing schemes based on FS lasers. Based on weak probe gratings measured by OFDR, a novel alignment procedure was implemented and successfully used to map the absolute core position of different types of fiber. This method is precise, flexible, and is non-destructive, i.e. a final strong and high-quality first order FBG can be written in the probed area. It can be seen as an alternative to the typical alignment method relying on an imaging system but requires the availability of an OFDR system.

For the writing scheme itself, a phase control strategy based on PSO tracking was used to precisely control the position of each of the grating planes. It was also demonstrated that a multi-pulse approach provides a way to inscribe strong first-order grating with low insertion loss and high spectral quality. These writing methods made it possible to implement an apodization method based on phase modulation, allowing both phase and amplitude control within a few grating periods. This method of FS direct-writing can be used to fabricate long FBGs, with arbitrarily complex apodization and phase profiles, offering the potential for tailoring complex spectral functionalities over a large bandwidth. Our work now focuses on challenging applications that could not have been contemplated without our novel approach and which will be reported on in the future.

Funding. Natural Sciences and Engineering Research Council (NSERC); Canadian Foundation for Innovation (CFI); Fonds de Recherche du Québec – Nature et Technologies (FRQNT).

Disclosures. The authors declare no conflicts of interest.

Data availability. Data underlying the results presented in this paper are not publicly available at this time but may be obtained from the authors upon reasonable request.

Supplemental document. See Supplement 1 for supporting content.

CHAPTER 5 FABRICATION OF NOVEL FBG-BASED SENSORS AND FILTERS

In the last two chapters, a method to inscribe high-quality FBGs using a FS direct-writing scheme was established. It was shown that complex apodization and phase profiles could be inscribed with high precision and accuracy by using a phase modulation approach and a PSO phase control strategy. The fabrication of a challenging ultra-long FBG was also demonstrated successfully. Moreover, our alignment method has proven to be quite effective at tracking the fiber core position accurately, in both coated and uncoated fibers. From that point, different types of FBG that could serve as real-life applications were realized.

In this context, this chapter presents the additional research results for two practical applications that were successfully implemented. First, the fabrication of a distributed random FBG strain sensor and its potential use for a real-time 3D shape sensing is examined. Then, advanced phase filters for the realization of high-speed passive optical logic processing and for group-velocity dispersion compensation of telecom data signal are demonstrated.

Please note that my involvement in these projects was limited to the fabrication and characterisation of the FBGs. The other development phases, such as the design, assembly, and testing of the devices, were done by other colleagues. Hence, even though a proper motivation and introduction to each project are given, the in-depth technical details on the working principles or experimental results of these applications are left as references to the interested reader, as they are beyond the scope of this thesis. The goal here is to show different examples of applications that were achieved with the FBG writing system presented in this thesis. These examples are used to show the full potential of this writing system as well as the performance of the fabricated FBGs in real-life conditions.

5.1 Fiber optic shape sensing

5.1.1 Introduction

The technology of fiber optic 3D shape sensors (FOSS) can be used to track the shape and position of dynamic objects remotely and in real-time [93]. It has been used for many applications in the fields of civil, mechanical, aerospace, and biomedical engineering [93]. FOSS

are commonly based on either of the two following strain sensing technologies: FBG arrays [94] or OFDR distributed sensing [95, 96]. While FBG-based sensors provide large sensing length, high strain accuracy and high sampling rate, they are limited to just a few discrete measurement points of spectrally unique FBGs inscribed at different position in the fiber. The low spatial resolution offered by those sensors is generally not sufficient to reconstruct the shape of bodies with complex geometry, tight bend, twist, or high strain gradient. This is often the case in biomedical applications or instruments such as endoscope, catheter, or needle, where OFDR is the preferred approach to obtain high-resolution fully distributed strain measurements along the length of the sensor [93, 95, 97, 98]. Put simply, OFDR distributed measurement systems are based on the detection of the optical backscatter of the fiber, such as the Rayleigh, Brillouin, or Raman scattering [95, 96].

Recently, our research group demonstrated different ways to increase the light scattering of optical fibers, either by exposing the fiber core to UV radiation [97] or by inscribing random gratings [98, 99], allowing to improve the signal to noise ratio of OFDR-based strain measurements. Additionally, it was shown that these fibers can be extruded as an optical fiber triplet to serve as a functional FOSS for minimally invasive surgery [100], as illustrated in Figure 5.1. However, a technical challenge remained. Because the coating of the fiber must be removed to expose its core to UV light, the mechanical strength of the fiber is reduced, and they become difficult to extrude without breaking. A solution to this problem was to inscribe random FBGs with a FS laser directly through the coating of the fiber to preserve its mechanical strength. Thus, this section describes the fabrication of such FBG sensors, which were then extruded into a working prototype of a FOSS.

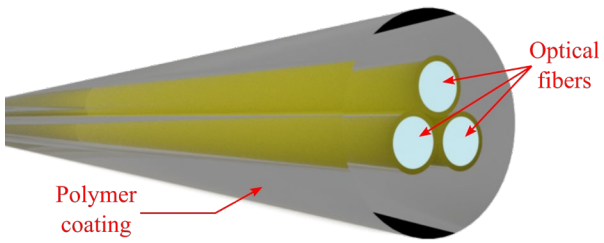

Figure 5.1: Schematic illustration of an optical fiber triplet that can serve as a FOSS. Image reproduced with the permission of P. Lorre.

5.1.2 Through-the-coating inscription of random FBGs by femtosecond laser

Random FBGs are based on a random fluctuation of the grating period or phase. This type of grating are designed to exhibit a weak reflectivity over a large bandwidth, which provides them with an enhanced Rayleigh backscattering level of several orders of magnitude higher than the backscattering of an unexposed SMF-28 fiber [99]. The distance between each grating planes is calculated from:

$$d_n = \Lambda_g(1 + \mathrm{A}) \tag{5.1}$$

$$\Lambda_g = \frac{m\lambda_B}{2n_{eff}} \tag{5.2}$$

Where d_n is the distance between the n^{th} and $(n+1)^{th}$ grating plane, Λ_g is the grating period, λ_B is the desired Bragg wavelength, m is the grating order, n_{eff} is the effective refractive index of the fiber and $\mathrm{A} \sim \mathrm{U}(-\alpha, \alpha)$ is a random uniform distribution whose outcome is bounded by a parameter α that is defined as the randomness percentage of the grating.

In order to achieve distributed sensing, several random FBGs were inscribed directly through the coating of a polyimide coated fiber using the FS Pl-b-Pl direct-writing scheme described in this thesis. They were made over a length of 0.5 to 1.5 m. The physical properties of this fiber are listed in Appendix C. Using the PSO phase control strategy described in Section 3.3, it is relatively easy to induce a random fluctuation of grating phase, since the position of each plane (calculated from Eq. (5.1)) can be directly fed into motor controller of the writing system, which then triggers the laser to emit a burst of pulse at each desired position.

5.1.3 Results

First, a study of the randomness (α) of the FBGs and its effect on the bandwidth was undertaken to evaluate the control and precision of the writing system compared to a numerical simulation. It was performed by writing several 50 mm long FBGs through the coating of a polyimide coated fiber with α varying from 1% to 6%. The reflection spectrum of the random FBGs for different randomness is shown in Figure 5.2 (a), from which the bandwidth can be calculated by using a Lorentzian fit. The experimental results agree well with the simulated bandwidth of random

FBGs as shown in Figure 5.2 (b), demonstrating excellent control during the fabrication process. A randomness of 4 % was found to be adequate for the sensing application giving a bandwidth of approximately 9 nm.

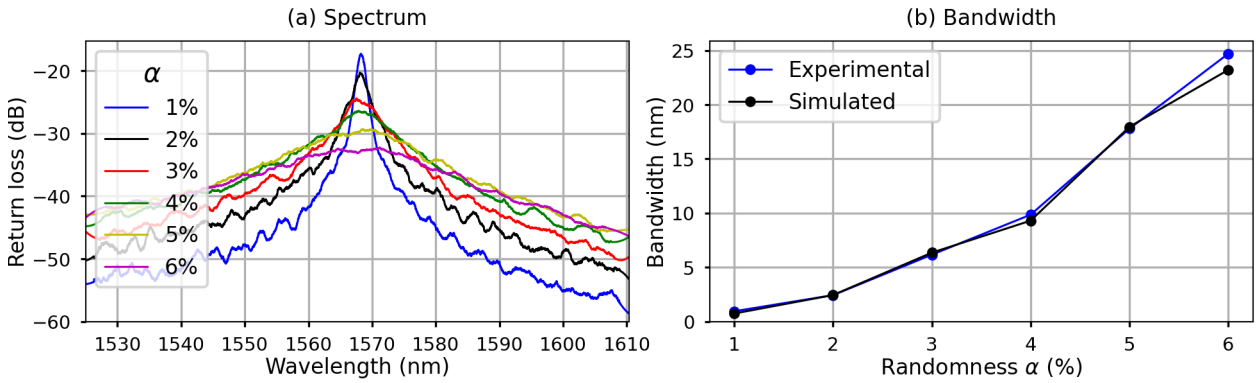

Figure 5.2: (a) Reflection spectrum of random FBGs showing the evolution of the bandwidth as a function of the randomness (α). (b) Experimental vs. simulated sensor bandwidth as a function of the randomness.

Another important characteristic of these types of distributed sensors is the spatial distribution of the scattering along its length, which can be assessed from the time domain signal of the OFDR instrument, instead of the frequency spectrum. Ideally, the backscattering signal should be constant throughout the whole FBG to obtain a uniform response and sensitivity from every point in the sensor. To evaluate the scattering uniformity of the sensors, long FBGs of about 950 mm were written in both a polyimide coated fiber and an uncoated SMF-28 fiber for reference. As shown in Figure 5.3, the backscattering amplitude of both FBGs suffers from spatial fluctuations. In the case of an uncoated fiber, the signal is quite uniform, but severe fluctuations with an amplitude up to ~10-15 dB can be seen for the FBG made through the polyimide coating. This can be problematic when the amplitude of the fluctuation is larger than the dynamic range of the sensing instrument, causing dead zones in the sensing area.

This issue was attributed to the polyimide coating being highly inhomogeneous in terms of thickness and shape along the fiber, distorting the focal spot. By optimizing and increasing the resolution of the alignment procedure to compensate for the coating inhomogeneity, it was possible to drastically improves the uniformity of the backscatter signal. For example, Figure 5.4 (a) shows the backscatter amplitude for a 500 mm random FBG written through the polyimide

coating, after the alignment procedure was improved. Unfortunately, another big challenge was the reproducibility of such low spatial fluctuation during the fabrication process. The uniformity was also difficult to maintain over longer length. The example shown in Figure 5.4 shows one of the best performance possible with a polyimide coated fiber, as the coating of this specific fiber was probably very uniform. However, even if it is currently not possible to prevent the focal spot from being unevenly distorted by some shape variation of the fiber coating, these sensors can still be used for shape sensing, as long as the amplitude of the fluctuation remains within the dynamic range of the sensing instrument.

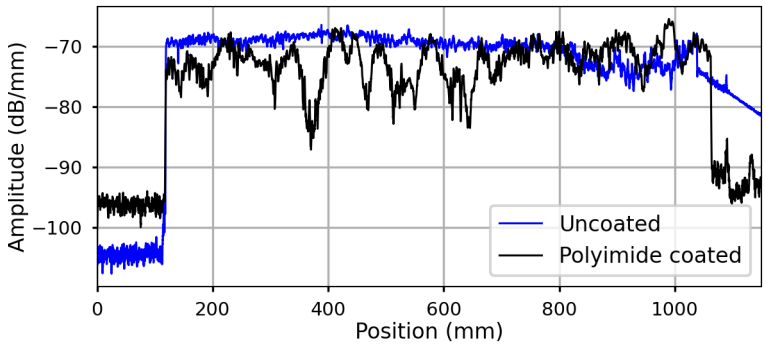

Figure 5.3: Backscatter amplitude for FBGs written in an uncoated SMF-28 fiber and a polyimide coated fiber.

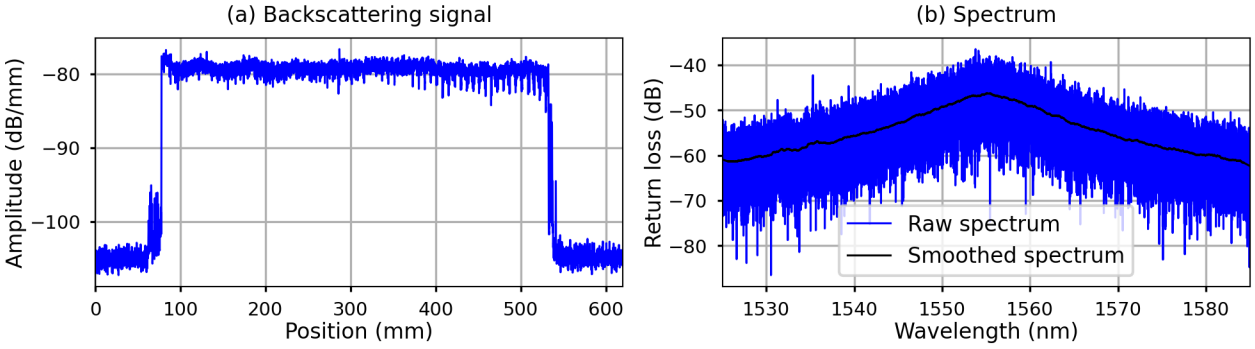

Figure 5.4: (a) Backscatter amplitude of an improved 500 mm long FS random FBG. Note the improvement in the uniformity of the signal with length compared to Figure 5.3. (b) Spectrum of the sensor.

Following the results presented above, random FBGs of 1.5 m in length were fabricated. Figure 5.5 shows an example of the backscatter signal for two of those sensors. It can be seen from Figure 5.5 (a) that a uniform backscatter amplitude can be obtained over a long length, but

managing the fluctuations is still a challenge, as shown in Figure 5.5 (b). To fabricate the FOSS, these FBGs were extruded into fiber triplets using the extrusion procedure developed by P. Lorre [100]. An example of the final result is given in Figure 5.6 (a), which shows a microscope image of a fiber triplet cross-section, while Figure 5.6 (b) and (c) show an example of shape reconstruction. However, because the research objective of this thesis was focussed on the fabrication of the sensors, further details about the shape reconstruction algorithm and the sensor performance can be found J. Francoeur's article [101].

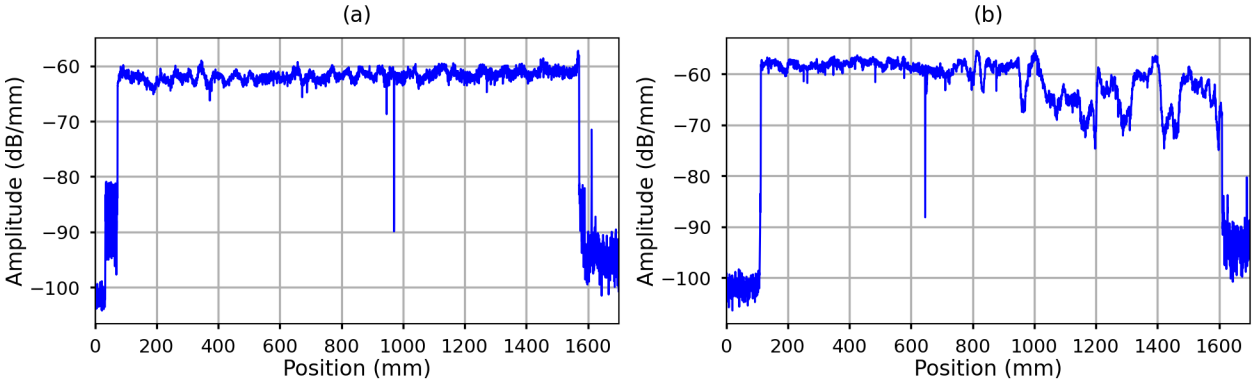

Figure 5.5: Backscatter amplitude of two random FBGs. (a) shows a very uniform response, while (b) shows some residual amplitude fluctuations.

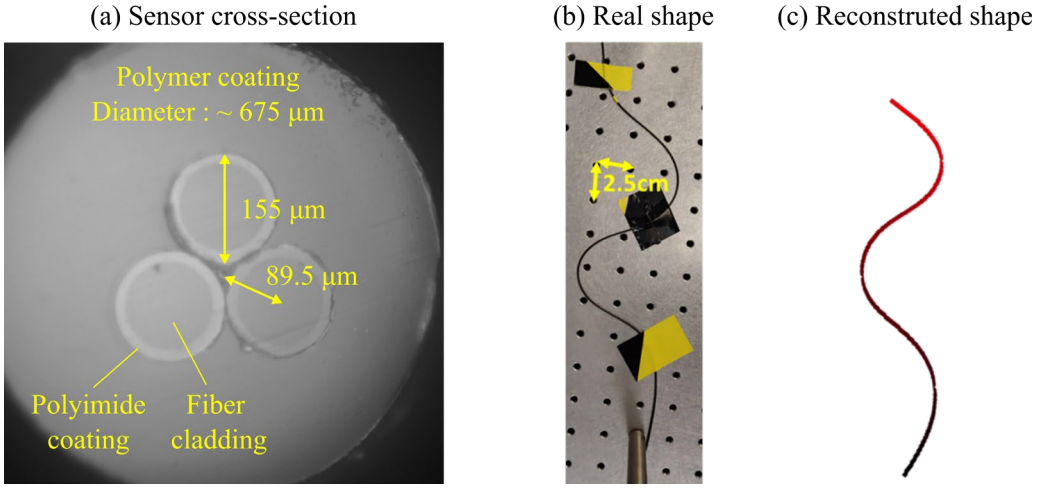

Figure 5.6: (a) Cross-section of a fiber triplet as seen from a microscope. (b) Example of a shape that the sensor was placed into. (c) Reconstructed shape. Reproduced with the permission of P. Lorre and J. Francoeur (Polytechnique Montreal).

5.2 Phase-only filters

This section presents the results of an ambitious project that was realized in collaboration with the research group led by José Azaña at the Institut national de la recherche scientifique (INRS).

5.2.1 Introduction

Optical linear spectral phase-only (or all-pass) filtering can be used to manipulate the phase of a complex waveform, while keeping its amplitude untouched [102]. Said to be passive, phase-only filters allow for an energy efficient filtering system, featuring high transmission and low-loss. They have been used in many fields of applications such as pulse shaping and arbitrary waveform generation [103-107], optical signal processing [72, 108-113], dispersion compensation [114, 115], spectroscopy [116], and coherent control of quantum states [117, 118], to name just a few. Being linear filtering devices, FBGs have been studied to implement all sorts of passive linear optical filtering functionalities [108]. Compared to other solutions based on bulky free-space optical components [104] or time-domain filtering [106], FBGs have the advantage of low cost, low weight, low losses, small size and are compatible with fiber-optics systems. However, tailoring specific spectral response by customizing the apodization and phase profile of FBGs have often been constrained by practical fabrication limitations such as insufficient apodization resolution and dynamic range, or the ability to control the phase of the grating over a long length.

In this context, this section presents the realization of two novel FBG-based phase-only filters employed for optical signal processing, which could be fabricated using the advanced capabilities of the FS direct-writing scheme presented in this thesis. The first is a discrete phase filter used for group-velocity dispersion (GVD) compensation of data signals passing through 70.56 km of a telecommunication link. The second filter has been realized to demonstrate the potential of passive ultrafast optical logic gates. It features a record spectral phase resolution of just 1 GHz, which was used to experimentally realize high-speed fully-passive NOT and XNOR logic gates.

5.2.2 Group-velocity dispersion compensation of 70.56 km fiber-optic link

Signal distortion induced by GVD in optical links can be compensated by different methods including digital signal processing, dispersion compensation fibers or linearly chirped gratings

[115]. Recently, S. Kaushal *et al.* proposed a discrete phase-only filter design to achieve GVD compensation of telecommunication data signals in fiber-optics links, while providing a significant reduction of the device length compared to linearly chirped grating [114]. By fabricating a waveguide Bragg grating (WBG) in a silicon-on-insulator platform, they experimentally demonstrated GVD compensation of a 24 Gbps non-return-to-zero on-off keying (NRZ-OOK) signal propagating through a 31.12 km fiber link, with a device length reduction of 5x compared to an equivalent linearly chirped WBG [115]. Of course, this reduction in length is highly desirable to reduce the amount insertion loss, but also because the fabrication of long linearly chirped grating is technically difficult to realize due to fabrication limitations and phase error accumulation (true for both waveguide and fiber Bragg grating).

Fortunately, this type of filter can be also implemented in an FBG, and the main objective of this research project was to evaluate the possibility of fabricating one using the FS direct-writing method presented in this thesis. Using a 6.9 cm FBG, GVD compensation of a 24 Gbps NRZ-OOK signal over 70.56 km of fiber-optic link was experimentally demonstrated, with a device length 2.2x smaller than an equivalent linearly chirped FBG. For more information on the design and working principle of this filter, refer to [114].

Figure 5.7 (a) shows the target apodization and phase profile of the 6.9 cm long grating, calculated from the target spectral response of the grating (described in [114]) using an inverse layer peeling algorithm. As can be seen, this complex design requires to control the coupling coefficient and phase accurately, over a large dynamic range and with a very high spatial resolution, something that has been difficult to achieve using other conventional inscription methods. To achieve a maximum κ of 300 m^{-1} with low insertion loss, the FBG was written using 200 pulses/plane, a speed of 30 $\mu\mathrm{m/s}$ and a sinusoidal phase modulation with a period (Λ_{ϕ}) of 10 μm. This filter's design targets a reflectivity of 50 %, with a -3 dB bandwidth of 100 GHz, centered around a Bragg wavelength of 1550 nm. Figure 5.7 (b) compares the experimental spectral response (in reflection) to its simulation. The remarkable agreement between simulation and experiment clearly demonstrates the ability to inscribe high-quality complex FBG providing the required spectral phase response to achieve GVD compensation. Figure 5.8 (a) shows the experimental setup that was used to evaluate the performance of this filter. A 24 Gbps pseudo random bit sequence is generated with an arbitrary waveform generator and an intensity

modulator. The signal is dispersed through 70.56 km of SMF-28 fiber before being amplified and filtered by the FBG. Figure 5.8 (b), (c) and (d) shows the eye diagram of the signal before the fiber, after the fiber and after the filter. Comparing (b) and (c), the obvious eye opening reveals the ability for GVD compensation using this compact phase-only filter and proves the performance of the FS direct-writing method. The full results of this project have been accepted to the 2022 IEEE photonics conference [119] and a complete manuscript should be written in a near future.

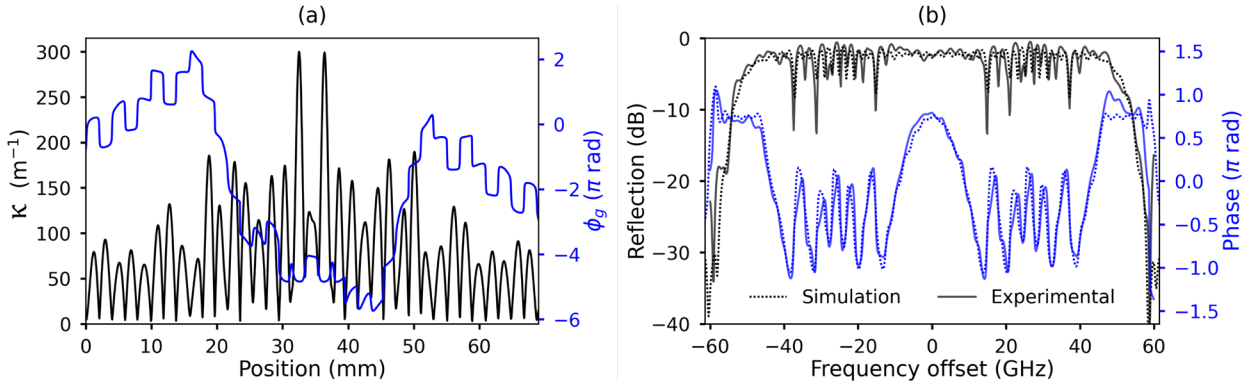

Figure 5.7: (a) Target coupling coefficient and grating phase, as calculated from an inverse layer peeling algorithm. (b) Simulated vs. measured reflectivity and phase spectral response.

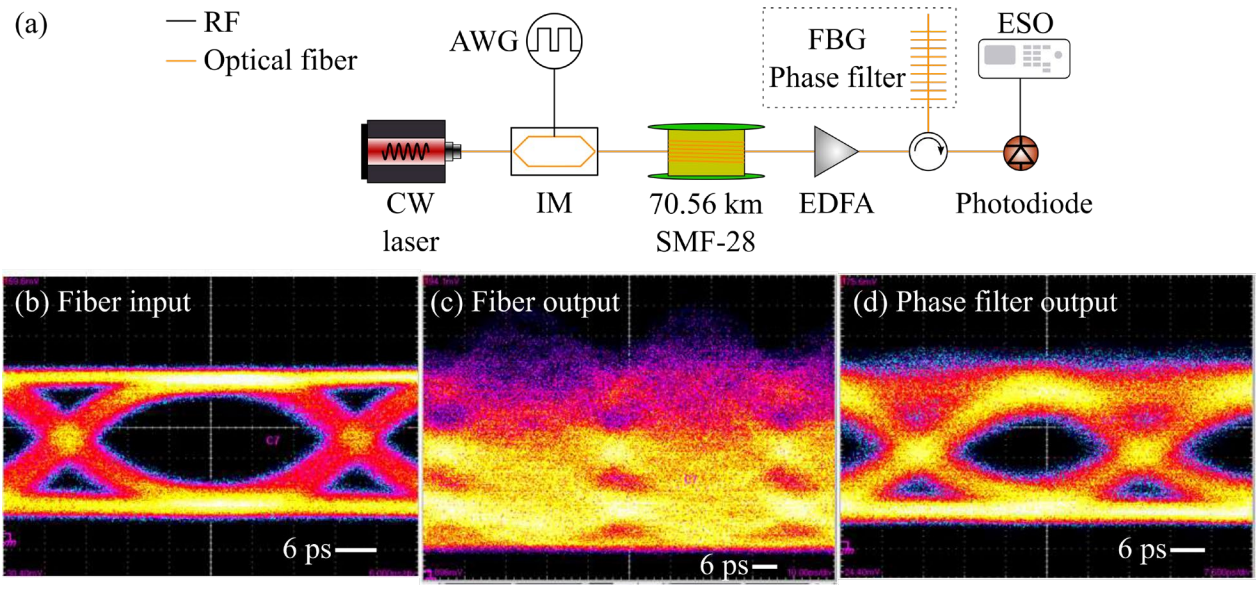

Figure 5.8: (a) Representation of the experimental setup to measure the dispersion compensation. A 24 Gbps pseudo-random bit sequence NRZ-OOK signal is generated from an arbitrary

waveform generator (AWG) and intensity modulator (IM). After dispersing through the fiber spool of 70.56 km, the signal is amplified by an erbium-doped fiber amplifier (EDFA) and is reflected from the FBG phase filter with a circulator. It is detected by a 50 GHz photodetector and electrical sampling oscilloscope (ESO). (b, c, d) Eye diagram measured at the input and output of the fiber, and after reflection from the FBG filter. (b, c, d) Reproduced with the permission of S. Kaushal (INRS).

5.2.3 Ultrafast passive optical logic processing based on phase-only filter

Since logic gates based on electronic transistors are reaching their fundamental physical limitations, progressing towards devices with higher processing speed and lower energy consumption has become difficult with today's technologies. Alternative solutions based on photonic devices have been explored for some time, but most of the proposed methods have yet to show better, or even similar performance, compared to electronic logic gates [110]. This is because most photonic gates are based on nonlinearity or interferometric methods to achieve computing tasks, making them slow and/or energy inefficient, which limits their practical range of applications. Recently, an implementation of the NOT operation was proposed and realized using passive spectral phase-only filtering, and inversion of a high-speed (640 Gbps) return-to-zero on-off-keying (RZ-OOK) data signal was demonstrated [110]. The working principle of this type of passive logic gate is explained in [110], but the basic idea is that the energy contained in the signal can be redistributed between the "0" and "1" bits by selectively inducing a π phase shift to the frequency clock components of the data signal (the carrier frequency and the different harmonics spaced by the modulation frequency). Hence, by manipulating the phase of the incoming signal instead of its amplitude, the energy is preserved during the bit inversion process (except for insertion loss). Naturally, FBGs can be used to target specific phase responses, and the first FBG implementation of such a passive gate was demonstrated in 1997 for the generation of a dark soliton pulse train [120, 121]. However, in most applications, phase filtering is achieved by using commercial waveshapers based on free-space diffraction, which are bulky device that can be limited in terms of frequency resolution (~12 GHz) [110]. This constraint on frequency resolution has severely limited the minimal speed at which this passive NOT operation could be

achieved, and 640 Gbps is nowhere near the standard bit rate used in a single channel of most telecom devices (~10-40 Gbps).

Hence, the goal of this project was to extend the ideas introduced in [110] towards an all-fiber based solution. By implementing a fully passive and linear NOT gate using a unique FBG design, it was possible to experimentally demonstrate the inversion of a 45 Gbps NRZ-OOK data signal with 127 random bit sequence (RBS). Moreover, the FBG involved in this work features an extremely small spectral phase resolution of just 1.2 GHz, which represents a 10x improvement compared to commercial waveshapers. This improved resolution was the key to achieving an efficient NOT operation at bit rates in the range of 10-40 Gbps.

The working principle of the NOT gate for an NRZ-OOK signal is illustrated in Figure 5.9, where the output signal of the phase filter (c) is the inverse of the input (b). This can be achieved by imparting a π phase shift only to the carrier frequency of the signal. Figure 5.9 (a) shows the target spectral response of the filter, superimposed to a representation of the power spectrum density (PSD) of the data signal. The sidebands of this signal correspond to the spectral components of the data bits and should not be phase shifted for optimal operation. A lower bit rate implies that the sidebands get closer to the carrier frequency, which is why a very narrow phase shift is required for inversion at 45 Gbps. More specifically, the filter targets a spectral response centered at a Bragg wavelength of 1550 nm, with a flat-top super-Gaussian amplitude profile, a peak reflectivity of 50% and a -3 dB bandwidth of 50 GHz. The target spectral phase response is a rectangular $0 - \pi$ phase shift with a -3 dB bandwidth of 1 GHz.

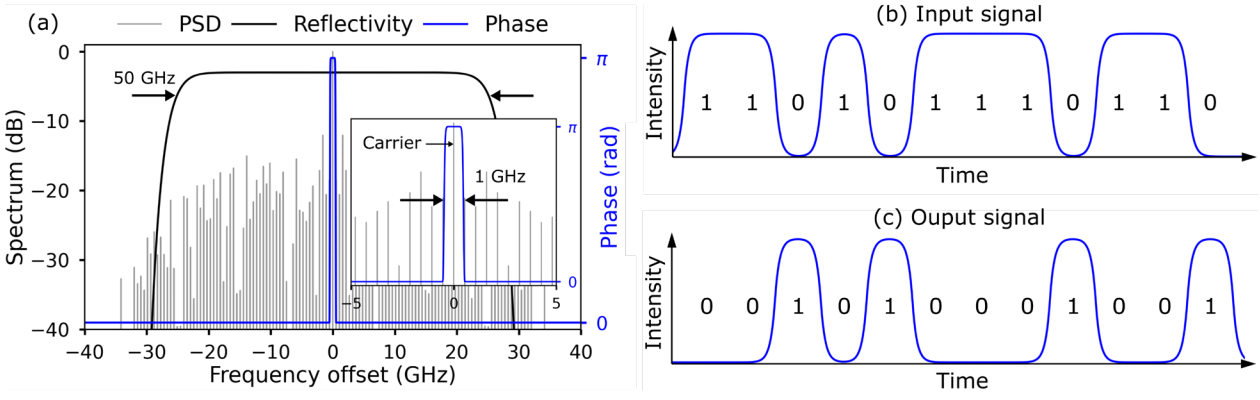

Figure 5.9: (a) Target spectral response of the phase-only filter used for NOT operation. The reflectivity covers a large bandwidth of 50 GHz, which contains most of the spectral components

of the NRZ-OOK data signal. The PSD of such signal is represented in gray. The inset shows that a π phase shift should be applied only to the carrier frequency, which can be done with a narrow bandwidth of 1 GHz. (b) Illustration of the input data signal. (c) Output signal after reflection on the FBG filter.

However, targeting such a narrow π phase shift is very difficult because it requires an FBG length of ~20 cm, and an accurate control of the apodization and phase profile. For instance, Figure 5.10 (a) shows the required apodization and phase profile calculated from the target spectral response shown in Figure 5.9 (a) using an inverse layer peeling algorithm. Specifically, this FBG design has a length of 213.6 mm, and the coupling coefficient requires to be controlled over a large dynamic range ($0.08 < \kappa < 378\ \mathrm{m}^{-1}$), with sharp transitions that demand an ultra-high spatial resolution. Despite this stringent requirement, it was possible to inscribe this challenging structure successfully in an uncoated SMF-28 by using the high spatial resolution of FS direct-writing scheme, the high dynamic range provided by phase modulation apodization, the high coupling coefficient offered by the multi-pulse approach, and the accurate tracking of the fiber core position. The inscription parameters were 150 pulses/plane, a writing speed of 30 µm/s, and a sinusoidal phase modulation with a period of 12.5 µm. Figure 5.10 (b) compares the experimental spectral response of the fabricated FBG to its simulation, which was computed from the target apodization profile. As can be seen, a precise π phase shift with a -3 dB bandwidth of 1.2 GHz could be achieved, and the agreement between the simulation and experimental result demonstrates excellent fabrication capabilities in the case of an ultra-long complex FBG.

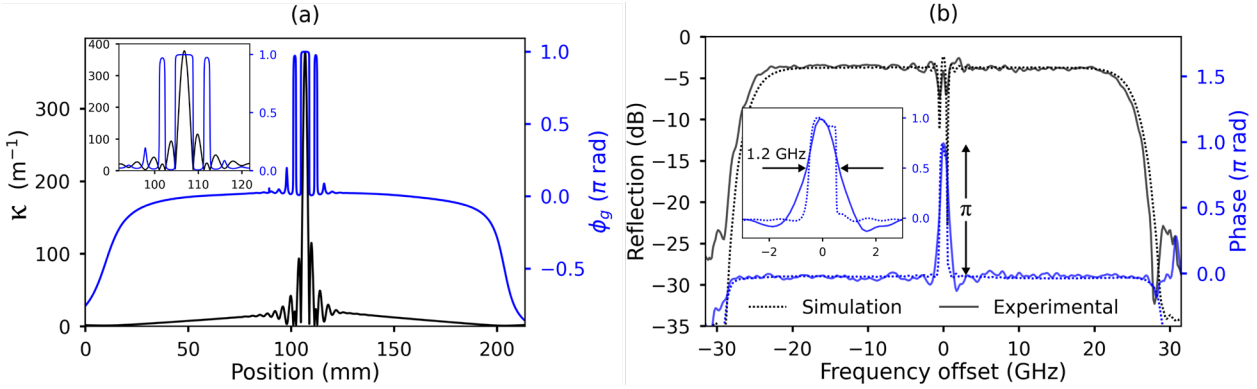

Figure 5.10: (a) Target coupling coefficient and phase profile. (b) Simulated vs. measured reflectivity and phase spectral response.

Nevertheless, note that FBGs of this length are prone to phase error accumulation during the writing process and are also extremely sensitive to environmental perturbations during their manipulation in the real-world. For this length of FBG, any local temperature or strain variation can significantly distort the spectral phase response of the filter. Therefore, instead of fighting against environmental perturbations and the unpredictable imperfections occurring naturally during the fabrication process, a prototype of a temperature controller based on a resistive heating array was designed and built at Polytechnique Montreal to compensate for phase errors. Figure 5.11 (a) shows a rendered image of this controller, where a series of 19 small resistors is placed under a 3D printed support that includes a V-groove to hold the fiber. To adjust the local phase of the grating, the power dissipated by each resistor can be controlled individually using a microcontroller. Of course, this prototype has many limitations, but it was found to be adequate to maintain the desired spectral phase response of the filter in real-world conditions. For example, Figure 5.11 (b) shows the phase response of the FBG with and without heating.

Finally, the performance of the passive NOT gate was evaluated at INRS using a similar setup as the one shown in Figure 5.8 (a), except for the 70.56 km of dispersive fiber. Figure 5.12 shows the input/output, as well as the eye diagram for the 45 Gbps 127 RBS data signal. Clearly, the inversion process is demonstrated, and an estimated energy consumption of just 34 fJ/bit is reported. Further details about the full result and performance of this filter can be found in the paper presented by S. Kaushal at the Signal Processing in Photonic Communications conference [122], and a full manuscript has been submitted for publication in a near future [123]. This manuscript includes an experimental demonstration of a passive XNOR gate, which could be realized using the same phase filter, but was not covered in the present section.

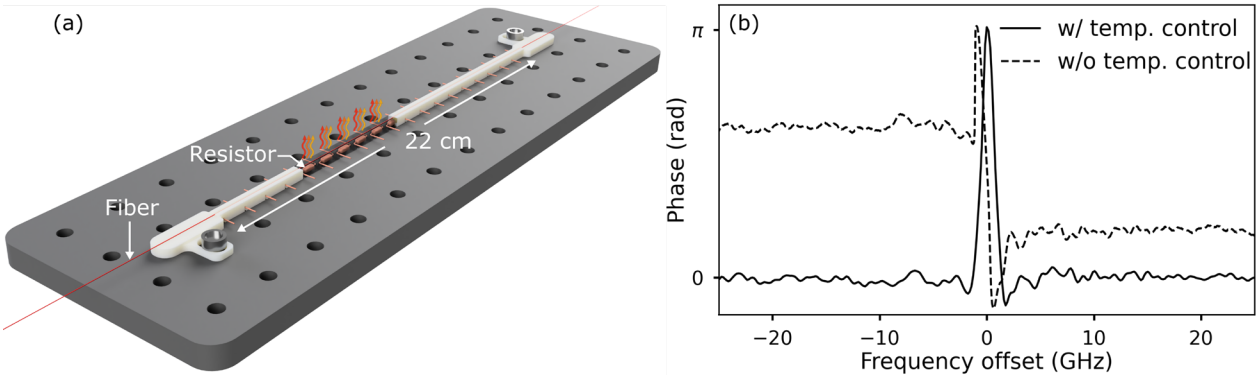

Figure 5.11: (a) Illustration of the temperature controller based on an array of resistive element incorporated in a 3D printed with a V-groove. (b) Spectral phase response of the phase filter with and without temperature control. Note that this controller was designed and built by the author of this thesis.

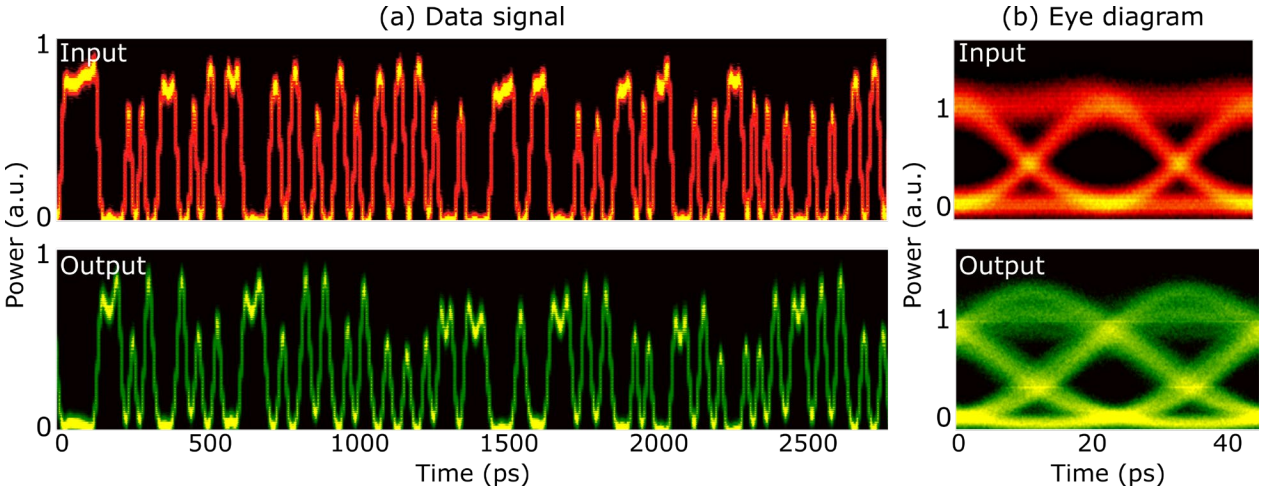

Figure 5.12: (a) 45 Gbps NRZ-OOK data signal with an RBS of 127 bits measured at the input and output of the phase filter. (b) Eye diagram corresponding to a single bit period. Reproduced with the permission of S. Kaushal (INRS) [123].

CHAPTER 6 GENERAL DISCUSSION AND RECOMMANDATIONS

The primary purpose of the research presented in this thesis was to develop and implement a FS direct-writing system for the fabrication of advanced FBGs. To get there, the limitations of existing direct-writing methods were studied and addressed by proposing new solutions. Overall, a complete system for the direct-writing of FBGs with FS laser was successfully established. This is demonstrated in the article published by Optics Express, where different methods used to inscribe high-quality FBGs with arbitrary complex apodization or phase profile are described. The results of this study indicate that the combination of a Pl-b-Pl scheme and a multi-pulse approach can produces FBGs with strong RIMs, low IL, and low PD. The study also demonstrates that the concept of apodization by phase modulation can be practically implemented in direct-writing systems by using PSO tracking, allowing the inscription of arbitrary complex structures. Moreover, it is shown that the alignment technique based on OFDR and weak probe gratings can track the fiber core position with high accuracy, and without the use of a camera system. Together, these key findings were used to realize advanced FBG-based sensors and filters, opening the doors to many new applications.

To put things into perspective, the rest of this chapter discusses about different features of the writing system and the meaning and significance of the findings. Recommendations for further improvement are also given.

6.1 Refractive index modifications: Beam shaping and multi-pulse exposure

As it was exposed throughout this thesis, the characteristics of the RIMs induced by tightly focussed FS pulses greatly impact the physical properties of the resulting FBGs (κ, IL, PD, …). In this work, a Pl-b-Pl approach based on astigmatic focussing was used to maximize the overlap between the RIM and the mode field of the fiber, which, according to the literature [40], should help to achieve strong coupling, low IL, and low PD, while minimizing the effect of astigmatism caused by the fiber curvature. Furthermore, the effects of a multi-pulse exposure were studied to understand how it impacts the grating properties.

With this approach, it was found that FBGs with high spectral quality and IL < 0.1 dB/cm can be inscribed in both an uncoated SMF-28 fiber or a polyimide coated fiber, without the use of index-matching oil compensation techniques. The study about multi-pulse exposure have shown that a burst of many lower-energy pulses allows for stronger coupling and lower IL than with a single-pulse, and a pulse energy threshold delimiting the formation of type-I vs. type-II FBGs was established. Even though multi-pulse exposure has been extensively studied in the field of FS laser processing and WBG writing [5, 36-38], there is only a few reports in the literature about the use of this type of exposure for the fabrication of FBGs. Hence, this study contributed to a clearer understanding of the physical mechanisms involved in the formation of FBGs with multiple pulses. However, type-II FBGs were not studied in detail during this research, and a further characterization is needed to understand the properties of FBGs made in this regime, with this setup.

In the low-loss (type-I) regime, κ value of up to 600 m^{-1} and 325 m^{-1} were demonstrated for an uncoated fiber and polyimide coated fiber, respectively. In previous studies [54, 60, 124], the ratio of the coupling coefficient to the scattering loss coefficient (κ/α) was identified as a good figure of merit to determine the maximum reflectivity of a grating. α (m^{-1}) is defined by:

$$\alpha = \frac{\ln(T_{IL})}{-2L}, \tag{6.1}$$

where $T_{IL} = 10^{-\mathrm{IL(db)}/10}$ is the out-of-band transmission loss (in linear scale) and L is the length of the FBG. A higher ratio of κ/α indicates a stronger grating, with higher reflectivity and lower IL. For $\kappa = 600\ \mathrm{m}^{-1}$ and using a conservative value for IL of 0.1 dB/cm, this ratio can be evaluated to $\kappa/\alpha = 521$. This result compares well with other similar writing schemes. For instance, a maximum value of $\kappa/\alpha = 70$ was reported for a standard PbP method [124], $\kappa/\alpha = 172$ was reported for Pl-b-Pl method using a slit beam shaping [54], and $\kappa/\alpha = 720$ was reported for a LbL method [60]. Gratings made with the same beam shaping technique [40] than in this thesis have $\kappa/\alpha = 1500$. However, in this case, very low IL < 0.02 dB/cm were reported, but they do not discuss the uncertainty of the IL measurement, which is usually in the same order of magnitude. As it was shown in Figure 4.6 of the manuscript, IL in the order of ~ 0.02 dB/cm

could also be measured, but since the measurement of very low IL is sensitive many sources of errors, it seems better to report IL bounded by the value of < 0.1 dB/cm.

The FBGs made during this work were also found to have low PD, as illustrated in Figure 4.5, where the birefringence (Δn_B) is measured at 6.2×10^{-6} RIU. This value is at least one order of magnitude better than most PbP schemes [45] and is in good agreement with the best performance shown in [54], where a slit beam shaping method is used.

Overall, these findings illustrate that a Pl-b-Pl method with a multi-pulse exposure is well suited for applications that requires high coupling, low IL, and low PD. However, further improvements could still be made to reach an even higher κ/α ratio and lower PD. For example, a different focusing arrangement could by used to optimize the RIM's cross-section. Instead of using a single cylindrical lens to realize astigmatic focussing, a cylindrical lens telescope with additional degrees of freedom could be installed before the focussing objective [45, 47]. This could greatly improve the ability to control the shape of the focal spot and to fine tune the astigmatism. To better characterize and understand the shape of the RIMs, a microscope system should also be implemented. For example, imaging techniques based on differential interference contrast (DIC) microscopy are commonly used to see the structure of a grating or to study FS modifications [5].

In the case of a polyimide coated fiber, the repetition rate of the laser was set to just 60.606 kHz to avoid degradation of the coating by thermal accumulation, making it impractical to inscribe FBGs with more than 50 pulses/plane, as the process become slow. Increasing the NA of the focussing lens could help to reduce the power density at the coating and the coating degradation. If fabrication time is not a constraint, it might be also possible to further increase the maximum κ value for through-the-coating writing by using a higher number of pulses.

Finally, since FS laser processing is based on nonlinear absorption, small variations of the laser power can cause significant variations in the coupling coefficient, reducing the spectral quality of the FBG. Thus, finding a way to reduce those power fluctuations could help to improve the uniformity of the writing process.

6.2 Direct-writing apodization and phase control

Apodization by phase modulation has proven to be a valuable tool for the fabrication of arbitrary complex FBGs with advanced spectral functionalities. During this thesis, many apodized gratings were successfully fabricated, with their spectral responses closely matching the simulations. To test the full capabilities and limitations of this technique, a challenging design was proposed in Section 4.7. The results clearly demonstrate the ability of this method to inscribe complex apodization profiles with high accuracy and resolution, over a large dynamic range and with a spatial resolution of only a few µms (limited by the period Λ_ϕ of the phase modulation). In this example a period of $\Lambda_\phi = 2.5\ \mu m$ was used to realize a structure with stringent resolution requirements, but in most situation, a period of $\Lambda_\phi = 10\ \mu m$ was found to provide sufficient resolution and adequate spacing between the Fourier components of the grating. By leveraging this high spatial resolution, FBGs that were previously impossible to inscribe using conventional UV techniques could be realized. Even though many apodization methods have been used for the direct-writing of FBGs (see Section 2.4), the ability to maintain a constant average RIM using the phase modulation approach offers superior performances in terms of spectral response and avoids the need to calibrate κ as a function of the pulse energy, the lateral displacement or other experimental parameters. Overall, these key attributes provide an efficient and reliable way for FBGs apodization with direct-writing methods.

These advancements were only possible because of the PSO tracking feature of the Aerotech translation stage motor controller. The phase control strategy developed around this feature has shown to be capable of controlling the exact position of each RIM with great precision, which is a crucial requirement for phase modulation. Note that the concept of phase modulation could be also implemented with a LbL method, where the translation stage stops at each RIM position before triggering the laser, but LbL is significantly more time consuming compared to PbP or Pl-b-Pl. However, it would make it possible to avoid the necessity of PSO tracking.

Clearly, the full potential of PSO tracking has yet to be evaluated, and this feature should bring many new opportunities for the development of advanced photonic devices. For instance, further investigations could probably exploit PSO tracking to inscribe FBGs using a multi-pass approach [81], which could improve their spectral qualities and the reproducibility of the writing process.

6.3 Fiber core position mapping

An important aspect of every direct-writing system is the procedure used to track the core position of the fiber. The novel alignment method proposed in this thesis has shown that it is possible to track the fiber core position with sub-micrometer accuracy (in the transverse plane), using nothing but probe FBGs and an OFDR system to measure their individual reflectivity. It was found that this procedure can map the core position of different types of fibers such as a polyimide coated fiber or an uncoated SMF-28 fiber.

However, since the OFDR method is fundamentally different from a camera system, it has many distinct characteristics. For example, it does not need to visually distinguish the boundaries of the core to locate its position, allowing to track the core position of special fibers in which it might be difficult to clearly see the core using a simple microscope setup, such as fiber with thick coating, small core, low core-cladding RI difference, multiple cores, etc. This features also allows to avoid the need for oil index-matching compensation techniques, which are sometimes employed just to get a better picture of the core. However, further investigations are needed to confirm the extent of this capability, as the study was only conducted for two types of fiber.

This alignment method can also be described as “absolute”, since the optimal position returned by the procedure is not relative to anything else than the core center. This is not the case for a camera system, as the core position is relative to the offset between the focal spot of the laser and camera, which needs to be calibrated. Thus, the OFDR method is calibration-free.

Some limitations were also identified for the OFDR method. Primary, it requires to have an OFDR system with a high-dynamic range. Because several probes need to be inscribed to find the optimal position, it has a low longitudinal resolution compared to what is possible with a camera system. It is also relatively slow, taking up to 25 seconds for each iteration of the process. In the case of coated fibers, variations of the coating thickness or curvature can induce large fluctuations of the focal spot position, which can be difficult to track depending on the amplitude and frequency of the fluctuation. Nevertheless, this new method provides an alternative to the camera method, and it has some unique attributes. It could be worth to implement a camera system just to carry out an exhaustive comparison between both types of system. Perhaps the combination of the two could be used to collect more data about the core position, which could

improve the performance of the mapping process even more. Alternatively, a better fibre coating uniformity could significantly improve mapping using the method discussed in this thesis. Furthermore, even though no oil compensation techniques were used during the study, it might be valuable to design a modular V-groove glass plate that could be clipped on-and-off the translation stage to help mitigating situations where the coating geometry exhibits large fluctuations. Finally, an interesting study would be to test the possibility of tracking the position of an individual core in a multicore fiber, with potential for advanced sensor applications [125-127].

CHAPTER 7 CONCLUSION

This research aimed at developing and implementing a versatile FS direct-writing system that is capable of inscribing advanced FBGs. Based on a thorough analysis of contemporary direct-writing methods, various solutions were proposed and demonstrated to solve existing challenges. Not only did the findings enable the fabrication of advanced FBGs with high spectral qualities, but they also contributed to some improvements in this research field. Apodization by phase modulation certainly fills a gap in the pool of apodization methods suitable for FS direct-writing schemes, and PSO tracking offers an elegant way to control the position of the RIMs. The multi-pulse approach has shown great potential towards the realization of FBGs with higher reflectivity and lower losses, and the novel alignment technique has provided an alternative approach to track the fiber core position. By publishing the results in Optics Express, the ideas that were explored during this work will hopefully contribute to the advancement of direct-writing fabrication methods.

In CHAPTER 5 of this thesis, the full potential of the developed direct-writing system was shown by the realization of FBG-based sensors and filters, which may lead to important applications in the fields of distributed sensing and optical signal processing. Using the excellent capabilities of the writing system, many other applications may now be considered. For example, it opens doors to the development of novel filters which could be used in telecommunication systems for signal processing, wavelength division multiplexing, or dispersion compensation. The possibility to inscribe high-quality FBGs using a FS direct-writing system also allows for new opportunities in many other fields of application, such as fiber sensors, biomedical instruments, fiber lasers, astronomical filters, and many more.

REFERENCES

[1] K. O. Hill, Y. Fujii, D. C. Johnson, and B. S. Kawasaki, "Photosensitivity in optical fiber waveguides: Application to reflection filter fabrication," *Applied Physics Letters,* vol. 32, no. 10, pp. 647-649, 1978, doi: 10.1063/1.89881.

[2] R. Kashyap, *Fiber Bragg Gratings*. Academic Press, 2010.

[3] G. Meltz, W. W. Morey, and W. H. Glenn, "Formation of Bragg gratings in optical fibers by a transverse holographic method," *Opt Lett,* vol. 14, no. 15, pp. 823-5, Aug 1 1989, doi: 10.1364/ol.14.000823.

[4] K. M. Davis, K. Miura, N. Sugimoto, and K. Hirao, "Writing waveguides in glass with a femtosecond laser," *Opt Lett,* vol. 21, no. 21, pp. 1729-31, Nov 1 1996, doi: 10.1364/ol.21.001729.

[5] R. Osellame, G. Cerullo, and R. Ramponi, *Femtosecond Laser Micromachining: Photonic and Microfluidic Devices in Transparent Materials*. Springer, 2012.

[6] S. J. Mihailov *et al.*, "Fiber bragg gratings made with a phase mask and 800-nm femtosecond radiation," *Opt Lett,* vol. 28, no. 12, pp. 995-7, Jun 15 2003, doi: 10.1364/ol.28.000995.

[7] A. Dragomir, D. N. Nikogosyan, K. A. Zagorulko, P. G. Kryukov, and E. M. Dianov, "Inscription of fiber Bragg gratings by ultraviolet femtosecond radiation," *Opt Lett,* vol. 28, no. 22, pp. 2171-3, Nov 15 2003, doi: 10.1364/ol.28.002171.

[8] A. Martinez, M. Dubov, I. Khrushchev, and I. Bennion, "Direct writing of fibre Bragg gratings by femtosecond laser," *Electronics Letters,* vol. 40, no. 19, 2004, doi: 10.1049/el:20046050.

[9] S. J. Mihailov, D. Grobnic, and C. W. Smelser, "Efficient grating writing through fibre coating with femtosecond IR radiation and phase mask," *Electronics Letters,* vol. 43, no. 8, 2007, doi: 10.1049/el:20070114.

[10] A. Martinez, I. Y. Khrushchev, and I. Bennion, "Direct inscription of Bragg gratings in coated fibers by an infrared femtosecond laser," *Opt Lett,* vol. 31, no. 11, pp. 1603-5, Jun 1 2006, doi: 10.1364/ol.31.001603.

[11] S. Loranger, "Discovery and Correction of Spatial Non-Uniformity in Optical Fibers: Towards the Fabrication of Perfect Ultra-Long Fiber Bragg Gratings for Applications in Non-Linear Optics," PhD thesis, École Polytechnique de Montréal, 2018. [Online]. Available: https://publications.polymtl.ca/2997/

[12] M. Gagne, S. Loranger, J. Lapointe, and R. Kashyap, "Fabrication of high quality, ultra-long fiber Bragg gratings: up to 2 million periods in phase," *Opt Express,* vol. 22, no. 1, pp. 387-98, Jan 13 2014, doi: 10.1364/OE.22.000387.

[13] S. Loranger, V. Lambin-Iezzi, and R. Kashyap, "Reproducible ultra-long FBGs in phase corrected non-uniform fibers," *Optica,* vol. 4, no. 9, 2017, doi: 10.1364/optica.4.001143.

[14] G. D. Marshall, R. J. Williams, N. Jovanovic, M. J. Steel, and M. J. Withford, "Point-by-point written fiber-Bragg gratings and their application in complex grating designs," *Opt Express,* vol. 18, no. 19, pp. 19844-59, Sep 13 2010, doi: 10.1364/OE.18.019844.

[15] A. Roberge, S. Loranger, J.-S. Boisvert, F. Monet, and R. Kashyap, "Femtosecond laser direct-writing of high quality first-order Bragg gratings with arbitrary complex apodization by phase modulation," *Optics Express,* vol. 30, no. 17, 2022, doi: 10.1364/oe.465331.

[16] T. Erdogan, "Fiber grating spectra," *Journal of Lightwave Technology,* vol. 15, no. 8, pp. 1277-1294, 1997, doi: 10.1109/50.618322.

[17] R. Kashyap, "Chapter 4 - Theory of Fiber Bragg Gratings," in *Fiber Bragg Gratings (Second Edition)*, R. Kashyap Ed. Boston: Academic Press, 2010, pp. 119-187.

[18] A. Othonos, K. Kalli, D. Pureur, and A. Mugnier, "Fibre Bragg Gratings," in *Wavelength Filters in Fibre Optics*, (Springer Series in Optical Sciences, 2006, ch. Chapter 6, pp. 189-269.

[19] R. Kashyap, "Chapter 5 - Apodization of Fiber Gratings," in *Fiber Bragg Gratings (Second Edition)*, R. Kashyap Ed. Boston: Academic Press, 2010, pp. 189-215.

[20] C. C. Katsidis and D. I. Siapkas, "General transfer-matrix method for optical multilayer systems with coherent, partially coherent, and incoherent interference," *Appl Opt,* vol. 41, no. 19, pp. 3978-87, Jul 1 2002, doi: 10.1364/ao.41.003978.

[21] A. Mafi, "Anderson localization in a partially random Bragg grating and a conserved area theorem," *Opt Lett,* vol. 40, no. 15, pp. 3603-6, Aug 1 2015, doi: 10.1364/OL.40.003603.

[22] R. Cheng, Y. Han, and L. Chrostowski, "Characterization and compensation of apodization phase noise in silicon integrated Bragg gratings," *Opt Express,* vol. 27, no. 7, pp. 9516-9535, Apr 1 2019, doi: 10.1364/OE.27.009516.

[23] Puhan, Burmen, Tuma, and Fajfar, "Irradiance in Mixed Coherent/Incoherent Structures: An Analytical Approach," *Coatings,* vol. 9, no. 9, 2019, doi: 10.3390/coatings9090536.

[24] Z. H. Wang, G.-D. Peng, and P. L. Chu, "Improved Rouard's method for fiber and waveguide gratings," *Optics Communications,* vol. 177, no. 1-6, pp. 245-250, 2000, doi: 10.1016/s0030-4018(00)00579-4.

[25] E. Chehura, S. W. James, and R. P. Tatam, "Rouard's method as a modelling tool for the sensing characteristics of complex fibre Fabry-Perot interferometers formed between chirped fibre Bragg gratings," presented at the 17th International Conference on Optical Fibre Sensors, 2005.

[26] L. A. Weller-Brophy and D. G. Hall, "Analysis of waveguide gratings: application of Rouard's method," *Journal of the Optical Society of America A,* vol. 2, no. 6, 1985, doi: 10.1364/josaa.2.000863.

[27] R. Kashyap, "Chapter 2 - Photosensitivity and Photosensitization of Optical Fibers," in *Fiber Bragg Gratings (Second Edition)*, R. Kashyap Ed. Boston: Academic Press, 2010, pp. 15-51.

[28] R. Kashyap, "Chapter 1 - Introduction," in *Fiber Bragg Gratings (Second Edition)*, R. Kashyap Ed. Boston: Academic Press, 2010, pp. 1-13.

[29] R. Kashyap, "Chapter 3 - Fabrication of Bragg Gratings," in *Fiber Bragg Gratings (Second Edition)*, R. Kashyap Ed. Boston: Academic Press, 2010, pp. 53-118.

[30] R. Kashyap, "Chapter 11 - Femtosecond-Induced Refractive Index Changes in Glass," in *Fiber Bragg Gratings (Second Edition)*, R. Kashyap Ed. Boston: Academic Press, 2010, pp. 503-526.

[31] R. R. Gattass and E. Mazur, "Femtosecond laser micromachining in transparent materials," *Nature Photonics,* vol. 2, no. 4, pp. 219-225, 2008, doi: 10.1038/nphoton.2008.47.

[32] S. A. Slattery, D. N. Nikogosyan, and G. Brambilla, "Fiber Bragg grating inscription by high-intensity femtosecond UV laser light: comparison with other existing methods of fabrication," *Journal of the Optical Society of America B,* vol. 22, no. 2, 2005, doi: 10.1364/josab.22.000354.

[33] A. M. Weiner, "Ultrafast Optics," 2009.

[34] P. P. Rajeev, M. Gertsvolf, P. B. Corkum, and D. M. Rayner, "Field dependent avalanche ionization rates in dielectrics," *Phys Rev Lett,* vol. 102, no. 8, p. 083001, Feb 27 2009, doi: 10.1103/PhysRevLett.102.083001.

[35] S. Gross, M. Dubov, and M. J. Withford, "On the use of the Type I and II scheme for classifying ultrafast laser direct-write photonics," *Opt Express,* vol. 23, no. 6, pp. 7767-70, Mar 23 2015, doi: 10.1364/OE.23.007767.

[36] H. Zhang, S. M. Eaton, and P. R. Herman, "Single-step writing of Bragg grating waveguides in fused silica with an externally modulated femtosecond fiber laser," *Opt Lett,* vol. 32, no. 17, pp. 2559-61, Sep 1 2007, doi: 10.1364/ol.32.002559.

[37] C. B. Schaffer, J. F. García, and E. Mazur, "Bulk heating of transparent materials using a high-repetition-rate femtosecond laser," *Applied Physics A: Materials Science & Processing,* vol. 76, no. 3, pp. 351-354, 2003, doi: 10.1007/s00339-002-1819-4.

[38] M. Ams, P. Dekker, S. Gross, and M. J. Withford, "Fabricating waveguide Bragg gratings (WBGs) in bulk materials using ultrashort laser pulses," *Nanophotonics,* vol. 6, no. 5, pp. 743-763, 2017, doi: 10.1515/nanoph-2016-0119.

[39] P. Roldan-Varona, D. Pallares-Aldeiturriaga, L. Rodriguez-Cobo, and J. M. Lopez-Higuera, "Slit Beam Shaping Technique for Femtosecond Laser Inscription of Enhanced Plane-by-Plane FBGs," *Journal of Lightwave Technology,* vol. 38, no. 16, pp. 4526-4532, 2020, doi: 10.1109/jlt.2020.2992568.

[40] P. Lu *et al.*, "Plane-by-Plane Inscription of Grating Structures in Optical Fibers," *Journal of Lightwave Technology,* vol. 36, no. 4, pp. 926-931, 2018, doi: 10.1109/jlt.2017.2750490.

[41] K. Chah, D. Kinet, M. Wuilpart, P. Megret, and C. Caucheteur, "Femtosecond-laser-induced highly birefringent Bragg gratings in standard optical fiber," *Opt Lett,* vol. 38, no. 4, pp. 594-6, Feb 15 2013, doi: 10.1364/OL.38.000594.

[42] N. Jovanovic *et al.*, "Polarization-dependent effects in point-by-point fiber Bragg gratings enable simple, linearly polarized fiber lasers," *Opt Express,* vol. 17, no. 8, pp. 6082-95, Apr 13 2009, doi: 10.1364/oe.17.006082.

[43] C. Caucheteur, T. Guo, and J. Albert, "Polarization-Assisted Fiber Bragg Grating Sensors: Tutorial and Review," *Journal of Lightwave Technology,* vol. 35, no. 16, pp. 3311-3322, 2017, doi: 10.1109/jlt.2016.2585738.

[44] J. Thomas *et al.*, "Cladding mode coupling in highly localized fiber Bragg gratings: modal properties and transmission spectra," *Opt Express,* vol. 19, no. 1, pp. 325-41, Jan 3 2011, doi: 10.1364/OE.19.000325.

[45] Y. Chen, Y. Lai, and M. W. Cheong, "Distortion-free femtosecond laser inscription in free-standing optical fiber," *Appl Opt,* vol. 55, no. 21, pp. 5575-9, Jul 20 2016, doi: 10.1364/AO.55.005575.

[46] M. Ams, G. Marshall, D. Spence, and M. Withford, "Slit beam shaping method for femtosecond laser direct-write fabrication of symmetric waveguides in bulk glasses," *Opt Express,* vol. 13, no. 15, pp. 5676-81, Jul 25 2005, doi: 10.1364/opex.13.005676.

[47] R. Osellame *et al.*, "Femtosecond writing of active optical waveguides with astigmatically shaped beams," *Journal of the Optical Society of America B,* vol. 20, no. 7, 2003, doi: 10.1364/josab.20.001559.

[48] P. S. Salter, M. J. Woolley, S. M. Morris, M. J. Booth, and J. A. J. Fells, "Femtosecond fiber Bragg grating fabrication with adaptive optics aberration compensation," *Opt Lett,* vol. 43, no. 24, pp. 5993-5996, Dec 15 2018, doi: 10.1364/OL.43.005993.

[49] S. Antipov, M. Ams, R. J. Williams, E. Magi, M. J. Withford, and A. Fuerbach, "Direct infrared femtosecond laser inscription of chirped fiber Bragg gratings," *Opt Express,* vol. 24, no. 1, pp. 30-40, Jan 11 2016, doi: 10.1364/OE.24.000030.

[50] G. Bharathan *et al.*, "Femtosecond laser direct-written fiber Bragg gratings with high reflectivity and low loss at wavelengths beyond 4 microm," *Opt Lett,* vol. 45, no. 15, pp. 4316-4319, Aug 1 2020, doi: 10.1364/OL.399329.

[51] E. Ertorer, M. Haque, J. Li, and P. R. Herman, "Femtosecond laser filaments for rapid and flexible writing of fiber Bragg grating," *Opt Express,* vol. 26, no. 7, pp. 9323-9331, Apr 2 2018, doi: 10.1364/OE.26.009323.

[52] Y. Yu, J. Shi, F. Han, W. Sun, and X. Feng, "High-precision fiber Bragg gratings inscription by infrared femtosecond laser direct-writing method assisted with image recognition," *Opt Express,* vol. 28, no. 6, pp. 8937-8948, Mar 16 2020, doi: 10.1364/OE.388393.

[53] A. V. Dostovalov, A. A. Wolf, A. V. Parygin, V. E. Zyubin, and S. A. Babin, "Femtosecond point-by-point inscription of Bragg gratings by drawing a coated fiber through ferrule," *Opt Express,* vol. 24, no. 15, pp. 16232-7, Jul 25 2016, doi: 10.1364/OE.24.016232.

[54] X. Xu *et al.*, "Slit beam shaping for femtosecond laser point-by-point inscription of high-quality fiber Bragg gratings," *Journal of Lightwave Technology,* pp. 1-1, 2021, doi: 10.1109/jlt.2021.3082566.

[55] R. R. Thomson *et al.*, "Shaping ultrafast laser inscribed optical waveguides using a deformable mirror," *Opt Express,* vol. 16, no. 17, pp. 12786-93, Aug 18 2008, doi: 10.1364/oe.16.012786.

[56] P. S. Westbrook *et al.*, "Kilometer length, low loss enhanced back scattering fiber for distributed sensing," in *2017 25th Optical Fiber Sensors Conference (OFS)*, 24-28 April 2017 2017, pp. 1-5, doi: 10.1109/OFS.2017.7961121.

[57] J. Thomas *et al.*, "Inscription of fiber Bragg gratings with femtosecond pulses using a phase mask scanning technique," *Applied Physics A,* vol. 86, no. 2, pp. 153-157, 2006, doi: 10.1007/s00339-006-3754-2.

[58] J. He, B. Xu, X. Xu, C. Liao, and Y. Wang, "Review of Femtosecond-Laser-Inscribed Fiber Bragg Gratings: Fabrication Technologies and Sensing Applications," *Photonic Sensors,* vol. 11, no. 2, pp. 203-226, 2021, doi: 10.1007/s13320-021-0629-2.

[59] K. Zhou, M. Dubov, C. Mou, L. Zhang, V. K. Mezentsev, and I. Bennion, "Line-by-Line Fiber Bragg Grating Made by Femtosecond Laser," *IEEE Photonics Technology Letters,* vol. 22, no. 16, pp. 1190-1192, 2010, doi: 10.1109/lpt.2010.2050877.

[60] R. J. Williams, R. G. Kramer, S. Nolte, and M. J. Withford, "Femtosecond direct-writing of low-loss fiber Bragg gratings using a continuous core-scanning technique," *Opt Lett,* vol. 38, no. 11, pp. 1918-20, Jun 1 2013, doi: 10.1364/OL.38.001918.

[61] H.-J. Deyerl, N. Plougmann, J. B. Jensen, F. Floreani, H. R. Sørensen, and M. Kristensen, "Fabrication of advanced Bragg gratings with complex apodization profiles by use of the polarization control method," *Appl. Opt.,* vol. 43, no. 17, pp. 3513-3522, 2004/06/10 2004, doi: 10.1364/AO.43.003513.

[62] K. Tian, G.-X. Chen, and Q.-Y. Song, "A two-step scanning-mask exposure method for the fabrication of arbitrary apodized fiber gratings," *Optik,* vol. 141, pp. 24-31, 2017, doi: 10.1016/j.ijleo.2017.05.064.

[63] J. Albert *et al.*, "Apodisation of the spectral response of fibre Bragg gratings using a phase mask with variable diffraction efficiency," (in En), *Electronics Letters,* vol. 31, no. 3, pp. 222-223, 1995, doi: 10.1049/el:19950146.

[64] T. Osuch and Z. Jaroszewicz, "Numerical analysis of apodized fiber Bragg gratings formation using phase mask with variable diffraction efficiency," *Optics Communications,* vol. 284, no. 2, pp. 567-572, 2011, doi: 10.1016/j.optcom.2010.09.063.

[65] Q. Guo *et al.*, "Femtosecond Laser Fabricated Apodized Fiber Bragg Gratings Based on Energy Regulation," *Photonics,* vol. 8, no. 4, 2021, doi: 10.3390/photonics8040110.

[66] I. Ulyanov, D. V. Przhiialkovskii, and O. V. Butov, "Point-by-point inscription of chirped apodized fiber Bragg gratings for application as ultrashort pulse stretchers," *Results in Physics,* vol. 32, 2022, doi: 10.1016/j.rinp.2021.105101.

[67] T. A. Goebel *et al.*, "Realization of aperiodic fiber Bragg gratings with ultrashort laser pulses and the line-by-line technique," *Opt Lett,* vol. 43, no. 15, pp. 3794-3797, Aug 1 2018, doi: 10.1364/OL.43.003794.

[68] J. He *et al.*, "Femtosecond laser line-by-line inscription of apodized fiber Bragg gratings," *Opt Lett,* vol. 46, no. 22, pp. 5663-5666, Nov 15 2021, doi: 10.1364/OL.441888.

[69] R. J. Williams *et al.*, "Point-by-point inscription of apodized fiber Bragg gratings," *Opt Lett,* vol. 36, no. 15, pp. 2988-90, Aug 1 2011, doi: 10.1364/OL.36.002988.

[70] R. J. Williams, R. G. Kramer, S. Nolte, M. J. Withford, and M. J. Steel, "Detuning in apodized point-by-point fiber Bragg gratings: insights into the grating morphology," *Opt Express,* vol. 21, no. 22, pp. 26854-67, Nov 4 2013, doi: 10.1364/OE.21.026854.

[71] R. Cheng and L. Chrostowski, "Apodization of Silicon Integrated Bragg Gratings Through Periodic Phase Modulation," *IEEE Journal of Selected Topics in Quantum Electronics,* vol. 26, no. 2, pp. 1-15, 2020, doi: 10.1109/jstqe.2019.2929698.

[72] S. Kaushal *et al.*, "Optical signal processing based on silicon photonics waveguide Bragg gratings: review," *Frontiers of Optoelectronics,* vol. 11, no. 2, pp. 163-188, 2018, doi: 10.1007/s12200-018-0813-1.

[73] A. D. Simard, N. Belhadj, Y. Painchaud, and S. LaRochelle, "Apodized Silicon-on-Insulator Bragg Gratings," *IEEE Photonics Technology Letters,* vol. 24, no. 12, pp. 1033-1035, 2012, doi: 10.1109/lpt.2012.2194278.

[74] X. P. Pan *et al.*, "Femtosecond laser inscribed chirped fiber Bragg gratings," *Opt Lett,* vol. 46, no. 9, pp. 2059-2062, May 1 2021, doi: 10.1364/OL.422576.

[75] Y. Zhang, Y. Zhu, D. Qiao, and P. Jiang, "Fiber Bragg gratings fabricated by femtosecond lasers for narrow-linewidth fiber laser," *Optik,* vol. 223, 2020, doi: 10.1016/j.ijleo.2020.165451.

[76] A. Halstuch, A. Shamir, and A. A. Ishaaya, "Femtosecond inscription of fiber Bragg gratings through the coating with a Low-NA lens," *Opt Express,* vol. 27, no. 12, pp. 16935-16944, Jun 10 2019, doi: 10.1364/OE.27.016935.

[77] M. Bernier, F. Trepanier, J. Carrier, and R. Vallee, "High mechanical strength fiber Bragg gratings made with infrared femtosecond pulses and a phase mask," *Opt Lett,* vol. 39, no. 12, pp. 3646-9, Jun 15 2014, doi: 10.1364/OL.39.003646.

[78] C. Hnatovsky, D. Grobnic, and S. J. Mihailov, "Through-the-coating femtosecond laser inscription of very short fiber Bragg gratings for acoustic and high temperature sensing applications," *Opt Express,* vol. 25, no. 21, pp. 25435-25446, Oct 16 2017, doi: 10.1364/OE.25.025435.

[79] C. Hnatovsky, D. Grobnic, and S. J. Mihailov, "Nonlinear photoluminescence imaging applied to femtosecond laser manufacturing of fiber Bragg gratings," *Opt Express,* vol. 25, no. 13, pp. 14247-14259, Jun 26 2017, doi: 10.1364/OE.25.014247.

[80] W. He, J. Zhao, M. Dong, F. Meng, and L. Zhu, "Wavelength-switchable erbium-doped fiber laser incorporating fiber Bragg grating array fabricated by infrared femtosecond laser inscription," *Optics & Laser Technology,* vol. 127, 2020, doi: 10.1016/j.optlastec.2019.106026.

[81] D. V. Przhiialkovskii and O. V. Butov, "High-precision point-by-point fiber Bragg grating inscription," *Results in Physics,* vol. 30, 2021, doi: 10.1016/j.rinp.2021.104902.

[82] Corning. "Corning® SMF-28® Ultra Optical Fiber - Product Information." https://www.corning.com/media/worldwide/coc/documents/Fiber/product-information-sheets/PI-1424-AEN.pdf (accessed June, 2022).

[83] Fibercore. "Polyimide Coated SM Fiber." https://fibercore.humaneticsgroup.com/products/single-mode-sm-fiber/polyimide-coated-sm-fiber/sm1250104125p (accessed June, 2022).

[84] Aerotech. "Position Synchronized Output (PSO) – Coordinate Part Position with Process Control." https://www.aerotech.com/position-synchronized-output-pso-coordinate-part-position-with-process-control/ (accessed November 19, 2021).

[85] B. Soller, D. Gifford, M. Wolfe, and M. Froggatt, "High resolution optical frequency domain reflectometry for characterization of components and assemblies," *Opt Express,* vol. 13, no. 2, pp. 666-74, Jan 24 2005, doi: 10.1364/opex.13.000666.

[86] E. Udd *et al.*, "Optical frequency domain reflectometry: principles and applications in fiber optic sensing," presented at the Fiber Optic Sensors and Applications XIII, 2016.

[87] LUNA. "Optical Backscatter Reflectometer 4600 : User Guide." https://lunainc.com/product/obr-4600 (accessed May 18, 2022).

[88] A. Rahman, K. Madhav, and M. M. Roth, "Complex phase masks for OH suppression filters in astronomy: part I: design," *Opt Express,* vol. 28, no. 19, pp. 27797-27807, Sep 14 2020, doi: 10.1364/OE.402989.

[89] T. Geernaert *et al.*, "Point-by-point fiber Bragg grating inscription in free-standing step-index and photonic crystal fibers using near-IR femtosecond laser," *Opt Lett,* vol. 35, no. 10, pp. 1647-9, May 15 2010, doi: 10.1364/OL.35.001647.

[90] Y. Lai, K. Zhou, K. Sugden, and I. Bennion, "Point-by-point inscription of first-order fiber Bragg grating for C-band applications," *Opt Express,* vol. 15, no. 26, pp. 18318-25, Dec 24 2007, doi: 10.1364/oe.15.018318.

[91] D. Pallares-Aldeiturriaga, P. Roldan-Varona, L. Rodriguez-Cobo, and J. M. Lopez-Higuera, "Optical Fiber Sensors by Direct Laser Processing: A Review," *Sensors (Basel),* vol. 20, no. 23, Dec 6 2020, doi: 10.3390/s20236971.

[92] S. Kaushal and J. Azaña, "Design of FBG-Based Linear Passive All-Optical NOT Gate," in *2019 Conference on Lasers and Electro-Optics Europe & European Quantum Electronics Conference (CLEO/Europe-EQEC)*, 2019, pp. 1-1, doi: 10.1109/CLEOE-EQEC.2019.8872328.

[93] I. Floris, J. M. Adam, P. A. Calderón, and S. Sales, "Fiber Optic Shape Sensors: A comprehensive review," *Optics and Lasers in Engineering,* vol. 139, 2021, doi: 10.1016/j.optlaseng.2020.106508.

[94] C. E. Campanella, A. Cuccovillo, C. Campanella, A. Yurt, and V. M. N. Passaro, "Fibre Bragg Grating Based Strain Sensors: Review of Technology and Applications," *Sensors (Basel),* vol. 18, no. 9, Sep 15 2018, doi: 10.3390/s18093115.

[95] Z. Ding *et al.*, "Distributed Optical Fiber Sensors Based on Optical Frequency Domain Reflectometry: A review," *Sensors (Basel),* vol. 18, no. 4, Apr 3 2018, doi: 10.3390/s18041072.

[96] P. Lu *et al.*, "Distributed optical fiber sensing: Review and perspective," *Applied Physics Reviews,* vol. 6, no. 4, 2019, doi: 10.1063/1.5113955.

[97] F. Parent *et al.*, "Enhancement of accuracy in shape sensing of surgical needles using optical frequency domain reflectometry in optical fibers," *Biomed Opt Express,* vol. 8, no. 4, pp. 2210-2221, Apr 1 2017, doi: 10.1364/BOE.8.002210.

[98] F. Monet *et al.*, "High-Resolution Optical Fiber Shape Sensing of Continuum Robots: A Comparative Study," *IEEE Int Conf Robot Autom,* vol. 2020, May-Aug 2020, doi: 10.1109/icra40945.2020.9197454.

[99] F. Monet, S. Loranger, V. Lambin-Iezzi, A. Drouin, S. Kadoury, and R. Kashyap, "The ROGUE: a novel, noise-generated random grating," *Opt Express,* vol. 27, no. 10, pp. 13895-13909, May 13 2019, doi: 10.1364/OE.27.013895.

[100] P. Lorre *et al.*, "Extruded optical fiber triplets for 3D shape sensing for minimally invasive surgery," presented at the Seventh European Workshop on Optical Fibre Sensors, 2019, EOF. [Online]. Available: https://doi.org/10.1117/12.2541323.

[101] J. Francoeur *et al.*, "Real-time 3D Shape Sensing with a Random Fiber Bragg Grating Triplet," in *Optical Sensors*, Vancouver, Canada, 11 july 2022: Optica Publishing Group, p. SM2C.2.

[102] A. M. Weiner, S. Oudin, D. H. Reitze, and D. E. Leaird, "Shaping of femtosecond pulses using phase-only filters designed by simulated annealing," *Journal of the Optical Society of America A,* vol. 10, no. 5, 1993, doi: 10.1364/josaa.10.001112.

[103] J. Azaña and L. R. Chen, "Synthesis of temporal optical waveforms by fiber Bragg gratings: a new approach based on space-to-frequency-to-time mapping," *Journal of the Optical Society of America B,* vol. 19, no. 11, 2002, doi: 10.1364/josab.19.002758.

[104] A. M. Weiner, "Ultrafast optical pulse shaping: A tutorial review," *Optics Communications,* vol. 284, no. 15, pp. 3669-3692, 2011, doi: 10.1016/j.optcom.2011.03.084.

[105] M. R. Fernández-Ruiz, A. Carballar, R. Ashrafi, S. LaRochelle, and J. Azaña, "All-Optical Pulse Shaping in the Sub-Picosecond Regime Based on Fiber Grating Devices," in *Shaping Light in Nonlinear Optical Fibers*, 2017, pp. 257-292.

[106] S. Thomas, A. Malacarne, F. Fresi, L. Poti, A. Bogoni, and J. Azana, "Programmable fiber-based picosecond optical pulse shaper using time-domain binary phase-only linear filtering," *Opt Lett,* vol. 34, no. 4, pp. 545-7, Feb 15 2009, doi: 10.1364/ol.34.000545.

[107] F. Ferdous *et al.*, "Spectral line-by-line pulse shaping of on-chip microresonator frequency combs," *Nature Photonics,* vol. 5, no. 12, pp. 770-776, 2011, doi: 10.1038/nphoton.2011.255.

[108] M. R. Fernández-Ruiz and A. Carballar, "Fiber Bragg Grating-Based Optical Signal Processing: Review and Survey," *Applied Sciences,* vol. 11, no. 17, 2021, doi: 10.3390/app11178189.

[109] J. Azaña, "Ultrafast Analog All-Optical Signal Processors Based on Fiber-Grating Devices," *IEEE Photonics Journal,* vol. 2, no. 3, pp. 359-386, 2010, doi: 10.1109/jphot.2010.2047941.

[110] R. Maram *et al.*, "Frequency-domain ultrafast passive logic: NOT and XNOR gates," *Nat Commun,* vol. 11, no. 1, p. 5839, Nov 17 2020, doi: 10.1038/s41467-020-19544-9.

[111] M. H. Asghari and J. Azana, "All-optical Hilbert transformer based on a single phase-shifted fiber Bragg grating: design and analysis," *Opt Lett,* vol. 34, no. 3, pp. 334-6, Feb 1 2009, doi: 10.1364/ol.34.000334.

[112] R. Maram, D. Kong, M. Galili, L. K. Oxenløwe, and J. Azaña, "Ultrafast All-Optical Clock Recovery Based on Phase-Only Linear Optical Filtering," in *Optical Fiber Communication Conference*, San Francisco, California, 2014/03/09 2014: Optica Publishing Group, in OSA Technical Digest (online), p. W3F.2, doi: 10.1364/OFC.2014.W3F.2. [Online]. Available: http://opg.optica.org/abstract.cfm?URI=OFC-2014-W3F.2

[113] S. Kaushal and J. Azaña, "Design of FBG-based Linear Passive All-optical NOT Gate," in *Conference on Lasers and Electro-Optics*, Munich, 2019/06/23 2019: Optica Publishing Group, in OSA Technical Digest, p. ci_p_5.

[114] S. Kaushal and J. Azana, "Design of Ultra-Compact On-Chip Discrete Phase Filters for Broadband Dispersion Management," *Journal of Lightwave Technology,* vol. 39, no. 21, pp. 6908-6921, 2021, doi: 10.1109/jlt.2021.3107834.

[115] S. Kaushal and J. Azaña, "Group-velocity Dispersion Compensation of Telecom Data Signals using Compact Discrete Phase Filters in Silicon," in *Optical Fiber Communication Conference (OFC) 2022*, San Diego, California, S. P. D. S. W. J. F. C. R. R. Matsuo and D. Simeonidou, Eds., 2022/03/06 2022: Optica Publishing Group, in Technical Digest Series, p. Th1D.3, doi: 10.1364/OFC.2022.Th1D.3. [Online]. Available: http://opg.optica.org/abstract.cfm?URI=OFC-2022-Th1D.3

[116] H. J. B. Marroux, A. P. Fidler, D. M. Neumark, and S. R. Leone, "Multidimensional spectroscopy with attosecond extreme ultraviolet and shaped near-infrared pulses," *Sci Adv,* vol. 4, no. 9, p. eaau3783, Sep 2018, doi: 10.1126/sciadv.aau3783.

[117] M. Kues *et al.*, "On-chip generation of high-dimensional entangled quantum states and their coherent control," *Nature,* vol. 546, no. 7660, pp. 622-626, Jun 28 2017, doi: 10.1038/nature22986.

[118] Z. Yang *et al.*, "A squeezed quantum microcomb on a chip," *Nat Commun,* vol. 12, no. 1, p. 4781, Aug 6 2021, doi: 10.1038/s41467-021-25054-z.

[119] S. Kaushal, A. Roberge, R. Kashyap, and J. Azaña, "Group-velocity Dispersion Compensation over a 70.56-km Fibre-optic Telecom Link using a cm-long In-fibre Device," in *IPC*, Vancouver, Canada, 2022: Accepted for publication.

[120] R. Leners, P. Emplit, D. Foursa, M. Haelterman, and R. Kashyap, "61-GHz dark-soliton generation and propagation by a fiber Bragg grating pulse-shaping technique," *Journal of the Optical Society of America B,* vol. 14, no. 9, 1997, doi: 10.1364/josab.14.002339.

[121] P. Emplit, M. Haelterman, R. Kashyap, and M. De Lathouwer, "Fiber Bragg grating for optical dark soliton generation," *IEEE Photonics Technology Letters,* vol. 9, no. 8, pp. 1122-1124, 1997, doi: 10.1109/68.605522.

[122] S. Kaushal, A. Roberge, R. Kashyap, and J. Azaña, "All-fiber based High-speed Linear Passive NOT Gate," in *Signal Processing in Photonic Communications*, Maastricht, Netherlands, 2022: Optica Publishing Group, p. SpTu4J.3.

[123] S. Kaushal, A. A. Rahim, A. Roberge, R. Morandotti, R. Kashyap, and J. Azaña, "All-fibre phase filters with 1-GHz resolution for high-speed passive optical logic processing," *Nat Commun: Submitted for publication,* 2022.

[124] R. J. Williams, N. Jovanovic, G. D. Marshall, G. N. Smith, M. J. Steel, and M. J. Withford, "Optimizing the net reflectivity of point-by-point fiber Bragg gratings: the role of scattering loss," *Opt Express,* vol. 20, no. 12, pp. 13451-6, Jun 4 2012, doi: 10.1364/OE.20.013451.

[125] A. Donko, M. Beresna, Y. Jung, J. Hayes, D. J. Richardson, and G. Brambilla, "Point-by-point femtosecond laser micro-processing of independent core-specific fiber Bragg gratings in a multi-core fiber," *Opt Express,* vol. 26, no. 2, pp. 2039-2044, Jan 22 2018, doi: 10.1364/OE.26.002039.

[126] A. Wolf, A. Dostovalov, K. Bronnikov, M. Skvortsov, S. Wabnitz, and S. Babin, "Advances in femtosecond laser direct writing of fiber Bragg gratings in multicore fibers: technology, sensor and laser applications," *Opto-Electronic Advances,* vol. 5, no. 4, pp. 210055-210055, 2022, doi: 10.29026/oea.2022.210055.

[127] Z. Zhao, M. Tang, and C. Lu, "Distributed multicore fiber sensors," *Opto-Electronic Advances,* vol. 3, no. 2, pp. 19002401-19002417, 2020, doi: 10.29026/oea.2020.190024.

[128] P. Vaveliuk and O. Martinez-Matos, "Effect of ABCD transformations on beam paraxiality," *Opt Express,* vol. 19, no. 27, pp. 25944-53, Dec 19 2011, doi: 10.1364/OE.19.025944.

[129] P. Vaveliuk, B. Ruiz, and A. Lencina, "Limits of the paraxial approximation in laser beams," *Opt Lett,* vol. 32, no. 8, pp. 927-9, Apr 15 2007, doi: 10.1364/ol.32.000927.

[130] P. Vaveliuk and O. Martinez-Matos, "Physical interpretation of the paraxial estimator," *Optics Communications,* vol. 285, no. 24, pp. 4816-4820, 2012, doi: 10.1016/j.optcom.2012.07.134.

APPENDIX A FOCAL SPOT SIMULATIONS

This section describes the model used to calculate the parameters and the intensity profile of the Gaussian beam as it propagates through the optical system used to shape the focal spot of the laser into a planar stripe, as illustrated in Figure 3.2 (a).

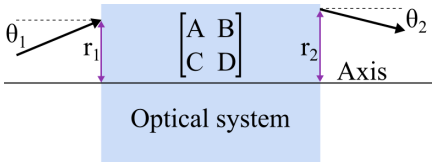

Figure A.1: The ABCD matrix transforms the input ray (r_1, θ_1) to the output (r_2, θ_2) ray.

To calculate how the different optical elements affect the laser beam, a ray transfer matrix analysis is considered. This method, shown in Figure A.1, describes the effect of an optical element or system by a 2x2 matrix, which relates the incoming light ray to the outgoing one by the following equation:

$$\begin{bmatrix} r_2 \\ \theta_2 \end{bmatrix} = \boldsymbol{T} \begin{bmatrix} r_1 \\ \theta_1 \end{bmatrix}; \quad \boldsymbol{T} = \begin{bmatrix} A & B \\ C & D \end{bmatrix}, \tag{A.1}$$

where r and θ are the distance and angle of the light ray relative to the reference optical axis.

A system which involves a cascade of multiple components can be describe by a single transfer matrix $\boldsymbol{T}$, obtained by multiplying the matrices of each element:

$$\boldsymbol{T} = \boldsymbol{T_N} \cdot \boldsymbol{T_{N-1}} \cdot \ldots \cdot \boldsymbol{T_2} \cdot \boldsymbol{T_1}. \tag{A.2}$$

The same ABCD matrices can also be used to calculate how the optical components affect the propagation of a Gaussian beam. To do so, it is possible to define a complex beam parameter, q, which containing information about the beam waist size and its curvature:

$$\frac{1}{q} = \frac{1}{R} - i\frac{\lambda}{\pi n \omega^2}; \quad q = (y - y_0) + iy_R \tag{A.3}$$

where R is the curvature, λ the wavelength, n the refractive index, ω the waist size, y the position along the optical axis, y_0 the position of minimal waist size, and y_R the Rayleigh range. Note that

the y-axis has been chosen for the direction of propagation to be consistent with the rest of this thesis.

The effect of an optical components on the q parameter is described by:

$$q_2 = \frac{Aq_1 + B}{Cq_1 + D}; \quad \frac{1}{q_2} = \frac{C + D/q_1}{A + B/q_1} \tag{A.4}$$

The diagram representing the optical system used to shape the beam and focus it down the core of an optical fiber is shown in Figure A.2, and the ABCD matrices corresponding to each optical element are given in Table A.1.

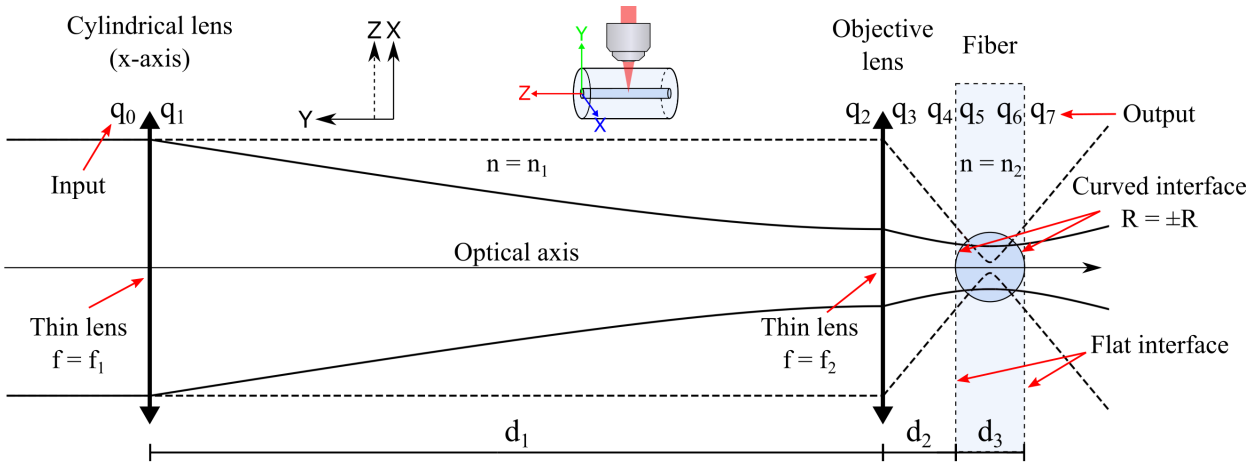

Figure A.2: Diagram of the optical system used to shape the focal spot of the laser beam into a plane. Since a cylindrical lens is used, the system is astigmatic, and this diagram illustrates the beam propagation in both the xy (solid line) and zy (dashed line) planes. The beam can be fully described by calculating the complex q parameter after each optical element.

Table A.1: ABCD transfer matrices for the optical components contained in Figure A.2

Optical element	ABCD matrix	Definition
Free space propagation	$\begin{bmatrix} 1 & d \\ 0 & 1 \end{bmatrix}$	d: Distance
Thin lens	$\begin{bmatrix} 1 & 0 \\ -1/f & 1 \end{bmatrix}$	f: Focal length ($f > 0$ for converging lens)
Refraction at a flat interface	$\begin{bmatrix} 1 & 0 \\ 0 & n_1/n_2 \end{bmatrix}$	n_1, n_2: Input/output refractive index

Refraction at a curved interface	$\begin{bmatrix} 1 & 0 \\ \frac{n_1 - n_2}{Rn_2} & \frac{n_1}{n_2} \end{bmatrix}$	n_1, n_2: Input/output refractive index R: Curvature radius ($R > 0$ when convex)

The transfer matrices describing the beam propagation in the xy-plane and zy-plane of this system are given by:

$$\boldsymbol{T_{xy}} = \begin{bmatrix} 1 & 0 \\ \frac{n_2 - n_1}{-Rn_1} & \frac{n_2}{n_1} \end{bmatrix} \begin{bmatrix} 1 & d \\ 0 & 1 \end{bmatrix} \begin{bmatrix} 1 & 0 \\ \frac{n_1 - n_2}{Rn_2} & \frac{n_1}{n_2} \end{bmatrix} \begin{bmatrix} 1 & d_2 \\ 0 & 1 \end{bmatrix} \begin{bmatrix} 1 & 0 \\ -1/f_2 & 1 \end{bmatrix} \begin{bmatrix} 1 & d_1 \\ 0 & 1 \end{bmatrix} \begin{bmatrix} 1 & 0 \\ -1/f_1 & 1 \end{bmatrix} \quad \text{(A.5)}$$

$$\boldsymbol{T_{zy}} = \begin{bmatrix} 1 & 0 \\ 0 & n_2/n_1 \end{bmatrix} \begin{bmatrix} 1 & d_3 \\ 0 & 1 \end{bmatrix} \begin{bmatrix} 1 & 0 \\ 0 & n_1/n_2 \end{bmatrix} \begin{bmatrix} 1 & d_2 \\ 0 & 1 \end{bmatrix} \begin{bmatrix} 1 & 0 \\ -1/f_2 & 1 \end{bmatrix} \quad \text{(A.6)}$$

Using Eq. (A.3) to (A.6), the complex q parameter can be calculate after each optical element, from which the parameters describing the Gaussian beam can be extracted (ω, y_0, y_R). The focal waist size (ω_0) is related to Rayleigh range (y_R) by:

$$y_R = \frac{\pi \omega_0^2 n}{\lambda} \quad \text{(A.7)}$$

Finally, these parameters can be used to calculate the intensity profile of the focal spot with Eq. (2.32) to (2.34). Different examples are shown in Table A.2 and A.3.

Despite being simple, the ABCD matrix method is based on the paraxial approximation which requires the angle between the beam and optical axis to stay small for the calculations to be accurate. In our case, the maximal NA value for which the paraxial approximation is still valid is ambiguous, and care should be taken when interpreting the simulation results for NA > 0.6. Perhaps the next step to answer this question could be to evaluate the effect of ABCD transformations on beam paraxiality following the work of Vaveliuk *et al.* [128-130], or explore another non-paraxial vectorial beam propagation model. Another limitation of this model is that it does not consider some optical aberrations. This being said, the paraxial model presented above is still a good tool to understand the underlying principles of the beam shaping techniques used to fabricate FBGs with a Pl-b-Pl writing scheme, and it is useful to analyse how different experimental parameters can affect the beam propagation.

Table A.2: Cross-sections of the normalized intensity profile of the focal spot over the transverse (xy) and longitudinal (zy) planes of the fiber, considering different focussing conditions. The objective can have different values of NA (0.5, 0.65 and 0.8) or clear aperture. The beam diameter can be adjusted to be equal or below the clear aperture. When equal, the NA of the objective is said to be "matched", but a smaller beam diameter decreases the NA of the focussed beam. The astigmatism induced by the fiber curvature is also considered.

Objective N.A.		0.5		0.65		0.8	
Clear ap. (mm)	Beam diam. (mm)	Intensity profile XY plane	Intensity profile ZY plane	Intensity profile XY plane	Intensity profile ZY plane	Intensity profile XY plane	Intensity profile ZY plane
3.5	3.5	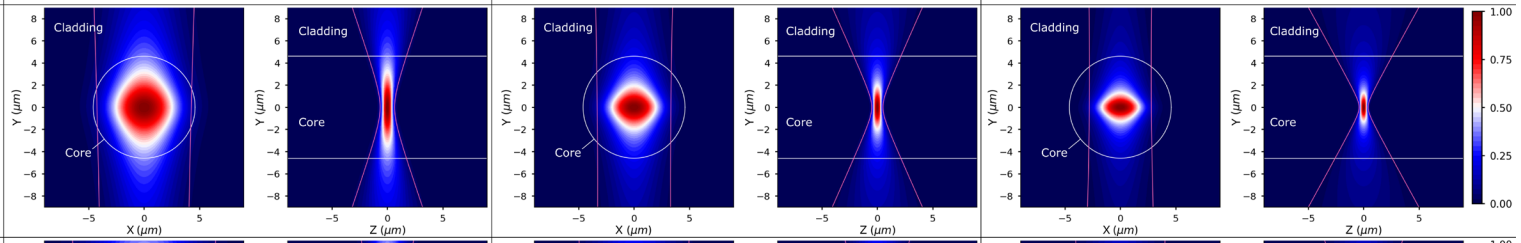					
5	3.5	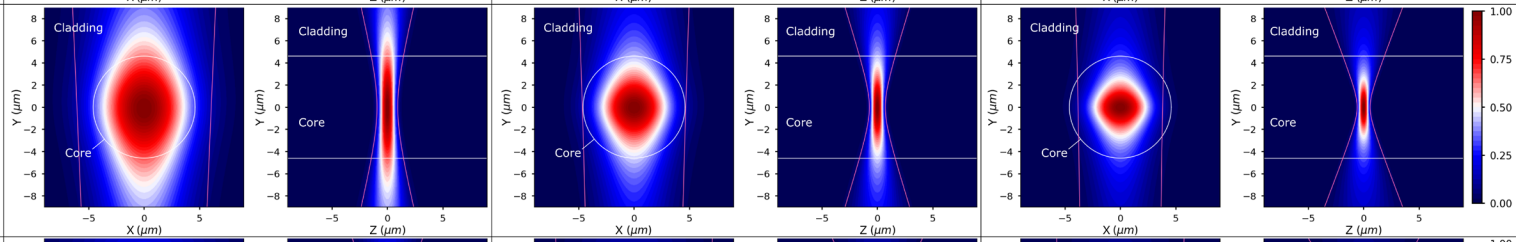					
5	5	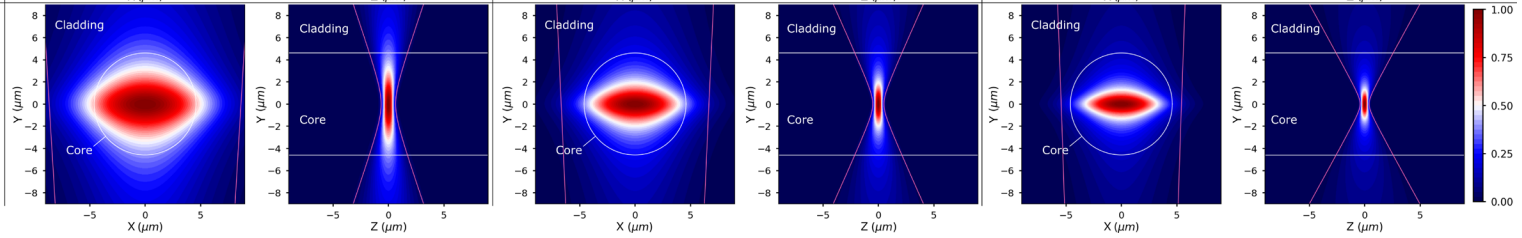					

Table A.2: Continued

Objective N.A.		0.5		0.65		0.8	
Clear ap. (mm)	Beam diam. (mm)	Intensity profile XY plane	Intensity profile ZY plane	Intensity profile XY plane	Intensity profile ZY plane	Intensity profile XY plane	Intensity profile ZY plane
9	5	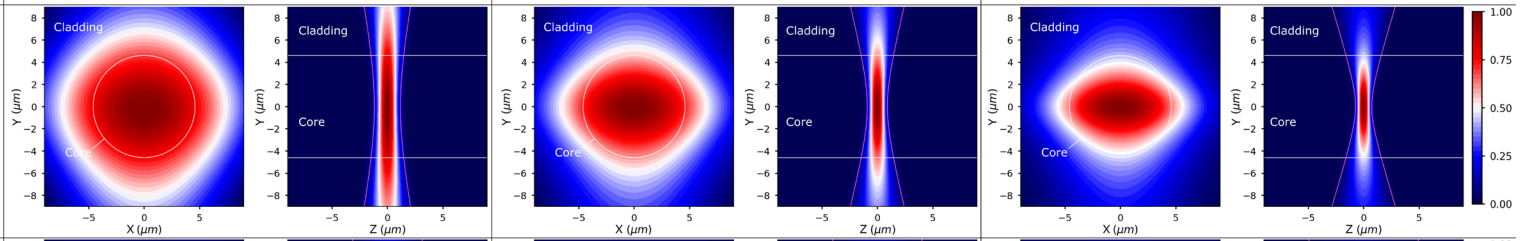					
9	9	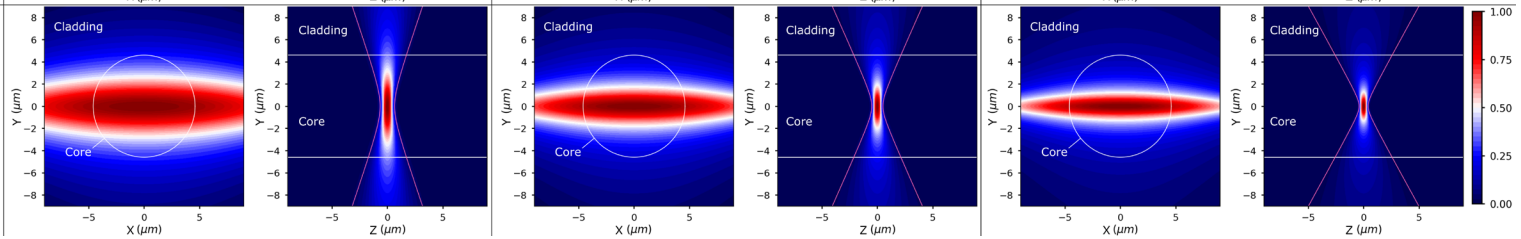					

Table A.3: (Upper row) Illustration of the beam waist as it propagates through the fiber for different distances between the cylindrical lens and the focussing objective. (Lower row) Corresponding normalized intensity profile of the focal spot. It is possible to notice that changing the position between the lens by a few cm only slightly affects the shape of the focal spot, where a small expansion of its width can be observed when reducing the distance.

Distance (m) Cyl. lens - Objective	0.850	0.925	1.00	1.075	1.150
Beam propagation XY plane	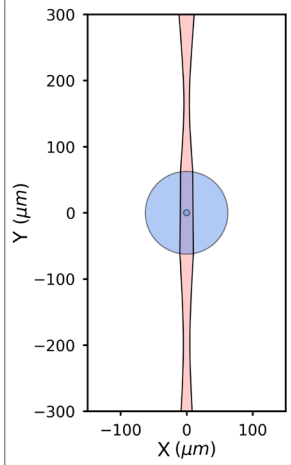	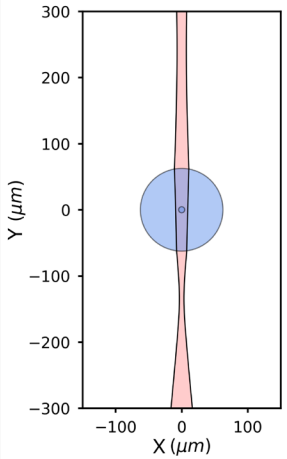	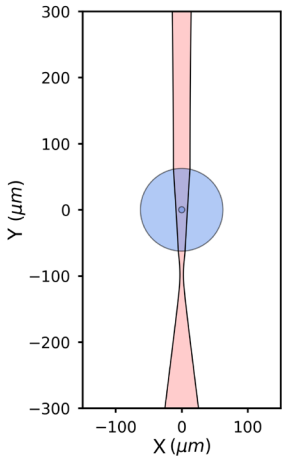	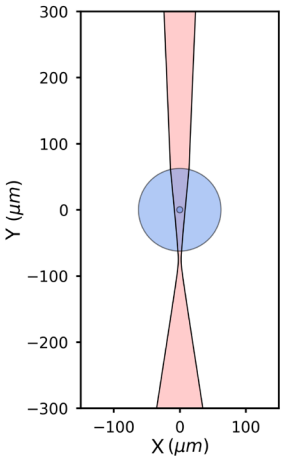	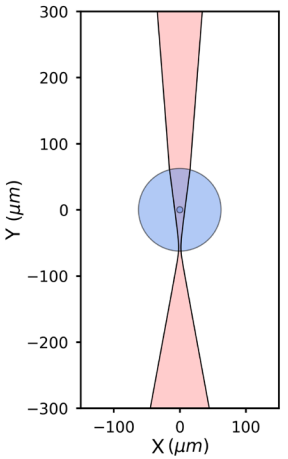
Intensity profile XY plane (A.U.)	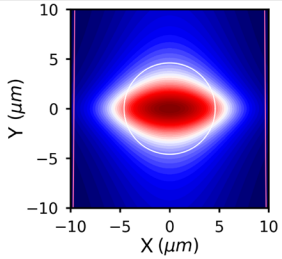	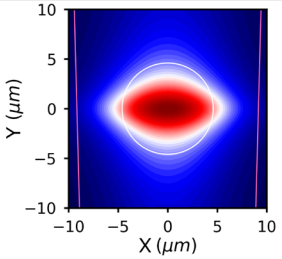	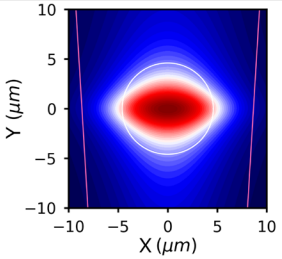	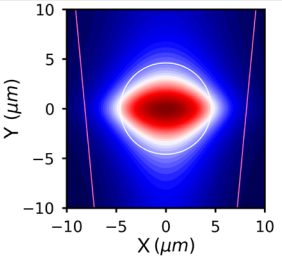	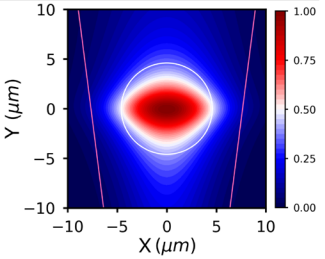

APPENDIX B OFDR ALIGNMENT METHOD

Mathematically, this process of the alignment method can be explained from the overlap integral definition of κ, given in Eq. (2.13):

$$\kappa(z) = \frac{v\omega}{4} \iint_{-\infty}^{\infty} n_{eff}(x,y,z)\, \overline{\Delta n_{eff}}(x,y,z)\, \vec{e}_{kt}(x,y)\, \vec{e}_{jt}^{*}(x,y)\, dx\, dy. \tag{B.1}$$

For single mode operation ($k = j$), we understand from Eq. (B.1) that κ is only maximized when $\overline{\Delta n_{eff}}$ and the mode field overlap perfectly, and any misalignment of the beam position causes a reduction of κ. Exploiting this fact, the alignment process is best described by expressing the coupling coefficient of each probe (κ_i) as a function of the transverse displacement ($\delta x_i, \delta y_i$):

$$\kappa_i(\delta x_i, \delta y_i) = \frac{v\omega n_{eff}}{4} \iint_{-\infty}^{\infty} \overline{\Delta n_{eff}}(x - \delta x_i, y - \delta y_i)\, \vec{e}(x,y)\, \vec{e}^{*}(x,y)\, dx\, dy, \tag{B.2}$$

where i is the alignment probe number. This equation tells us that the signal obtained from measuring κ as a function of the displacement is proportional to the cross-correlation between the RIM's cross-section and the mode field. Therefore, by assuming that the focal spot can be modelled as a Gaussian beam and does not suffer from substantial optical distortions, κ_i should varies approximately as a Gaussian function of the transverse displacement.

The grid that contains the position of transverse displacement ($\delta x_i, \delta y_i$), the number of probes and the length of the characterization section can be adjusted depending on the type of fiber being used and the shape of the focal spot.

To illustrate the accuracy of the method, as well as the sensitivity to misalignment, several weak uniform FBGs of 1 mm ($\kappa L < 3$) were inscribed in an uncoated SMF-28 with a small transverse misalignment relative to the mapping result. Figure B.1 shows their normalized coupling coefficient κ as a function of the deviation from the core center. As expected, the strongest gratings are produced when the objective is well-centered with the mapping result, suggesting low systematic error. It can also be seen that κ drops rapidly when the laser focal spot deviates by just a few μm from the core central position, but the sensitivity to misalignment is reduced over x-axis. This can be explained by two factors. First, because of refraction, it can be shown that

moving the objective by 1 mm toward the fiber (y-axis) induces a displacement of the focal spot by about 1.6 mm inside the glass medium. Secondly, Figure 3.2 (e) showed that the simulated RIM's cross-section is slightly asymmetric and elongated along the x-axis. Even though this minor elongation cannot explain the difference in sensitivity by itself, it should be noted that the geometry of the focal spot is extremely sensitive to variation in beam diameter (see 0), and a wider than expected beam could result in a wider focal spot (along x), hence a lower sensitivity to misalignment.

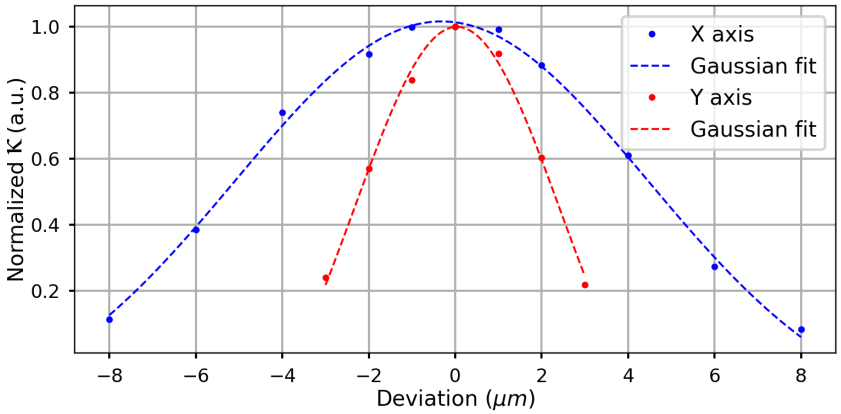

Figure B.1: Normalized coupling coefficient for weak uniform FBGs as a function of the transverse deviation from fiber core center, as measured with the OFDR alignment technique. The inscription was performed in an uncoated SMF-28 fiber, and the deviation was applied along the x and y transverse axis independently.

APPENDIX C PHYSICAL PROPERTIES OF THE FIBERS

Table C.1 Important physical and geometrical properties of the fibers that were frequently used during this thesis. The coating of the SMF-28 fiber [82] was usually removed before inscribing an FBG, while the SM1250(10.4/125)P polyimide coated fiber [83] was mainly used for through-the-coating inscriptions.

	SMF-28	SM1250(10.4/125)P
Manufacturer	Corning	Fibercore
Coating type	Dual acrylate	Polyimide
Coating diameter (µm)	242 ± 0.5	155 ± 5
Cladding diameter (µm)	125 ± 0.7	125 ± 2
Core diameter (µm)	8.2	-
Coating-cladding concentricity (µm)	< 12	-
Core-cladding concentricity (µm)	≤ 0.5	≤ 0.75
Effective refractive index @1550nm	1.4682	-
Mode field diameter @1550nm (µm)	10.4 ± 0.5	10.4 ± 0.8

APPENDIX D FEMTOSECOND LASER DIRECT-WRITING OF HIGH QUALITY FIRST-ORDER BRAGG GRATINGS WITH ARBITRARY COMPLEX APODIZATION BY PHASE MODULATION: SUPPLEMENTAL DOCUMENT

This appendix contains the supplemental document that was submitted to Optics Express along article 1 presented in CHAPTER 4.

Spectral quality of FBGs made above and below the threshold

In Section 4.6.2 of the manuscript, it was mentioned that writing FBGs with pulse energy below the transition (highlighted by the dashed lines on Figure 4.6) leads to a high-quality spectral response, while writing with pulse energy above this threshold causes a deterioration of the spectral response. Figure D.1 illustrates the difference between the two regimes by showing the transmission curves of different FBGs, made with pulse energy either above or below the threshold. The FBGs were inscribed in both an uncoated SMF-28 fiber and a polyimide coated fiber, and they were made with a number of pulses per grating plane that ranges from 1 to 200, as indicated in the legend.

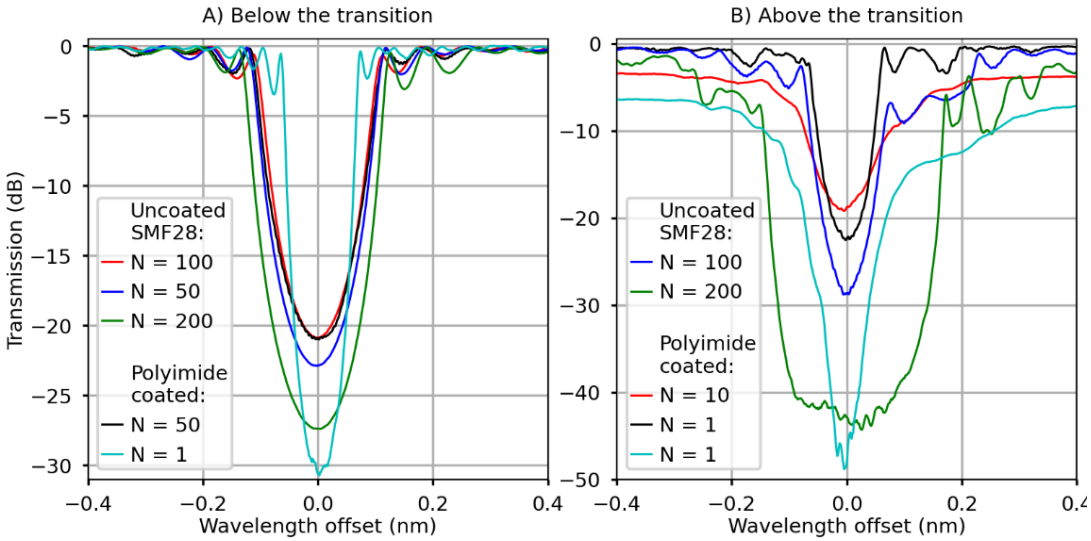

Figure D.1: Illustration of the difference between the spectral response for FBGs written with pulse energy below (A) or above (B) the transition threshold, indicated by the dashed lines of Figure 4.6. The study was performed in both an uncoated SMF-28 fiber and a polyimide coated fiber. N indicates the number of pulses per grating plane that was used for the inscription.